Sapienza Università di Roma

Dottorato di Ricerca in Fisica

Scuola di dottorato ”Vito Volterra”

Detection of underwater acoustic signals induced by ultra-high energy neutrinos interactions.

Thesis submitted to obtain the degree of

”Dottore di Ricerca” - Doctor Philosophiæ

PhD in Physics - XXI cycle - October 2008

By

Francesco Simeone

Program Coordinator

Prof. Enzo Marinari

Thesis Advisor

Prof. Antonio Capone

Contents

List of figures

1. Introduction

In this chapter the motivation of the neutrino astrophysics are discussed and the possible sources of high energy neutrinos are reviewed.

1.1. Motivation for neutrino astrophysics

Almost everything we know about the Universe came from its observation by means of electromagnetic radiation. Using the photons as observation probe it has been possible to discover very energetic sources, however the photons are highly absorbed by matter and so their observation only allows to directly obtain information of the surface process at the source. Moreover energetic photons interact with the photon background (microwave, infrared and radio) and are attenuated during their travel from the source toward us (the GZK effect[1][2]). The main reaction that take place is:

$$\gamma + \gamma_{CMBR} \rightarrow e^- + e^+ \qquad (1.1)$$

assuming a temperature of the cosmic microwave background(CMBR) equal to 2.73K (mean energy ~6.5*10^{-4}eV) the cinematic threshold is equal to $E_\gamma \approx 10^4 m_e^2 / 14 \approx 2 \cdot 10^{14} eV$. This effect reduces the mean free path of a 10^{15}eV photon to about 10kpc and make impossible to study extra galactic sources using photons.
Observation of the proton component of the cosmic rays can give informations about the sources but, since they are charged, low energy protons are deflected by the magnetic galactic fields and loose the directional information that would allow us to point back to their source. High energy protons are slightly deflected by magnetic fields and in principle could be good probe for the high energy Universe. Unfortunately, as pointed out by Greisen-Zatsepin-Kuz'min[1][2], the proton interactions with the CMBR will reduce the proton energy, for instance, by resonant pion production:

$$N + \gamma_{CMBR} \rightarrow N + \pi \qquad (1.2)$$

The kinematic threshold for this reaction is about $5*10^{19}$eV. This prevent the observation of protons with energy above 10^{20}eV coming from sources more distant that about 30Mpc. In figure 1.1 the attenuation length due to different interactions of protons and photons with the photon background is reported.

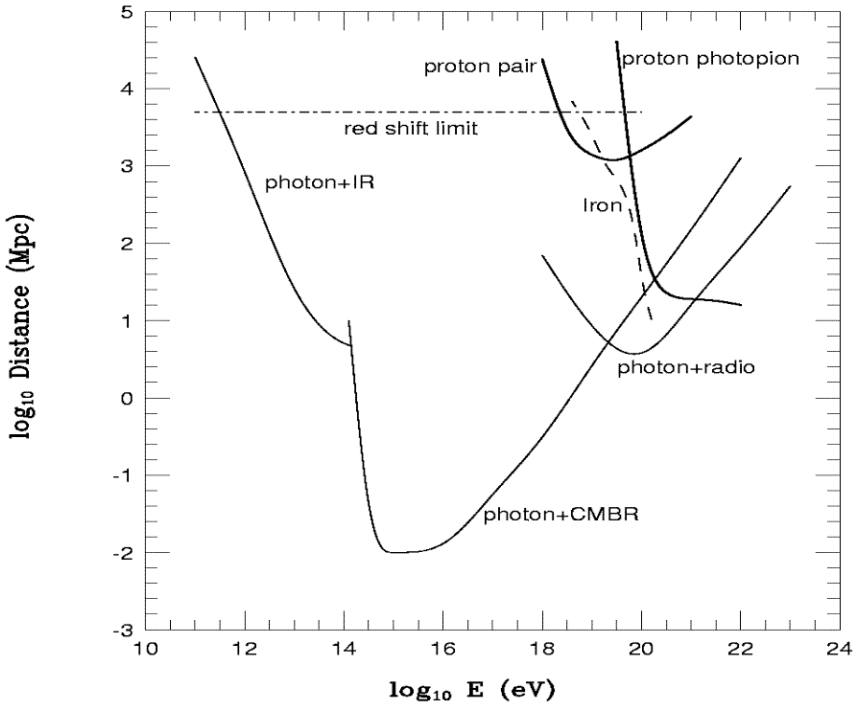

Figure 1.1

The attenuation length of p and γ with the photon background (IR, CMBR and radio) as a function of the incident particle.

In order to directly observe the inner physical mechanism of distant and energetic sources we need to use a neutral, stable and weakly interacting messenger: the neutrino. The interest in studying such high energy sources arises from the fact that much of the classical astronomy is related to the study of the thermal radiation, emitted by stars or dust, while the non thermal energy density in the Universe is roughly equal the thermal one and is assumed to play a relevant role in its evolution. The presence of such non thermal Universe is confirmed by the cosmic ray spectrum reported in figure 1.2.

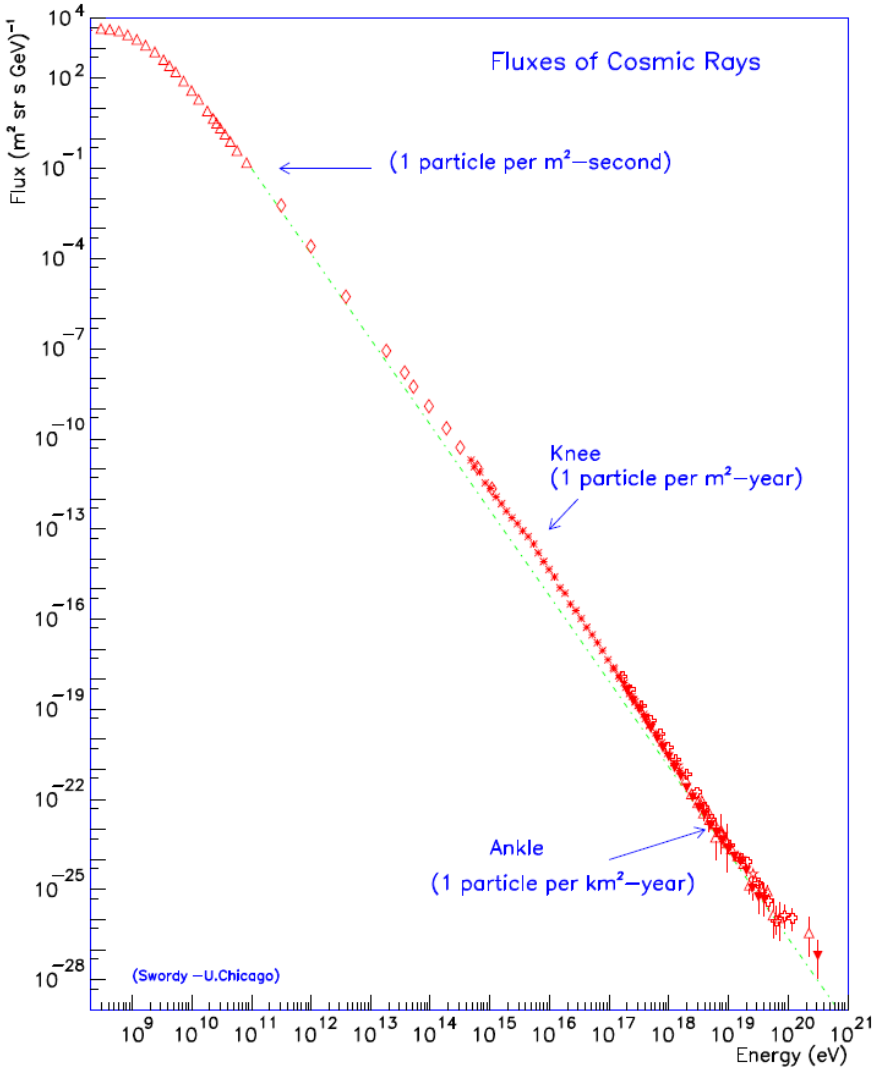

Figure 1.2

The cosmic ray flux as a function of the particle energy[3].

The mechanism by which the cosmic rays are accelerated is still an open question. The supernova shock waves are generally assumed to be the place in which the cosmic rays are produced since the Fermi acceleration mechanism, that takes place in this case, can reproduce quite well their energy spectrum; however the experimental evidence is not complete. In fact few sources of high energy gamma rays are not associated with supernova remnants and this seems to indicate that other mechanisms are present. It is widely accepted that this mechanism can accelerate particles up to 10^{15}eV may be 10^{17}eV, so the highest energy cosmic ray should be accelerated in a different way. Even if the detailed mechanism is still unknown the sources in which the acceleration take

place are the most energetic and interesting place of the Universe and play a key role in its evolution. Such high energy are far beyond the possibility of any Earth based accelerator and thus represents an unique opportunity to test the theory in such energy regions. The neutrino astronomy can open a new window on the high energy non-thermal Universe, increasing our knowledge both in astrophysical and in particle physics fields.

1.2. Sources of ultra high energy neutrinos

All sources where protons are accelerated are sources of high energy neutrinos since the interaction of the accelerated particles with the photons, or matter near the source can produce charged pions that will decay into neutrinos, for instance by the following reaction:

$$p + \gamma \rightarrow n + \pi^+ \rightarrow n + \mu^+ + \nu_\mu \rightarrow n + e^+ + \overline{\nu}_\mu + \nu_\mu + \nu_e \qquad (1.3)$$

As pointed out in the previous paragraph the sources of the highest energy cosmic rays are still unknown however few candidates have been proposed: the Active Galactic Nuclei (AGN) and the gamma ray burst (GRB).

The AGN are galaxies with a super massive (from 10^7 up to 10^9 solar mass) black hole in their centre which is feed by the host galaxies. The AGN model has been developed to coherently explain the experimental properties of different kinds of astrophysical objects: Seyfert galaxies, Blazars and Quasars. All those objects are believed to be AGNs, the different experimental features that they shows are related to the their relative orientation with respect to the observer. In figure 1.3 a schematic view of an active galactic nuclei is reported.

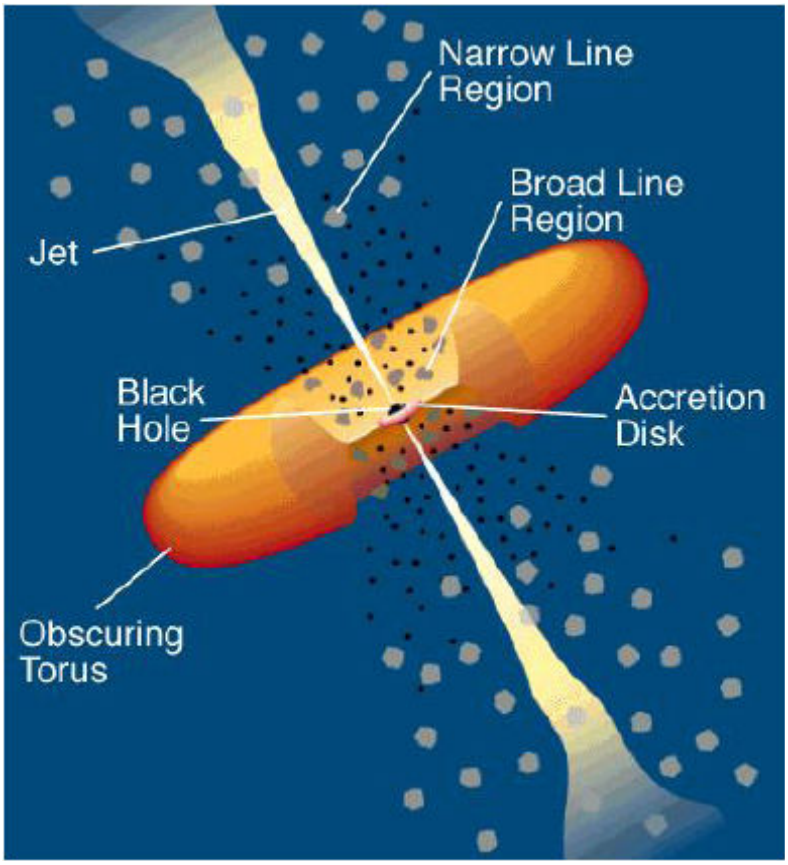

Figure 1.3

Scheme of the central part of the AGN. The unified model of AGN describes different classes of astrophysical objects as an unique object seen by different directions.

The matter contained in the accretion disk feeds the black hole and a fraction of this matter is expelled in jets perpendicular to the accretion disk. The jets are supposed to be the place in which the acceleration takes place by the Fermi mechanism; then by the reaction reported in 1.3 the neutrino are produced.

Another possible source of high energy neutrinos is the phenomenon that is at the origin of the so called gamma ray burst (GRB). The GRB are very short (from millisecond up to few seconds) very intensive burst of gamma rays discovered in ’60 by the Vela satellite. Usually the GRB is followed by an afterglow in the x ray, optical or radio band; spectral analysing of the afterglow reveals that this bursts have an high redshift. Because of their distance the GRB, in the hypothesis of isotropic emission, are the most energetic phenomena of the Universe releasing an energy of the order of 10^{46} J. One of the theoretical models used to explain such events is the fireball model[4] depicted in figure 1.4.

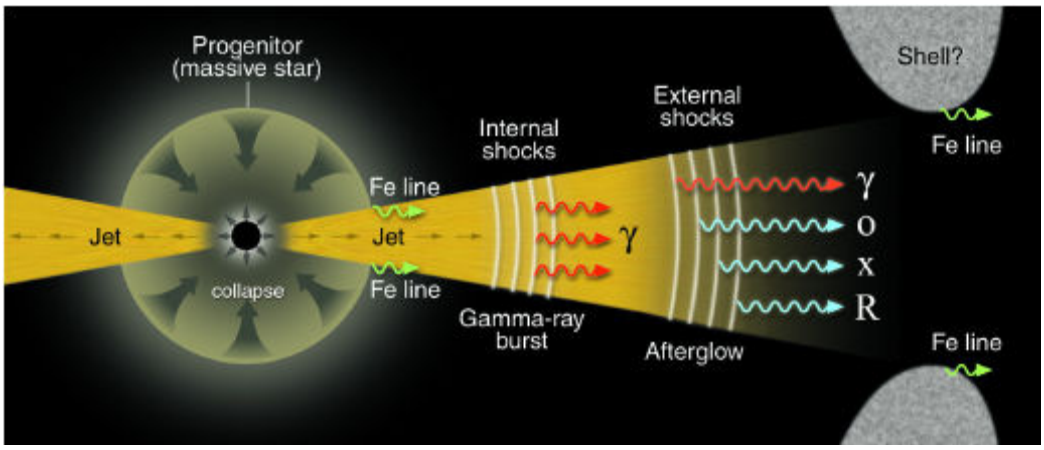

Figure 1.4

The fireball model of the GRB.

In this model a massive star collapse generating a highly relativistic ($\Gamma \approx 100$) shock wave of charged particles and gamma rays that collide with the surrounding medium. This shock wave accelerate, by Fermi mechanism, particles that meets in the medium where it propagates. A modified model (the cannon ball model[5]) assume that the shock waves are collimated in jets instead of having a spherical symmetry, this model allows to explain the observed GRB luminosity with a total energy released by the explosion much lower than the one needed by the fireball model.

A guarantee "source" of high energy neutrino is the GZK effect described in the previous paragraph. The existence of the GZK cut-off is based on solid theoretical predictions and nowadays is also experimentally evident in the Auger and HIRES data. As a consequence the interactions of the primary cosmic rays, during their propagation, will produce high energy neutrinos that will reach the Earth. The GZK neutrinos will retain the directional information that allows to point back to the source since the high energy protons, by which they are generated, are only weakly deflected by the galactic magnetic field.

2. Detection of ultra high energy neutrinos

In this chapter different experimental approaches towards the detection of ultra high energy neutrinos are discussed.

2.1. Water Cherenkov detectors

Water(or Ice)-Ĉerenkov technique is based on the detection of the charged leptons generated in the neutrino charged current weak interactions with the medium surrounding the detector. Those detectors measure the visible Ĉerenkov photons originates by charged particles propagating at velocities greater that the speed of light through a transparent medium and consist of array of photomultipliers.

The charged particle track can be reconstructed measuring the time of arrival of the Ĉerenkov photons on the photomultipliers. Optical Ĉerenkov detectors look for upward going charged leptons since the neutrinos are the only particles that can freely propagate through the Earth and interact with the medium producing upward going particles. A major background for those kind of detectors are the downward going atmospheric muons. Water(or Ice)-Ĉerenkov detectors are usually deeply embedded in natural medium (water or ice) to reduce this muons background using the medium as natural shield. Those kind of apparatuses, with a km^3 scale, can detect neutrinos in an energy interval that range from ~100GeV up to ~10PeV. The lower energy threshold is set by the photomultipliers spacing since the track length, in order to be reconstructed, must be "long" compared with the photomultipliers distance. The upper energy threshold is set by the effective volume of the detector. In the energy range in which those detectors work, the direction of the charged leptons, originated in the neutrino interactions, nearby coincides with the neutrino ones, allowing to reconstruct the neutrino direction. It can be shown that the mean difference in the angular direction between the neutrino and the charged lepton is :

$$\langle \theta_{\mu\upsilon} \rangle \cong \sqrt{\frac{0.7^0}{E_\upsilon [TeV]}} \qquad (2.1)$$

The angular resolution that can be archived is function of the hit time resolution, the scattering length and error in the photomultipliers positions. Water detector can reach angular resolution better than 0.5° (for energy above 1TeV) while, due to shorter scattering length of light in ice, the angular resolution for AMANDA/IceCube detector is worse and typically ~1°/2° respectively.

The Cherenkov technique is well established and presently under use, but is unrealistic to built a detector bigger than few km^3 at a reasonable cost.

There are several experiments currently taking data based on the Ĉerenkov detection technique. The Baikal[6] experiment, started in 1993 is located in the lake Baikal in Siberia and is the oldest. In 1998 has been upgraded reaching 192 photomultipliers and an effective volume of about $10^{-4}km^3$. AMANDA[7] and its successor IceCube are located in the South Pole. IceCube is the biggest neutrino telescope currently working. AMANDA is composed of 677 PMTs embedded in the Antarctic ice and reaches an effective volume of $10^{-2}km^3$. The ANTARES[8] experiment is composed by 12 string of photomultipliers, each string consisting of 75 PMTs and the whole apparatus has an effective volume of about $10^{-2}km^3$. The ANTARES telescope is the biggest neutrino telescope operating in the northern hemisphere. There are detectors actually being constructed in the Mediterranean sea: the NEMO[9] collaboration will deploy a detector prototype 100km off the Sicily coast during next year and the NESTOR[10] collaboration is working to built, using a different technical approach, a prototype detector in the Ionian sea. Moreover there is a European collaboration Km3Net[11] planning to built a kilometer cubic scale detector in the northern hemisphere complementary to the IceCube detector.

2.2. Radio Cherenkov detectors

This experimental technique is based on the detection on the coherent radio emission generated by the shower induced by the neutrino interaction. It was first proposed by

Askaryan in 1962[12] and verified experimentally in 2001[13] in an accelerator beam tests. As an electromagnetic shower develops, especially in dense medium, a charge asymmetry is generated since the positrons annihilate with the electrons of the medium. The resulting net current, during the shower development, originates a coherent electromagnetic pulse for wavelength longer than the shower extension. Askarian also suggested different natural mediums in which the radio Ĉerenkov signal should have attenuation length of the order of few kilometers: the sand, the ice and the salt. All the paste and present experiments use one of those natural medium. The first generation of those kind of experiments were: FORTE[14] a satellite antenna launched in 1997 that was able to monitor the ice over Greenland until 1999, RICE[15] an array of 16 broadband antennas (200MHz-1000MHz) deployed together with AMANDA in the Antarctic ice cap that is taking data since 1999 and GLUE[16] an experiment that uses two radio telescopes of 34m and 70m to look for the radio emission of the neutrino interaction on the Lunar regolith as depicted in fig. 2.1.

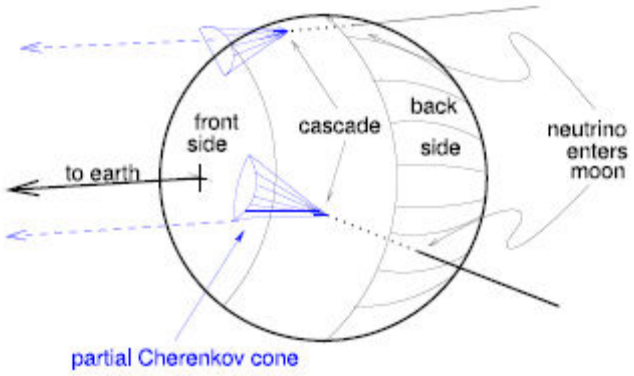

Figure 2.1

The Cherenkov cone originated by the UHE cascade in the Lunar regolith.

A new generation experiment is ANITA[17] a balloon experiment that is designed to detect neutrino interactions in the Antarctic ice. The ANITA satellite, shown in fig.2.2, is composed of 32 broadband antennas able to measure radio pulses from 200MHz to 1200MHz. The first flight of ANITA was done in 2006 and the balloon made three trips around the South Pole for a total life time of 35 days. ANITA has monitored the

Antarctic ice by an altitude of 37km, monitoring an ice surface of about $10^6 km^2$. Further launches are planned for the period 2008-2009.

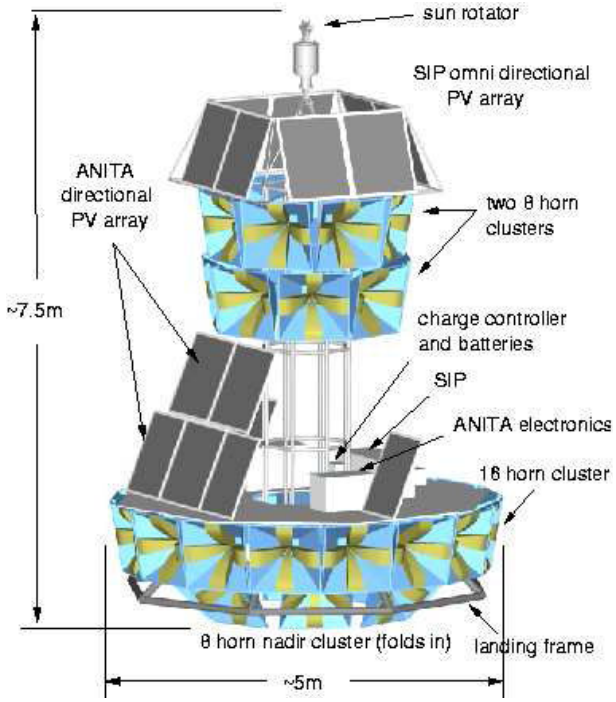

Figure 2.2

The scheme of the ANITA satellite.

2.3. Extensive Air shower detectors

Extensive air shower detectors (EAS) are designed to identify the shower induced by a cosmic ray interaction in the atmosphere. The biggest experiment of this kind currently taking data is the Pierre Auger Observatory[18]. It's an hybrid detector that measures the cascades, induced by the cosmic ray interaction in the atmosphere, using two different techniques, the detection principle is shown in fig. 2.3.

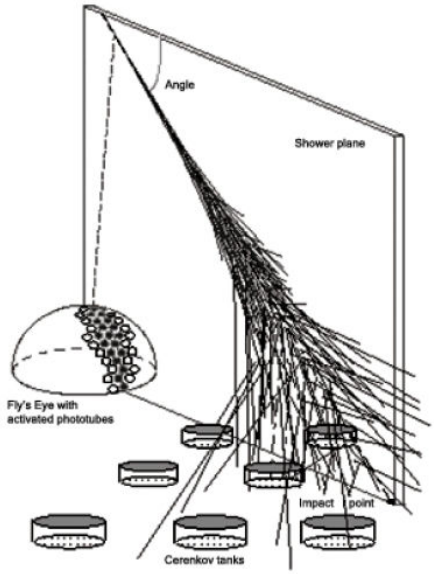

Figure 2.3

Detection principle of the Pierre Auger Observatory: the fly's eyes measure the fluorescence light emitted by the nitrogen atoms during the shower propagation in the atmosphere while the surface detectors measure the Cherenkov light of the charged particles that reach the ground.

The surface detectors are filled with pure water and are equipped with three photomultipliers that detect the Cherenkov light, produced in water, by the charged particles of the cascade. Those detectors are 1600 and are spaced by 1.5km. Moreover there are four fluorescence detectors that measure the fluorescence light emitted by the nitrogen during the propagation of the cascade's particle in the atmosphere. The Pierre Auger Observatory detector has an effective area of about 3000km^2 and is designed to detect the cosmic ray in the region of the GZK cutoff. Due to its dimension it is also capable of detecting the very rare neutrino interactions in the atmosphere. The primary cosmic rays interact on the top of the atmosphere while the neutrino interaction can happen at any depth. Measuring the cascade maximum directly with the fluorescence detectors or indirectly using the electron-muon ratio at the ground level it is possible to discriminate a neutrino induced cascade by a proton one. The detection of inclined showers seems to be a valid technique to distinguish neutrino and proton induced interaction: for these events the primary must have interacted deep in the atmosphere.

2.4. Acoustic detectors

The acoustic detection technique of neutrino induced cascades, in water or ice, is based on the thermo-acoustic effect, described in more details in chapter 3. The cascade energy is deposited in a narrow region of the medium, induces a local heating and results in a rapid expansion of the water (or ice). The expansion originates a pressure wave that propagates perpendicularly to the cascade direction. The acoustic detectors are composed of many acoustic sensors distributed in a wide instrumented volume; by measuring the acoustic induced neutrino pulse with several sensors it will be possible to infer the neutrino direction. The interest in this technique is related to the high attenuation length(~km) of the sound in water(or ice). Consequently it is possible to instruments a huge volume using a relatively low number of sensors. We will demonstrate that this technique is effective only at very high neutrino energy(~10^{19}eV) where a huge detection volume is anyway necessary to reveal the extremely faint neutrino flux foreseen by the models. This detection technique is relatively new and no "acoustic" experiment, designed specifically to reveal neutrinos, is at present in operation. A pioneer experiment, SAUND[19], is taking data using existing arrays of military hydrophones.

The SAUND experiment uses seven hydrophones of an array of 52 located at the Bahamas, the geometrical position of the hydrophones is reported in fig. 2.4.

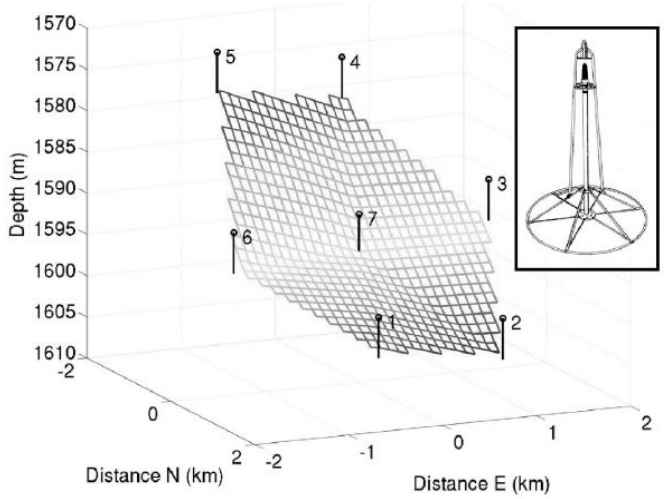

Figure 2.4

Schematic view of the SAUND hydrophones and their relative positions. The insert shows the mechanical structure that supports the hydrophones.

Despite of the low number of hydrophones and of the fact that their position and their electronic readout has not been optimized for the neutrino detection the SAUND collaboration was able to set the first upper limit for the diffuse neutrino flux, in the energy range $E_\upsilon \geq 10^{22} eV$ using an acoustic detection technique. Their result is reported in figure 2.5.

2.5. Present limits on the neutrino flux

Up to now no one of the experiments described has claimed to have observed astrophysical neutrinos. In figure 2.5 we report the upper limits for the diffuse neutrino flux provided by several experiments compared to the flux predicted by some theoretical models. In the vertical axis the flux is multiplied by E^2, as usual, since the energy spectrum expected by a Fermi acceleration mechanism is proportional to E^{-2} .

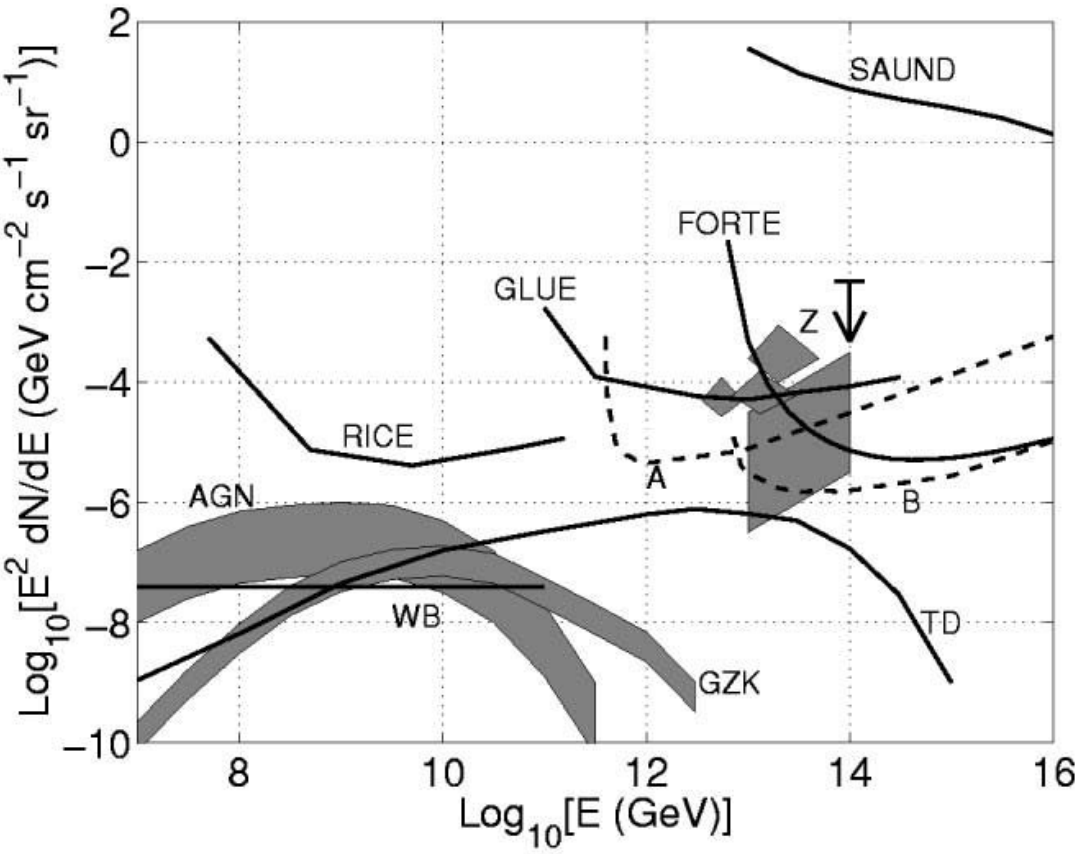

Figure 2.5

Summary of the upper limit to a diffuse neutrino flux set by different experiment (solid line labeled SAUND, GLUE, RICE). In the figure the neutrino flux predicted by different theoretical model are reported: Z for different models of Z burst, AGN for active galactic nuclei, TD for neutrino generated by topological defects and WGB for the Waxmann-Bahcall limit. The dashed lines labeled as A and B are the sensitivity of two different acoustic array discussed in [19].

3. Neutrino interactions in water

This chapter summarizes the main features of the neutrino interaction in water and the acoustic signal generation. The thermo-acoustic model, for the acoustic signal formation as a consequence of the neutrino interaction in water, and its link with the environmental parameters are described; then experimental verifications of this model are discussed. Showers development at very high energy (above 100 TeV) is reviewed and finally results from simulation, reported from literature, are summarized.

3.1. Thermo-acoustic model

We define here thermo-acoustic signal the pressure wave generated by the quasi-instantaneous heating of a macroscopic water volume in which a high-energy shower has developed. This effect was first suggested by G. A. Askarian in 1957 [20] and then confirmed experimentally, as discussed further in subsection 3.2, with proton and laser beam experiments. The shower, originated by UHE particle interacting in water, develops almost at the speed of light releasing a macroscopic energy in the medium. The energy deposited in the medium can be dissipated by different mechanisms: heat conduction, viscous friction and the thermo-acoustic one. Considering that the thermal conductivity coefficient in water is $\alpha \approx 10^{-7}\, m^2/s$ and the viscous friction one is $\beta \approx 10^{-6}\, m^2/s$ is possible to evaluate the characteristic time of those processes, over a length of 1m, as $\tau_\alpha \approx l^2/\alpha \approx 10^7 s$ and $\tau_\beta \approx l^2/\beta \approx 10^6 s$. Those times are much bigger than the characteristic time for a pressure wave propagation in water $\tau_\gamma \approx l/c_s \approx 10^{-3} s$ so it is safe to assume that the dissipation of the shower energy will occur by pressure wave propagation. Moreover the deviation from the thermodynamic equilibrium, of the part of medium interested by the high-energy cascade, could be considered as instantaneous since the heated water volume will expand much slowly than the speed of light.

The water expansion results in the emission of an impulse of pressure described by the following wave equation:

$$\frac{1}{c_s^2}\frac{\partial^2 p(\vec{r},t)}{\partial t^2} - \nabla^2 p(\vec{r},t) = \frac{\beta}{C_p}\frac{\partial^2 q(\vec{r},t)}{\partial t^2} \tag{3.1}$$

In this equation p is a small deviation from the hydrostatic pressure (in the position $\vec{r}$ and at the time t) and c_s is the speed of sound in the medium. The source term in this equation is the so called thermo-acoustic term in which q is the energy density, β is the expansion coefficient and C_p is the specific heat capacity at constant pressure. In this equation the parameters depend on the water properties such as temperature, salinity and hydrostatic pressure. It's convenient to group the environmental parameters in an adimensional one, the Gruneissen parameter γ

$$\gamma = \frac{\beta c^2}{C_p} \tag{3.2}$$

This parameter expresses the conversion efficiency of the thermal energy into sound. In fig. 3.1 it's shown the dependence of the Gruneissen parameter value for different sites and depths.

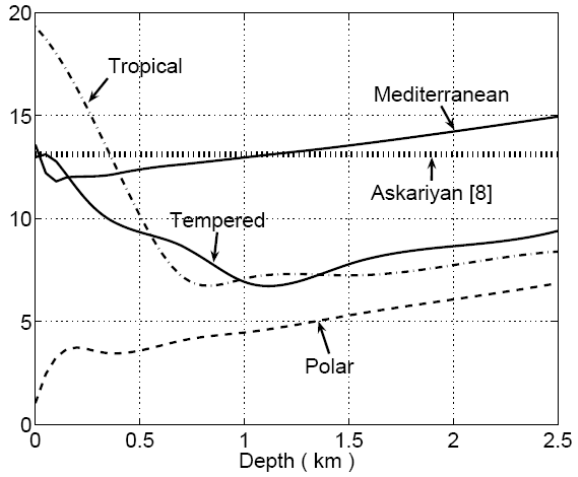

Figure 3.1

The Gruneissen parameter value expressed in % for different waters as function of the depth. The difference in its value are mainly due to differents water temperatures[2].

The equation 3.1 could be solved using the Kirchhoff integral:

$$p(\vec{r},t) = \frac{\beta}{4\pi C_p}\int \frac{dV'}{|\vec{r}-\vec{r}'|}\frac{\partial^2}{\partial t^2} q\left(\vec{r}', t - \frac{\vec{r}-\vec{r}'}{c}\right) \tag{3.3}$$

that can be simplified, since the energy deposition is almost instantaneous, assuming

$$\begin{aligned} q(\vec{r},t) &= q(\vec{r})\theta(t) \\ \dot{q}(\vec{r},t) &= q(\vec{r})\delta(t) \end{aligned} \tag{3.4}$$

where $\theta(t)$ is the step function and $\delta(t)$ is the delta function; this leads to the following equation:

$$p(\vec{r},t) = \frac{\gamma}{4\pi}\frac{\partial}{\partial R}\int_S \frac{q(\vec{r}')}{R} d\sigma \tag{3.5}$$

where the integration is performed over spherical shells of radius $R = c_s t$ centred on $\vec{r}$; the meaning of this integral is that the pressure in $\vec{r}$ at time *t* is the sum of all contributions that can reach this point propagating at the speed of sound.

This approach neglects the attenuation of the pressure waves, during the propagation from the source to the point $\vec{r}$ and assumes a linear propagation in the medium, which is not the case as will be discussed in detail during next chapter. Although those limitations, this technique is very effective at short distance form the source (roughly ~100m). The detailed simulation of the acoustic signal has been studied by many groups[21,22,23,24] and in subsection 3.4 I will summarize the results obtained describing the parameterization of the acoustic signal that will be used during the rest of this work.

3.2. Experimental proof of the thermo-acoustic model

The thermo-acoustic model allows to describe how the energy deposited in a medium, by an high-energy cascade, generates a pressure wave. It's possible to test this model in laboratory using other ways to deposit energy in the medium. Two different kind of approaches have been carried out in past years: experiments using high intensity an low energy particles beams[25] (*beam-dump*) and experiments using a laser beam[26].
In *beam-dump* experiments the energy deposition in water is obtained using a proton beam; the typical set up is depicted in fig 3.2.

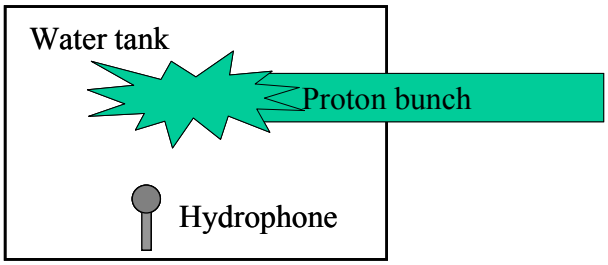

Figure 3.2

The proton beam enter in a water tank containing the hydrophone. The energy deposited in the medium generates an acoustic pulse recorded by the hydrophone

The protons energy is transferred to the medium by ionization and proton nucleus scattering. The energy of each proton bunch is mostly released at the end of its path, the so called Bragg's peak, since the energy loss per unit of length increases as the energy decreases. In figure 3.3 we show an example of energy deposition along the track.

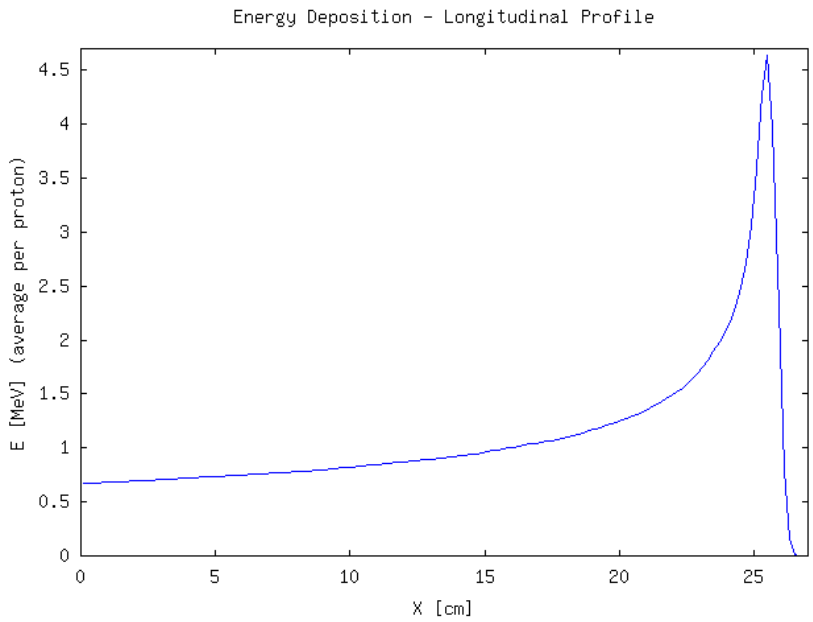

Figure 3.3

Longitudinal profile of the energy distribution. The energy of each single proton is 200MeV, the number of proton simulated is 10^5. [27]

This generates an energy deposition that is roughly point like. To correctly simulate the energy density deposited by the beam in the medium, is necessary to accurately measure both the beam intensity and its spatial distribution. This technique requires some care in handling the function that do represent the energy deposition since it can't be considered neither point like nor instantaneous.

Laser beam experiments are conceptually identical to the *beam-dump* ones but use a different technique to release energy in the medium; as the laser propagates in water its intensity decreases exponentially releasing energy to the medium by exciting the rotational and vibrational modes of the water molecules. All the experiments reported in literature have validated the thermo-acoustic model in principle but the results have large systematic and statistical errors so it is not possible to conclude that the model has been tested with high precision.

3.3. High energy showers in water

A detailed study of the neutrino interaction with nucleon and its simulation are beyond the scope of this work, however there are many works in literature that can be used, here the relevant results for this study are reported.

In figure 3.4 the total cross section for neutrino nucleon interaction is shown as function of neutrino energy[28].

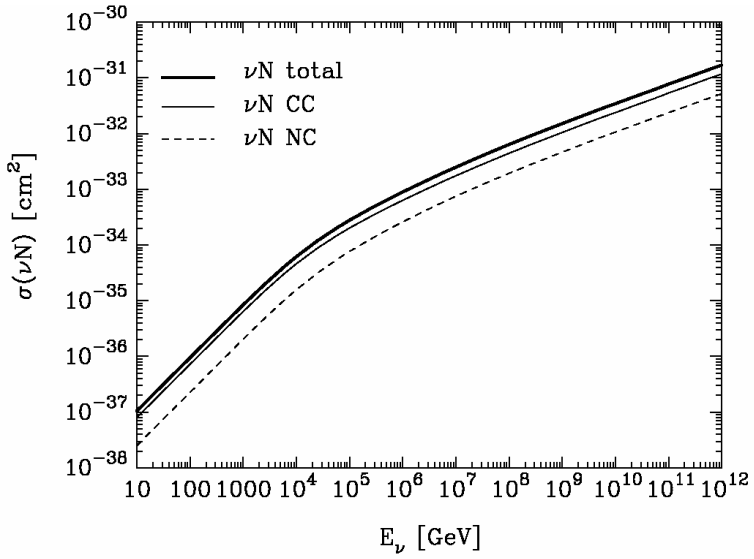

Figure 3.4

Neutrino nucleon cross section as function of the neutrino energy.

As the cross section increases the corresponding interaction length decreases; this implies that the Earth will became opaque to ultra high energy neutrinos. Defining the interaction length as:

$$L_{\text{int}} = \frac{1}{\sigma_{tot}(E_\nu)\rho N_A} \tag{3.6}$$

where $\rho \cong 5.5\, g/cm^3$ is the mean density of the Earth and $N_A = 6.022 * 10^{23}\, mol^{-1}$ is the Avogadro's number and using the neutrino cross section given by the parameterization:

$$\sigma_{tot} = 1.2 * 10^{-32} \left(\frac{E_\nu}{10^9\, GeV} \right)^{0.4} cm^2 \tag{3.7}$$

which is valid for neutrino energy above $10^{14}\, eV$, it is possible to show, as reported in figure 3.5, that the interaction length became smaller than the Earth radius for energy above $\approx 3 * 10^{14}\, eV$.

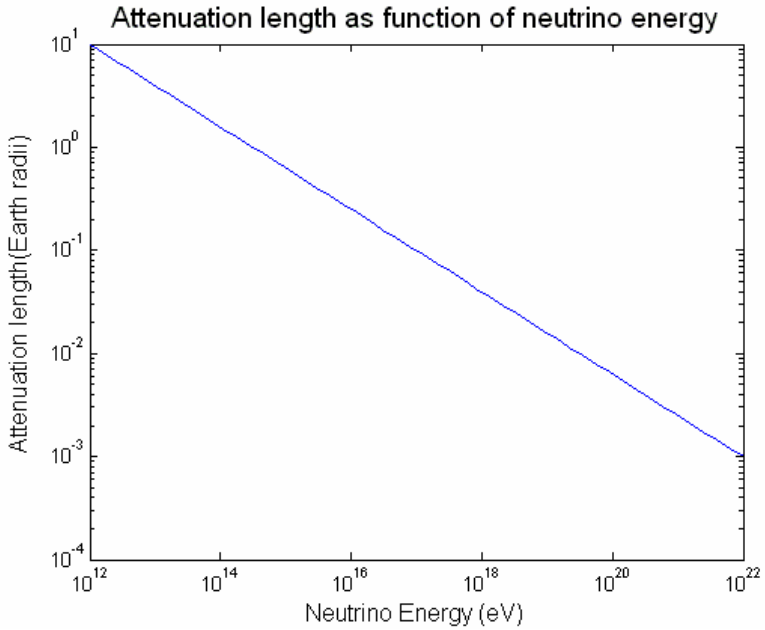

Figure 3.5

Attenuation legnth as function of the neutrino energy expressed in earth radii

As it will be shown in the remaining part of this chapter the acoustic signals, produced by neutrino interactions in water, are faint for energies below $10^{18}\, eV$; this fact implies that only UHE neutrinos can generate acoustic signals in water and, unlike the case of optical Cherenkov detection discussed in chapter 2, these neutrinos can reach the apparatus only from above. The angular distribution of UHE neutrinos capable to generate acoustic signals can be evaluated using the parameterization of the neutrino-

nucleon interaction cross section and simple geometrical considerations. Let's assume that the depth of the sea is h and that the Earth curvature could be neglected; in this approximation the path traveled by the neutrinos in water, as function of zenith angle, is:

$$\Delta = h\sqrt{1+\tan(\theta)^2} \tag{3.8}$$

The probability that the neutrino travels undisturbed through the medium and interacts in a sphere of radius R around the detector is:

$$P = \left(1 - e^{\frac{-R}{L(E)}}\right) e^{\frac{-(\Delta(\theta)-R)}{L(E)}} \tag{3.9}$$

where L is the interaction length as a function of neutrino energy. If we assume that the angular distribution of the incident neutrino flux is isotropic, it's convenient to weigh this probability for the solid angle. The results, in case of R=2km and h=3km is represented in figure 3.6 as function of zenith angle and neutrino energy. This distribution indicates that the most abundant events, for the energy range considered here, are the horizontal ones.

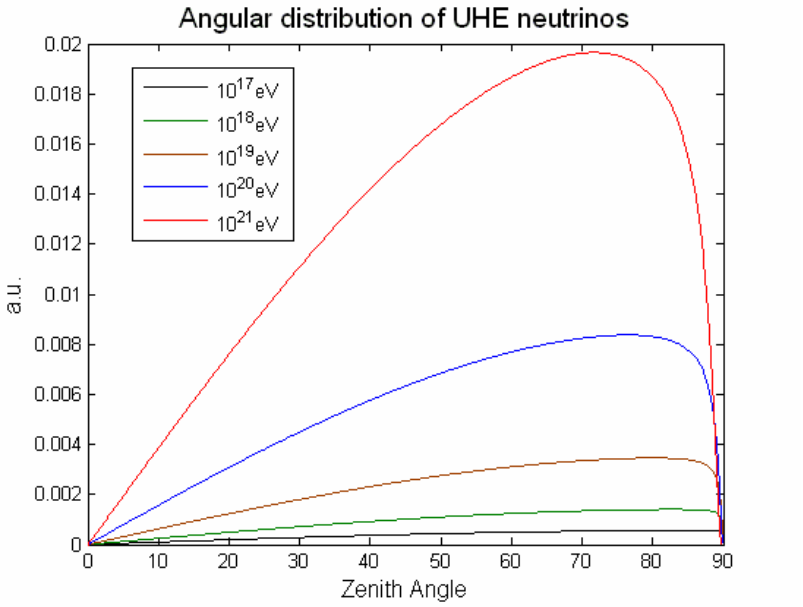

Figure 3.6

Angular distribution of the acoust detectable UHE neutrino interaction as funtion of the incident angle and neutrino energy.

The neutrino interaction with the nucleons of the medium could be of two types:

charge current interaction (CC)

$$\overset{(-)}{\nu}_{\ell} + N \rightarrow \ell^{\pm} + X$$

where the subscript ℓ indicates the lepton flavour (e, μ, τ). In this type of interactions the neutrino converts into the corresponding lepton and the kinetic energy transferred to the nucleon generates a hadronic shower.

neutral current interaction (NC)

$$\overset{(-)}{\nu}_{\ell} + N \rightarrow \overset{(-)}{\nu}_{\ell} + X$$

In this kind of interactions the outgoing neutrino can't be detected so the only visible part of the final state is the hadronic shower.

In general the differential cross section for neutrino interacting with nucleons can be parameterized by[28]:

$$\frac{d^2\sigma}{dxdy} = \frac{2G_F^2 m E_\nu}{\pi}\left(\frac{M_{W(Z)}^2}{Q^2 + M_{W(Z)}^2}\right)^2 \left[xq\left(x,Q^2\right) + x\bar{q}\left(x,Q^2\right)\left(1-y^2\right)\right] \tag{3.10}$$

where $G_F = 10^{-5} GeV^{-2}$ is the Fermi constant, q and $\bar{q}$ are the quarks, and antiquarks, distribution functions, m is the target mass, $M_{W(Z)}$ is the mass of the gauge boson exchanged ($W^{\pm}$ for the CC interactions and Z^0 for the NC ones) and Q^2 is the four-momentum exchanged. The adimensional variables $x = Q^2/2M\varepsilon$ and $y = \varepsilon/E_\nu$, called Bjorken invariants, are used to describe the energy and momentum exchanged by the neutrinos with the quark inside the nucleus. In figure 4 the total, the CC and NC cross sections are plotted as functions of the neutrino energy. In a wide range of energy the ratio of the CC cross section over the total one is :

$$\frac{\sigma_{CC}}{\sigma_{CC} + \sigma_{NC}} \approx 0.7 \tag{3.11}$$

this means that in about 70% of the neutrino interactions with nucleons there is the production of a charged lepton.

It's especially important which part of the neutrino energy is transferred to the hadronic cascade in NC and CC interactions. The kinematical variable which is relevant in this case is the Bjorken variable y

$$y = \frac{E_{vin} - E_{vout}}{E_{vin}} \tag{3.12}$$

where E_{vin} is the energy of the incident neutrino and E_{vout} is the energy of the outgoing neutrino(NC) or lepton(CC) in the laboratory frame. As reported from Gandhi the mean

inelasticity $\langle y \rangle$, shown in figure 3.7, is weakly dependent on energy and its value is about 20%.

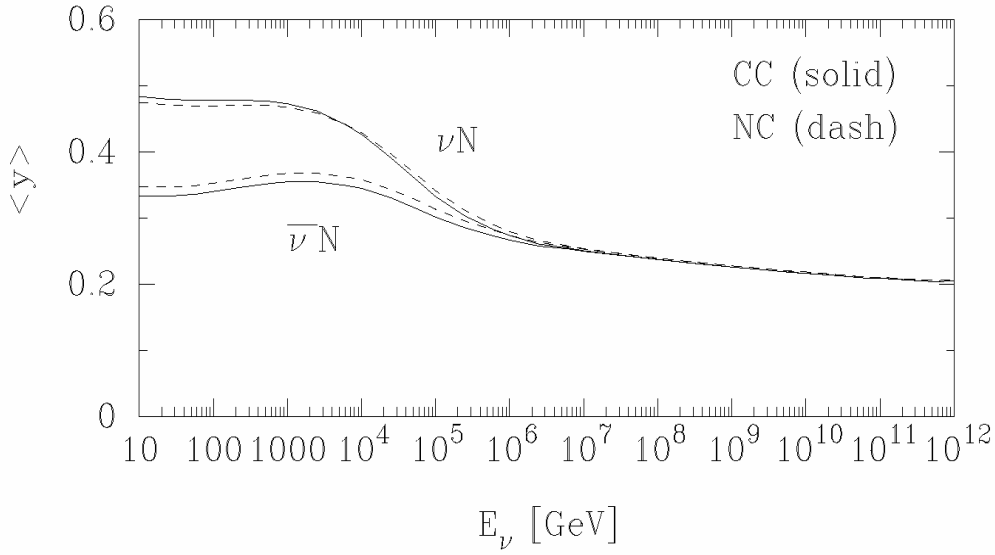

Figure 3.7

Mean inelasticity as function of the neutrino energy. Above $10^6 GeV$ there is no significant difference between neutrino and antineutrino inelasticity. Moreover its value weakly dependent on energy and is about 20-25%.[9]

From these considerations it might seem that the golden events are the electromagnetic showers produced during the CC interactions, which are the most abundant and retains about 80% of the incident neutrino energy. Unfortunately this is not the case at very high energy. It was first noticed[29,30] by Landau, Pomeranchuk and Migdal (LPM) that above a threshold of about $10^{17} eV$, the cross sections for bremsstrahlung and pair production decrease as $\sqrt{E}$. Usually those cross sections are calculated assuming moment transfer to a single scattering centre. As the energy increases the inter-atomic distance, seen in the frame of reference of the ultra relativistic particle, decreases; when this distance is comparable with the wave packet length of the particle, destructive quantum interference between amplitude from multiple scattering centres arises and the interaction length starts to increase. As a consequence the shower becomes longer and sub showers will develop along the main shower as the particle energy drops below the LMP threshold; the longitudinal profile of one cascade above the LPM threshold is shown in figure 3.8.

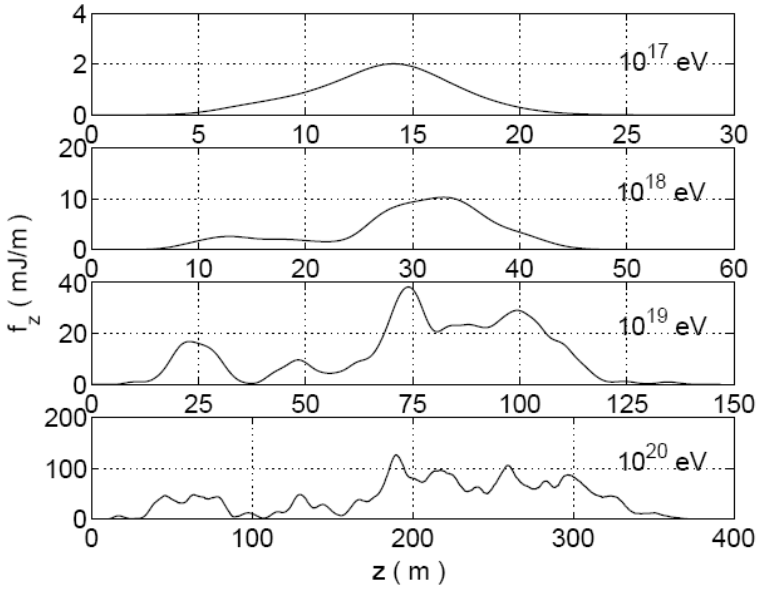

Figure 3.8

Energy density profile of an electromagnetic shower at differnt energy. As the LPM effect start to play a significant role the shower length increases; this prevent the energy density to increases linearly with the neutrino energy.[2]

The amplitude of the acoustic signal, as pointed out in the first paragraph, depends on the energy density deposited in the medium, therefore this effect greatly reduces the amplitude of the acoustic signal. Detailed simulations have been performed by many authors[21,22,23,24] and all of them agree that the acoustic signal amplitude of the electromagnetic showers, despite the energy difference, are comparable to the hadronic ones. Furthermore their statistical fluctuations are big and their simulation difficult so in this work I reduce the study to the acoustic signal produced by the hadronic showers.

3.4. Present results of acoustic signal simulation

The hadronic shower induced by neutrino interaction in water deposits most of its energy in a cylindrical volume of some tens centimetres radius and few tens of meter length (figure 3.9).

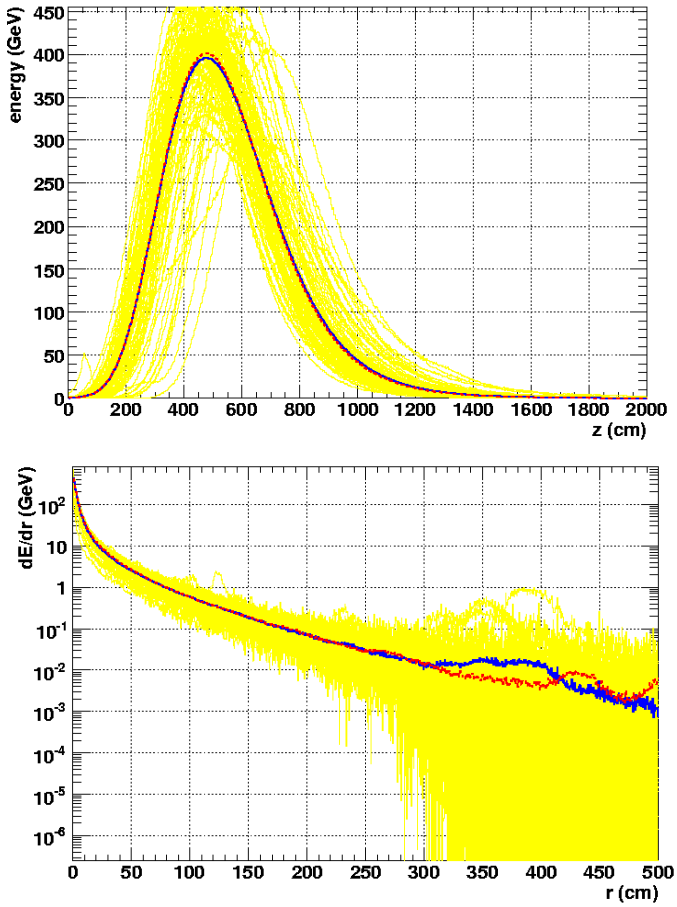

Figure 3.9

Radial(up) and longitudinal(down) energy deposition for 100TeV proton. The red curve indicates the mean of one hundred of simulated interactions.[5]

The detailed profile depends on energy and statistical fluctuation but, as pointed out in the previous paragraph, the amplitude of the acoustic signal vary linearly with the density of the energy deposition. As consequence I assume that the amplitude of the acoustic signal vary linearly with neutrino energy. In figure 3.10 the shape of an acoustic signal, at 1km from the shower and its power spectral density (PSD) are shown. The signal shape is due to Lehtinen[23] and is calculated assuming a constant attenuation as function of frequency; so its PSD is not changed during the propagation and can be considered equal to the PSD of the signal at the source.

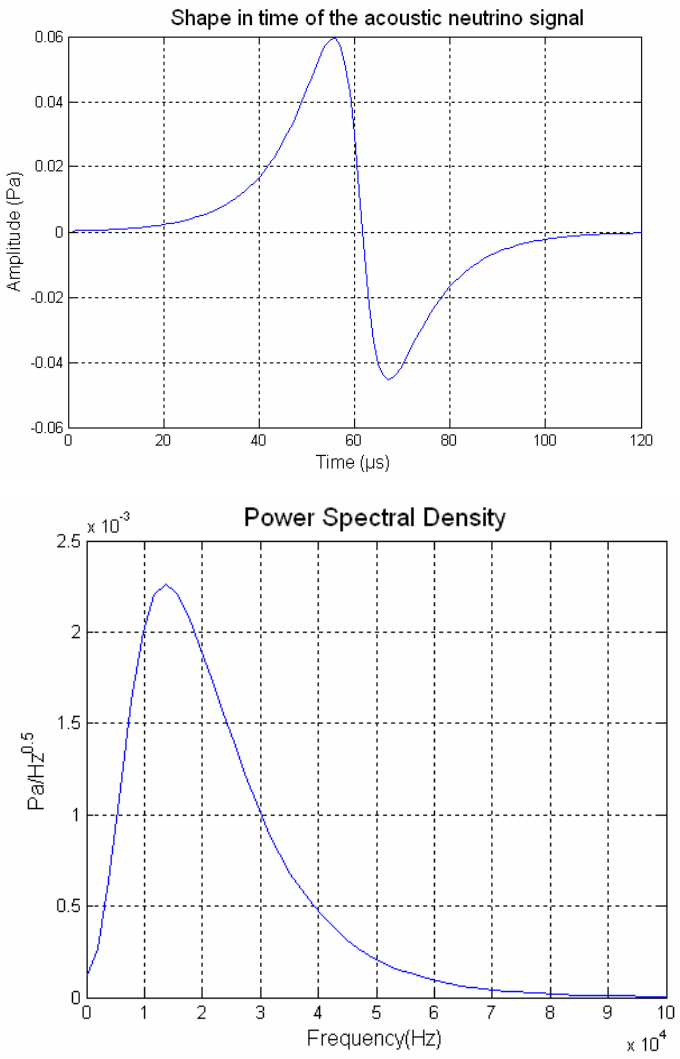

Figure 3.10

Shape in time of the acoustic signal induced by neutrino interaction in water(up) and its power spectral density(down)

One of the most important features of the acoustic signal produced by a shower is its angular distribution. As pointed out in the previous paragraph the energy deposition could be considered as instantaneous and so the sound generation (pressure wave from water expansion) along the shower. The simultaneous sound production along the shower results in a coherent emission in the plane perpendicular to the shower axis. The process of coherent sound emission can be treated in analogy to the diffraction from a slit of finite size. Assuming a cylindrical distribution of energy density the shape in time and the amplitude of the acoustic signal is function of the azimuth emission angle as illustrated in figure 3.11.

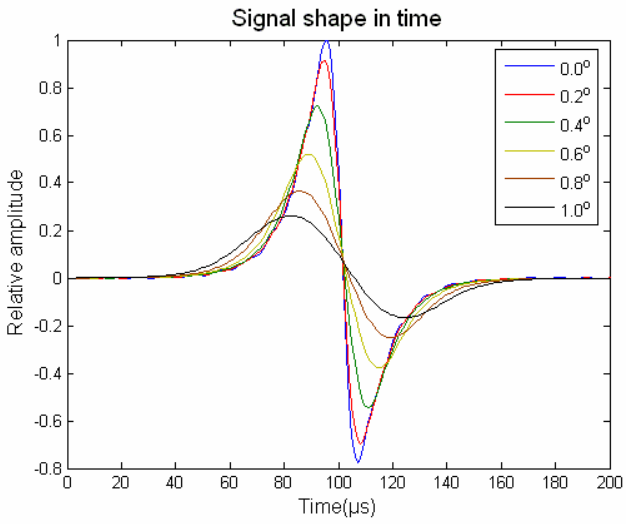

Figure 3.11

Shape in time of the acoustic signal as a function of the azimuthal angle of emission.

The sound emitted by two parts of the cylinder, at distance d, will interfere destructively if the path difference $d\sin(\theta)$ is equal to $\lambda/2$. The intensity profile as function of the azimuth angle can be evaluated using the Fraunhofer diffraction integral and turn out to be:

$$I(\theta) = I_0 \left(\frac{\sin\left(\frac{\pi d}{\lambda}\sin(\theta)\right)}{\frac{\pi d}{\lambda}\sin(\theta)} \right)^2 \tag{3.13}$$

this equation is valid for $d^2/\lambda L << 1$ that is usually mentioned as the "far field" approximation.

As expected, the intensity profile is function of the sound wave length. To evaluate the angular distribution of our signal we need to decompose it into plane wave and apply eq. 3.13 to all frequency components. The result of this operation is reported in figure 3.12.

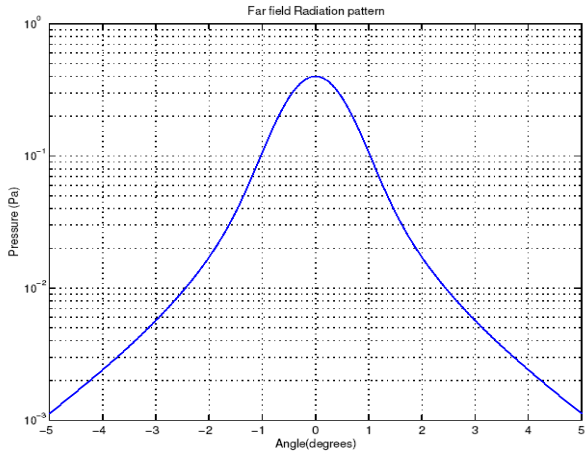

Figure 3.12

Far field radiation pattern as a function of the azimuthal emission angle. Tha intensity of the sound pulse decreases of about 20dB in 3 degrees.

It's important to stress that, since the relative intensity of each frequency component will vary as function of θ, the shape of the signal itself is a function of the emission angle. In particular as we move from the plane perpendicular to the shower the high frequency content of the signal is attenuated and so its height decreases and its width increases as reported in figure 3.11.

The result of this chapter is a signal parameterization that will be used in the rest of this work. The signal shape in time is reported in figure 3.10, I assumed that its amplitude is a linear function of the neutrino energy and that its spectral content will vary only as a function of the emission angle θ.

4. Underwater environment

The neutrino signal, after its generation, propagates through the underwater environment. Due to the characteristics of the medium, during the propagation, the signal amplitude is attenuated, its power spectral density is changed and the wave-front is distorted. This chapter describes the underwater environmental properties and discusses in detail the underwater sound propagation. Moreover different approaches, to deal with the propagation, are presented.

4.1. Sound velocity in water

The speed of sound, in water, depends on several environmental parameters, in particular the pressure, the temperature and the salinity. The sound speed value is ~1500m/s and varies weakly with the environmental conditions; for reference it increases, with the depth about 1.7m/s every 100m, while a temperature change of 1˚C will result in a difference of about 4m/s. Even if the relative velocity variation due to the environment changes, over a practical range, is of the order of few percents, the accurate knowledge of the sound speed is needed to correlate in time signals from distant sensors. Let's suppose to have two different sensors h_1 and h_2, whose distances from the source are s_1 and s_2. The time of arrival for the sensor 1 is obviously $t_1 = \frac{s_1}{c}$, the difference in time of arrival may differ from the nominal value $t_{12} = t_2 - t_1$ depending on the local variation of the sound speed as $\Delta t_{12} \cong -\frac{(s_2 - s_1)}{c^2}\Delta c$. If we want to evaluate t_{12} for sensors whose distance is about 100m with an error small, compared with the expected signal length (~100μs as discussed in 3.4), we need to know the sound velocity with the precision of about 1m/s. Many empirical equations have been derived to calculate the sound speed over a wide range of environmental parameters with different precision[31,32,33].

A very common and useful equation is:

$$c = 1449 + 4.6T - 0.055T^2 + 0.0003T^3 + (1.39 - 0.012T)(S - 35) + 0.017Z \qquad (4.1)$$

that is a simplified version of the one proposed by Wilson in 1960[33]. In the expression T is the temperature(˚C), S the salinity(ppt) and Z the depth(m).
This empirical equation has an accuracy, mediated over a wide range of environmental parameters, of about 2m/s. Moreover the uncertainty on the environmental parameters must be taken into account:

$$\Delta c = (5.02 - 0.11T + 9*10^{-4}T^2 - 0.012S)\Delta T - 0.012T\Delta S + 0.017\Delta Z \qquad (4.2)$$

Common precision of commercial instruments are $\Delta T \approx 0.05\,^{\circ}\mathrm{C}$ $\Delta S \approx 0.05\,ppt$ and $\Delta Z \approx 1m$; those values leads to a statistical error, for practical range of parameters, below 0.5m/s. Other equations are more accurate for instance the one proposed by Del Grosso[31] or the Chen and Millero[32] formula. In particular the empirical equation published by Del Grosso and used in this work has a mean error of about 8cm/s and a maximum error of 66cm/s.
The sea is mainly a stratified medium in which the relevant seasonal, or shorter time-scale variation, occur only in the upper layers. This can be understood thinking about the energy transfer in the medium. The main input power comes from the solar energy that is absorbed, depending on the wavelength, in less than few hundred of meters. The heat input into the ocean from the surface, increases stability (through a reduction of density at the surface) and prevents efficient heat penetration into the deep layers. As we can see from figure 4.1, at depth below few hundred meters the variations of temperature and salinity are small and do not show seasonal variations.

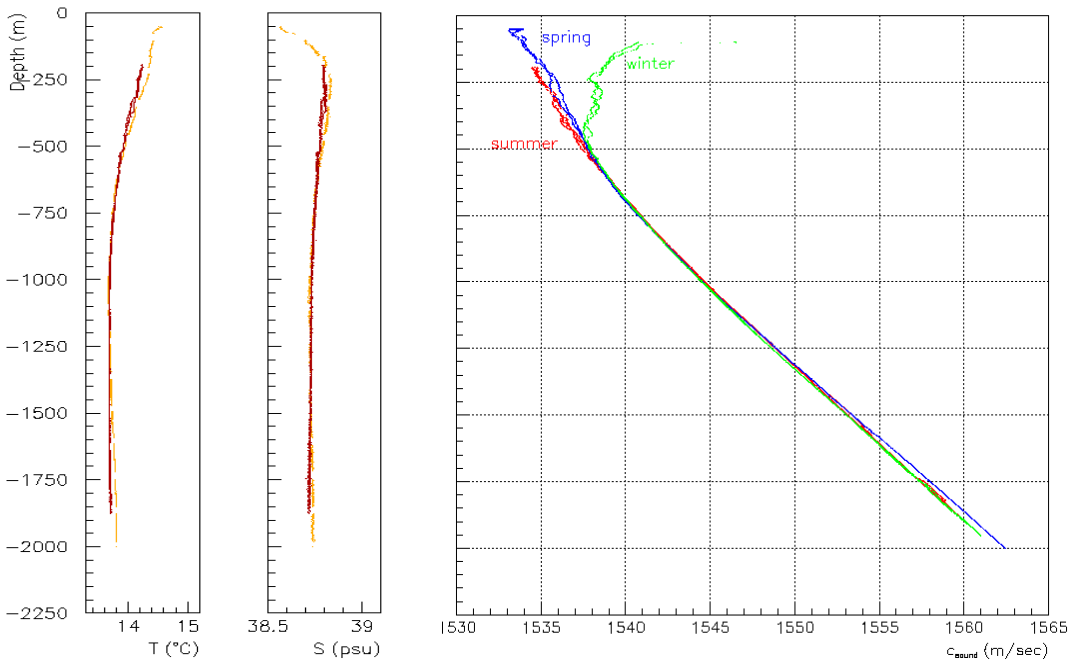

Figure 4.1

The temperature and the salinity are measured with a CTD, while the sound speed is computed using an empirical expression due to Millero. In the deepest layers there is no seasonal variation of the environmental parameters. [34]

In the deepest layers of the sea the main variation of the sound speed are due to the pressure changes with depth.

4.2. Sound attenuation

The sound is attenuated, during the propagation, due to geometrical spread of the wave-front and due to the characteristic of the medium. The geometrical attenuation simply derive from the energy conservation: if we assume that the pressure wave is spherically expanding in the medium, the intensity of this wave decreases a r^{-2}, for geometrical reasons, therefore the signal amplitude decreases as r^{-1}. This kind of attenuation does not depend on frequency.

Regarding the attenuation due the medium there are two main processes: the viscosity of the fluid and the reaction of dissolved ions in seawater. During the propagation those processes convert a fraction of the wave energy into heat dissipated in the medium. The

propagation in space of the acoustic signal is well represented by an exponential law. The variation of signal intensity can be specified by a ratio, usually expressed by its attenuation $\left(\frac{I(\vec{x})}{I_0}\right)$ in dB. So the effect of the absorption process are usually given in dB/m. An absorption of 1dB/km means that the energy is reduced by 21% after each kilometre traveled. The attenuation coefficient, as discussed by Francois and Garrison[35] can be written as:

$$\alpha = 10^{-3}\left[\frac{A_1 P_1 f_1 f^2}{f_1^2 + f^2} + \frac{A_2 P_2 f_2 f^2}{f_2^2 + f^2} + A_3 P_3 f^2\right] dBm^{-1} \tag{4.3}$$

where the A_i represents the temperature and salinity dependencies, the P_i are the pressure dependencies, the f_i are the relaxation frequencies, and subscript refer to the boric acid (1), magnesium sulphate (2), and pure water (viscosity)(3). The viscosity absorption proposed by Francois and Garrison has ten constants and two different fits for temperature above and below 20 ˚C, for simplicity here I report a simplified expression derived from Ainslie and McColm[36]:

$$\alpha = 4.9 * 10^{-4} f^2 e^{-\left(\frac{T}{27} + \frac{D}{17}\right)} dBkm^{-1} \tag{4.4}$$

where T is the temperature (˚C) and D is the depth (m). This is a very small effect but dominates at high frequency(>100kHz). Note that this is the only effect present in fresh water and that increasing the temperature or the depth leads to a decrease of the absorption length due to the negative exponential term. The other two terms in the equation 4.3 describe the absorption due to ionic relaxation. In the unperturbed sea there is an equilibrium between the molecular and the ionic system of the various salt dissolved. For example the magnesium sulphate is in equilibrium between:

$$MgSO_4 \leftrightarrow Mg^{2+} + SO_4^{2-} \tag{4.5}$$

and as the wave, propagating through the medium, modify the pressure this equilibrium state change. This variation convert a fraction of the wave energy into chemical energy and later on into heat. Different reactions have different relaxation time or relaxation frequency. Pressure change faster than the relaxation time of a reaction have a little effect on it since they can be considered as adiabatic.

The simplified expression for the relaxation frequency of the magnesium sulphate and the boric acid by Ainslie and McColm[36] are:

$$f_1 = 0.78\left(\frac{S}{35}\right)^{0.5} e^{\frac{T}{26}} kHz \text{ (for the boron)} \tag{4.6}$$

$$f_2 = 42e^{\frac{T}{17}} kHz \text{ (for the magnesium)} \tag{4.7}$$

In figure 4.2 the attenuation coefficient for a temperature of 14˚C a salinity of 35‰ and a pH equal to 8.2 are shown.

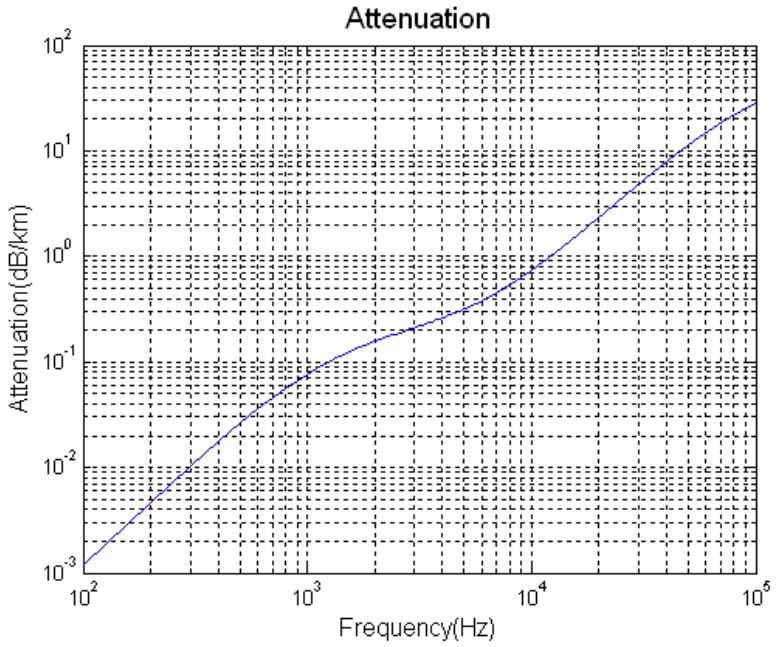

Figure 4.2

Attenuation as a function of the frequency of the pressure wave.

The boron contribution dominates for frequency below 5kHz while the viscosity is the only relevant effect for frequency above 100kHz; the magnesium dominate the absorption in the frequency range of interest for the neutrino signal detection. We can then conclude that the attenuation due to chemical relaxation and viscosity is frequency dependent so the signal spectral density will be modified during the propagation as shown in fig 4.3.

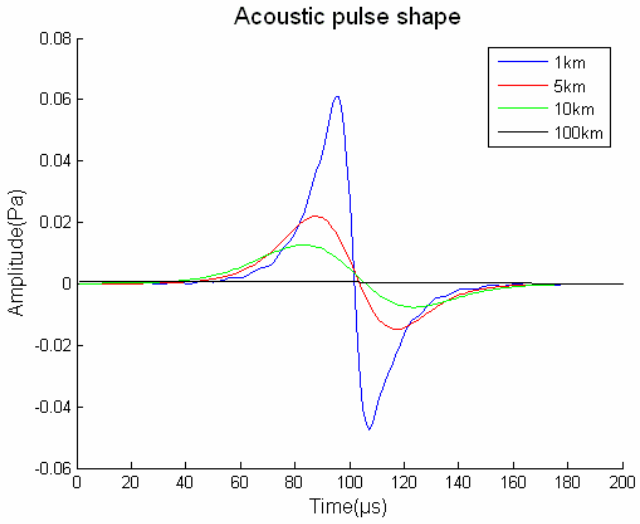

Figure 4.3

Variation of pulse shape with respect to distance, the only contribution assumed here is the one due to the medium properties.

4.3. Sound propagation

The propagation of the sound is governed by the wave equation:

$$\nabla^2\psi(\vec{x},t)=\frac{1}{c^2(\vec{x},t)}\frac{\partial^2}{\partial t^2}\psi(\vec{x},t) \qquad (4.7)$$

where $\psi(\vec{x},t)$ is the pressure and $c(\vec{x},t)$ is the speed of sound in position $\vec{x}$ at time t. We can safely neglect the time dependence of the sound speed since, as discussed in

4.1, during the propagation time the environmental parameters can be considered as constant. From now on we consider $c(\vec{x},t)=c(\vec{x})$.

We can look for a solution of the form $\psi(\vec{x},t)=\varphi(\vec{x})e^{i\omega t}$ to obtain the Helmotz equation:

$$\left[\nabla^2+k^2(\vec{x})\right]\varphi(\vec{x})=0 \tag{4.8}$$

where $k(\vec{x})=\frac{\omega}{c(\vec{x})}$. The Helmotz equation could be greatly simplify if it's reasonable to look for a solution, in high frequency limit, of the form:

$$\varphi(\vec{x})=A(\vec{x})e^{i\omega\theta(\vec{x})} \tag{4.9}$$

in which $A(\vec{x})$ is a slowly varying function compared to the phase function $\theta(\vec{x})$. This approximation, that leads to the eikonal equation, is particularly well verified in our specific case: when the wavelength is much smaller that all the other relevant lengths in play we can safely neglect the wave properties and deal with a particle-like propagation. As discussed in the previous paragraphs, the only significant change in the sound speed, relevant for this study, is due to the pressure variation with depth. The speed of sound gradient $\left(\frac{\Delta c}{\Delta z}\right)$ is about $0.017s^{-1}$ or $58.8Hz$ while, as shown at the end of chapter 3, the most of the signal energy lies above ~5kHz.

Substituting eq. 4.9 into eq. 4.8 we obtain:

$$\nabla^2 Ae^{i\omega\theta}+2\nabla Ai\omega\nabla\theta e^{i\omega\theta}+A\left(i\omega\nabla^2\theta e^{i\omega\theta}+\left(i\omega\nabla\theta\right)^2 e^{i\omega\theta}\right)+k^2=0 \tag{4.10}$$

where for clearness I drop the spatial dependency of $A(\vec{x}),\theta(\vec{x})$ and $k(\vec{x})$. In the high frequency limit the expression 4.10 simplified into the form:

$$\left(\nabla\theta(\vec{x})\right)^2=\left(\frac{1}{c(\vec{x})}\right)^2 \tag{4.11}$$

that is the eikonal equation.

From this equation, one can derive a Hamiltonian system of equations for the position and generalized momentum for all the possible trajectory that can describe the wave propagation. This has been done by many authors, in our case is convenient the form due to C.A.Boyles[37]:

$$\begin{aligned} \frac{d}{ds}\left(n\frac{dx}{ds}\right) &= \frac{\partial n}{\partial x} \\ \frac{d}{ds}\left(n\frac{dy}{ds}\right) &= \frac{\partial n}{\partial y} \\ \frac{d}{ds}\left(n\frac{dz}{ds}\right) &= \frac{\partial n}{\partial z} \end{aligned} \tag{4.12}$$

In the expression above s is the curvilinear coordinate along the ray path and n is the "sound refraction index" defined as

$$n = c_n / c \,. \tag{4.13}$$

c_n is the sound velocity in the point where the tangent of the trajectory is horizontal (θ=0). Recalling from 4.1 that, in our case, the only variation to the sound speed is due to the depth, we can simplify this expression assuming that $n = n(z)$.

$$\begin{aligned} n\frac{dx}{ds} &= const \\ n\frac{dy}{ds} &= const \\ \frac{d}{ds}\left(n\frac{dz}{ds}\right) &= \frac{dn}{dz} \end{aligned} \tag{4.14}$$

The first two equations state that the ray path lies on a plane and this plane is perpendicular to the xy plane. We can assume here, without loss of generality, that this plane in the xz plane. In this case we have:

$$\frac{dx}{ds} = \cos(\theta)$$
$$\frac{dz}{ds} = \sin(\theta) \tag{4.15}$$

Substituting eq 4.15 into eq 4.14 we obtain:

$$n\cos(\theta) = const$$
$$\frac{d}{ds}(n\sin(\theta)) = \frac{dn}{dz} \tag{4.16}$$

From here it is possible to derive a number of results. First we note that eq. 4.15 is the Snell law since it can be rewritten as:

$$\frac{\cos(\theta)}{c} = const \tag{4.17}$$

and this constant value is fixed along the sonic ray. Using the Snell law it is possible to demonstrate that in a medium in which the sound speed varies linearly with the depth the sonic ray path is an arc of circle. I will use the geometry depicted in fig 4.4.

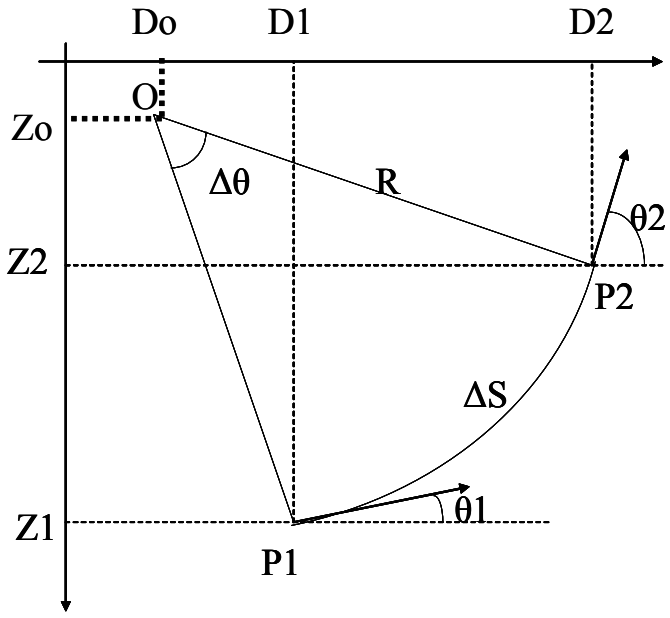

Figure 4.4

The sonic ray path passing throught two generic points P1 and P2. The Z axis point to the bootom of the sea.

Let's us consider a sonic ray and two points P1 and P2 on its path; using the Snell law we can write:

$$\frac{\cos(\theta_1)}{c_1} = \frac{\cos(\theta_2)}{c_2} \tag{4.18}$$

Moreover we know that the speed of sound is a linear function of the depth so:

$$\begin{aligned} c &= c_0 + G(z - z_0) \\ c_1 - c_2 &= G(z_1 - z_2) = G\Delta z \end{aligned} \tag{4.19}$$

where G is the constant gradient of the speed of sound. Substituting this equation into eq 4.18 we can derive the following expression:

$$\frac{c_1}{G\cos(\theta_1)}\left(\cos(\theta_1) - \cos(\theta_2)\right) = \Delta z \tag{4.20}$$

This can be done for every couple of points then is valid for the whole trajectory. It is then possible to see that the path is circular and that the radius is, in any point j of the path, equal to:

$$R = \frac{c_j}{G\cos(\theta_j)} \tag{4.21}$$

The curvature radius depends on the emission angle to respect to the horizontal and its minimum value is about ~100km. Since the ray path is an arc of circle, using simple geometrical considerations we can derive the equation for the spatial displacements along the ray as a function of the initial and final angles, referring to figure 4.4 for the symbols definition:

$$\begin{aligned} \Delta x &= x_2 - x_1 = \frac{c1}{G\cos(\theta_1)}(\sin(\theta_1) - \sin(\theta_2)) \\ \Delta z &= z_2 - z_1 = \frac{c1}{G\cos(\theta_1)}(\cos(\theta_2) - \cos(\theta_1)) \\ \Delta s &= R\Delta\theta \end{aligned} \tag{4.22}$$

It's possible to evaluate the travel time along an arc of trajectory using eq 4.16:

$$
\begin{aligned}
&\frac{d}{ds}\left(n\sin(\theta)\right)=\frac{dn}{dz}\\
&\frac{dn}{ds}\sin(\theta)+n\cos(\theta)\frac{d\theta}{ds}=\frac{dn}{dz}\\
&\frac{dn}{dz}\frac{dz}{ds}\sin(\theta)+n\cos(\theta)\frac{d\theta}{ds}=\frac{dn}{dz}\\
&\frac{dn}{dz}\sin(\theta)^2+n\cos(\theta)\frac{d\theta}{ds}=\frac{dn}{dz}\\
&n\cos(\theta)\frac{d\theta}{ds}=\cos(\theta)^2\frac{dn}{dz}\\
&\frac{d\theta}{ds}=\frac{\cos(\theta)}{n}\frac{dn}{dz}\\
&\frac{d\theta}{ds}=\frac{-\cos(\theta)}{c}G\\
&\frac{d\theta}{dt}=-\cos(\theta)G
\end{aligned}
\qquad (4.23)
$$

where G is the constant gradient of the speed of sound; we have assumed that $\cos(\theta)\neq 0$. The last equation can be integrated leading to an expression of the sound propagation time:

$$
\begin{aligned}
&\Delta t=\int_{\theta_1}^{\theta_2}\frac{-1}{G\cos(\theta)}d\theta\\
&\Delta t=\frac{-1}{G}\ln\left(\frac{\tan\left(\frac{\pi}{4}+\frac{\theta_2}{2}\right)}{\tan\left(\frac{\pi}{4}+\frac{\theta_1}{2}\right)}\right)
\end{aligned}
\qquad (4.24)
$$

Those equations will be apply in the next paragraph to develop a suitable ray tracing algorithm.

4.4. Ray tracing technique

Ray tracing is a technique to calculate the propagation of waves through a medium in which the speed of sound, as well as other characteristics, changes. Under this circumstances, the wave-front can change direction or be distorted. Ray tracing approximate the wave-front with a finite number of beams and propagate them through the medium by discrete steps.

In this work I'll use the ray tracing technique to propagate the sound wave from the source (the shower) to the pressure sensors and to trace back the wave-front, measured by different sensors, to the source.

The algorithm used starts with the eq 4.15 and 4.23 developed in the previous chapter:

$$\begin{aligned} \frac{d\theta}{dt} &= -\cos(\theta)G \\ \frac{dx}{ds} &= \cos(\theta) \\ \frac{dz}{ds} &= \sin(\theta) \end{aligned} \tag{4.25}$$

where s is the curvilinear length along the ray path and G represents the variation of the sound speed as a function of depth ($\partial c/\partial z$) here assumed constant in the whole space. Those equations could be rewritten as finite difference equations:

$$\begin{aligned} \theta_{n+1} &= \theta_n - \cos(\theta_n)G\Delta t \\ x_{n+1} &= x_n + \cos(\theta_{n+1})c(z_n)\Delta t \\ z_{n+1} &= z_n + \sin(\theta_{n+1})c(z_n)\Delta t \end{aligned} \tag{4.26}$$

and holds only if the temporal step, of index n and size Δt, is sufficiently small to consider the propagation as linear during the step. This approach could be extended to the case in which the vertical profile of the sound speed is an arbitrary function of depth. In fact is always possible to choose a temporal step for which the approximation of constant gradient holds; for a shorter temporal step the approximation of linear

propagation will hold. This allows to modify the first equation of 4.26 in the case of arbitrary vertical profile:

$$\theta_{n+1} = \theta_n - \cos(\theta_n) G(z_n) \Delta t \tag{4.27}$$

where $G(z_n) = \partial c(x, y, z)/\partial z$ is function of the depth z_n. I investigate the accuracy of this method by considering the case where the speed of sound gradient is a constant $G = 0.017 s^{-1}$ and the launching angle is $\theta_0 = 0$. In this case the exact solution, as shown in the previous paragraph, is an arc of radius $R = c(z_0)/G$ which is the minimum bending radius possible. In figure 4.5 the exact result is compared with the ray tracing results as function of temporal step.

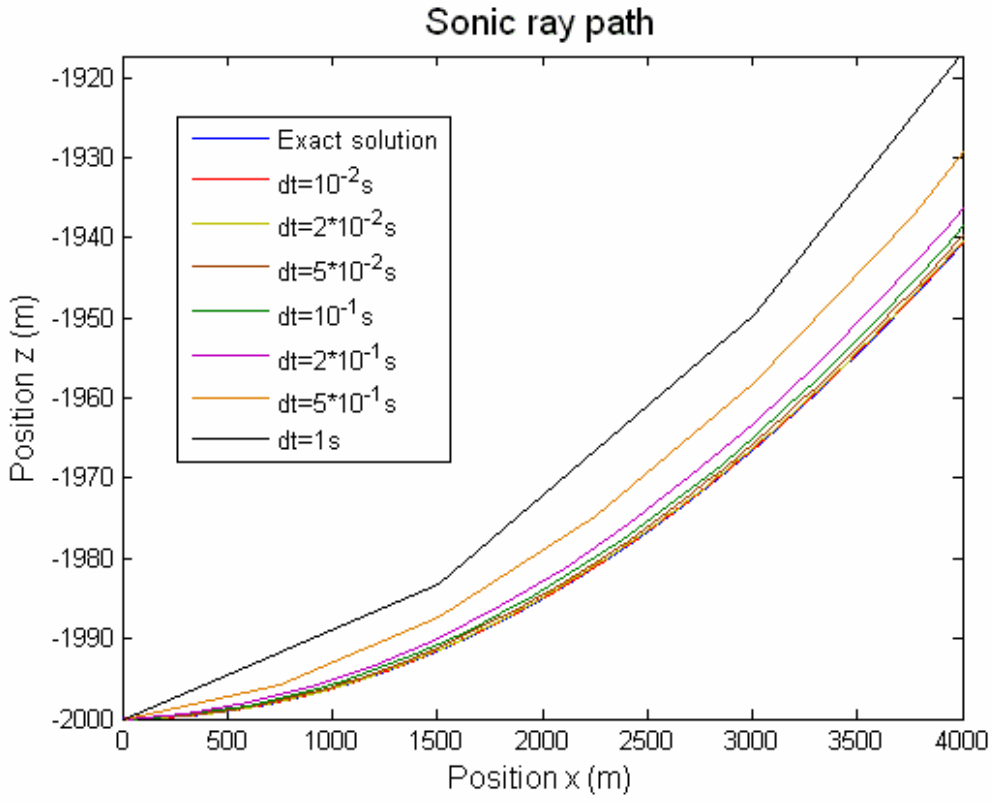

Figure 4.5

The simulated ray path for different simulation steps compared with the exact solution.

To illustrate the validity of the technique in case of arbitrary speed of sound profile I simulated the propagation choosing the Munk's sound speed profile given[38] by the formula :

$$c(z) = c_N\left(1 + 0.00737\left(P - 1 + e^{-P}\right)\right) \tag{4.28}$$

where $P = \dfrac{(z - 1300)}{650}$ and $c_N = 1500\, m/s$.

Using an initial depth of 1000m and emission angle ranging from -15˚ to +15˚ in steps of 0.5˚. I obtained the results report in figure 4.6 that are in agreement with the one presented in [38,39].

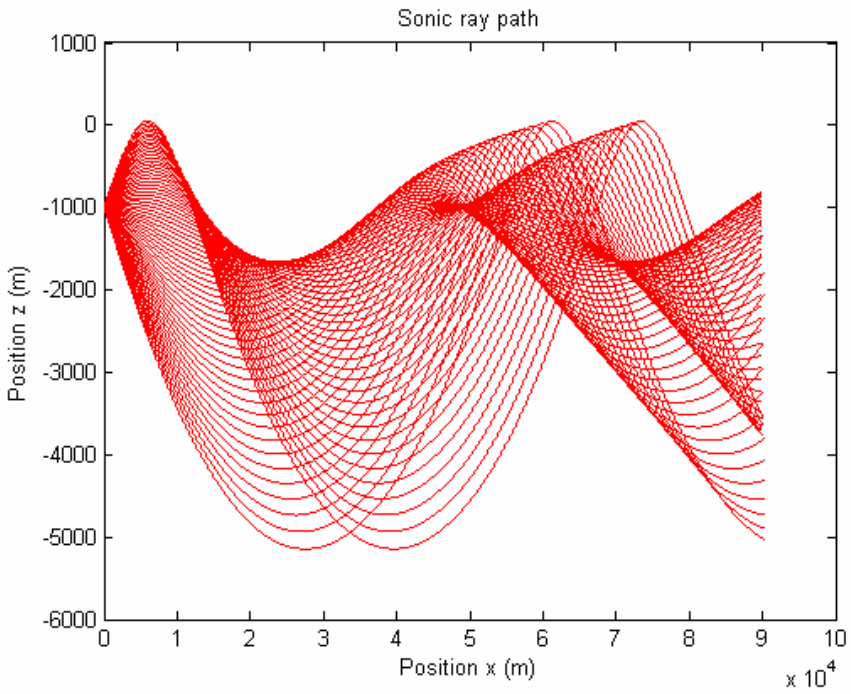

Figure 4.6

Propagation of the sonic ray in case of Munk's speed of sound profile. The figure shows the ray paths for initial angles of emission raging from -15 to 15 degrees.

In the real case the variation of the sound speed in the water is function of the depth and of the actual values of the medium environmental properties (pressure,

temperature, salinity). So the description of the propagation of the emitted sonic ray is function of its emission angle and of the speed of sound gradient components:

$$
\begin{aligned}
H(\vec{r}) &= \frac{\partial c(\vec{r})}{\partial x} \\
K(\vec{r}) &= \frac{\partial c(\vec{r})}{\partial y} \\
G(\vec{r}) &= \frac{\partial c(\vec{r})}{\partial z}
\end{aligned}
\tag{4.29}
$$

The method described before can now be extended allowing the variation of the sound speed as a function of the position. The equations 4.27 have been derived in the case of constant $\partial c/\partial z$ in the z direction but all the physical considerations still hold if the sound speed gradient is constant in any direction and the equation just need to be changed by a rotation in the three-dimensional space:

$$
\begin{aligned}
\theta_{n+1} &= \theta_n + (\sin(\theta_n)\cos(\varphi_n)H(x_n, y_n, z_n) - \sin(\theta_n)\sin(\varphi_n)K(x_n, y_n, z_n) - \cos(\theta_n)G(x_n, y_n, z_n))\Delta t \\
\varphi_{n+1} &= \varphi_n + (\cos(\varphi_n)H(x_n, y_n, z_n) - \sin(\varphi_n)K(x_n, y_n, z_n))\Delta t \\
x_{n+1} &= x_n + \cos(\theta_{n+1})\sin(\varphi_{n+1})c(x_n, y_n, z_n)\Delta t \\
y_{n+1} &= y_n + \cos(\theta_{n+1})\cos(\varphi_{n+1})c(x_n, y_n, z_n)\Delta t \\
z_{n+1} &= z_n + \sin(\theta_{n+1})c(x_n, y_n, z_n)\Delta t
\end{aligned}
$$

Those are the final equations used in the full three-dimensional ray tracing algorithm. This method is very useful to trace back the sound field, measured by an array of sensor, to the source. In particular the sound field can be evaluated using measured environmental data as function of position and time.

This approach is convenient if we want to trace back the sonic ray, taking into account the measured properties of the medium as a function of the position, from the sensors to the source, providing that the direction of arrival at the sensor is known. During the simulation phase, we want to propagate the signal from the cascade to the sensors. In this case it is wasteful, from a computational point of view, since it requires to propagate a large amount of sonic rays from the source and evaluate the time of arrival at the sensors using some kind of interpolation. In fact there is no way, with this

techniques, to known the ray parameters for which the sonic ray hits one specific sensor. A different approach is convenient to deal with the propagation from the source to the sensors.

If we restrict the propagation to the case of constant gradient in the z direction it is possible to evaluate exactly the ray parameter knowing the starting and ending point.

Let's suppose to have two points along the ray path P1 and P2 as shown in figure 4.3, recalling the results from the previous paragraph we know that the path is an arc of circle of radius $R = \frac{c_1}{G\cos(\theta_1)}$ we can write:

$$\begin{cases} D_O = \frac{c_1}{G}\tan(\theta_1) \\ Z_O = z_1 - \left|R\cos(\theta_1)\right| \\ R^2 = (d_2 - D_O)^2 + (z_2 - Z_O)^2 \end{cases} \tag{4.30}$$

where the subscript o indicate the centre of the circle. The last equation states that the points are on the same ray path and this path is a circle. Substituting we obtain:

$$\left(\frac{c_1}{G\cos(\theta_1)}\right)^2 = d_2^2 + \left(\frac{c_1}{G}\tan(\theta_1)\right)^2 - 2d_2\frac{c_1}{G}\tan(\theta_1) + (z_2 - z_1)^2 + \left(\frac{c_1}{g}\right)^2 + 2\frac{c_1}{G}(z_2 - z_1) \tag{4.31}$$

assuming that $\cos(\theta_1) \neq 0$ we can multiply both side by $\cos(\theta_1)^2$ obtaining:

$$\left(\frac{c_1}{G}\right)^2 = \cos(\theta_1)^2\left(d_2^2 + (z_2 - z_1)^2 + \left(\frac{c_1}{G}\right)^2 + 2\frac{c_1}{G}(z_2 - z_1)\right) + \sin(\theta_1)^2\left(\frac{c_1}{G}\right)^2 - \sin(\theta_1)\cos(\theta_1)2d_2\frac{c_1}{G} \tag{4.32}$$

this equation can be easily solved using the following substitutions:

$$\begin{cases} a = \left(d_2^2 + (z_2 - z_1)^2 + \left(\frac{c_1}{G}\right)^2 + 2\frac{c_1}{G}(z_2 - z_1) \right) \\ b = \left(\frac{c_1}{G}\right)^2 \\ c = 2d_2\frac{c_1}{G} \\ x = \cos(\theta_1) \\ y = \sin(\theta_1) \end{cases} \tag{4.33}$$

that leads to:

$$\begin{aligned} & ax^2 + b(1-x^2) - cxy - b = 0 \\ & ax^2 + b(1-x^2) \mp cx\sqrt{1-x^2} - b = 0 \\ & x\left((a-b)x \mp c\sqrt{1-x^2}\right) = 0 \\ & x = \pm\sqrt{\frac{c^2}{(a-b)^2 + c^2}} \end{aligned} \tag{4.34}$$

the ambiguity in the sign of $\cos(\theta_1)$ can be resolved by geometrical considerations. The condition $\cos(\theta_1) \neq 0$ means that the equations can be applied at maximum to half circle propagation and so the position of the ray along the d axis increases monotonically. Therefore if $d_2 \geq d_1$ we must chose the positive sign. The knowledge of $\cos(\theta)$ in one point of the path allows to know it in each point of the trajectory by means of the Snell law. The ambiguity in the sign of $\sin(\theta_{1,2})$ can be solved by direct substitution into eq 4.32.

5. Sound detection

In previous chapters the importance of underwater environment concerning the signal generation and its propagation towards the pressure sensor have been discussed. In this chapter the pressure sensors (hydrophones), their technical implementation and their limits as basic sensor for acoustic neutrino detection are reviewed. Moreover the underwater environment as source of noise is discussed in detail.

5.1. Hydrophones transducer

The hydrophones are underwater pressure sensors based on piezoelectric effect, this effect is the ability of some material to convert mechanical energy into electric energy (direct piezoelectric effect) and the opposite (inverse piezoelectric effect). To illustrate the piezoelectricity a brief review of the dielectric properties of materials is needed. An ideal dielectric does not have free charge carrier, when an electric field is applied to the material the positive and negative charge centres will move across the field line to form a dipole; as a consequence the material will elongate in the direction of the field line. This effect, common to all dielectric material, is known as electrostrictivity and for low value of the electric field, has a quadratic dependency on it. Some materials have a linear dependency on the electric field, the inverse piezoelectric effect; this is due to the absence of a centre of symmetry for the charge and so if a reverse field is applied the mechanical effect will not be invariant. In other words, to show the piezoelectric effect, the material must have an intrinsic polarization axis. Some crystals, depending on their structure, exhibit this effect but the stronger coupling between mechanical stress and electric field generated is typical of ferroelectric materials and in particular in polycrystalline ferroelectric ceramics, that are commonly used to build piezoelectric transducers. Those materials are made of domain in which there is a polarization axis but each domain is oriented in a random direction. As a result, a macroscopic piece of those ceramic does not have a defined axis. Above a characteristic temperature (Curie

temperature) each single domain exhibit a simple cubic symmetry with no dipole moment. In such case those ceramics behave like a normal dielectric and is possible to align the domains applying an external electric field. When the polycrystal is slowly cooled below the critical temperature, while maintaining the electric field, a permanent polarization axis along the electric field remains.

5.2. Equivalent hydrophones noise

A detailed description of the piezoelectric ceramic is very complex but many useful results can be obtained describing them as a simple electric circuit. In fig 5.1 the equivalent circuit for a piezoelectric transducer is shown, the sensibility of those transducer are expressed as function of their output voltage (Vo) and is clearly a function of frequency as reported in fig 5.2.

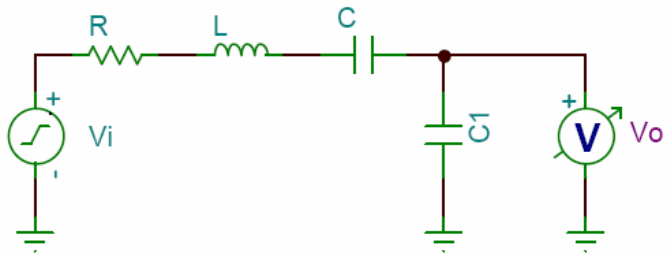

Figure 5.1

The equivalent circuit of an hydrophone.

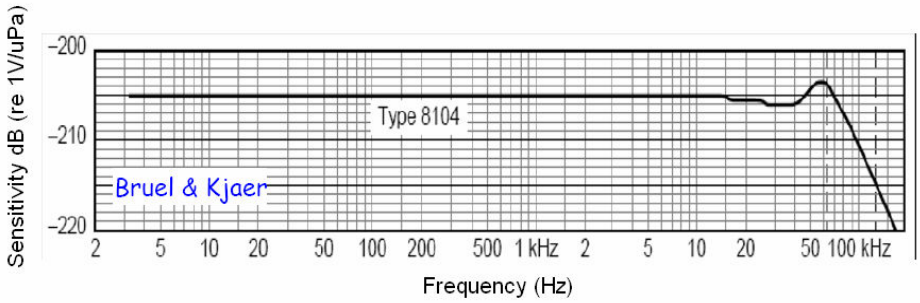

Figure 5.2

The sensitivity as a function of frequency for the trasducer type 8104 of Bruel&Kjaer constructor.[21]

This circuit is a second order low pass filter. If we define:

$$
\begin{aligned}
C_s &= \frac{C_1 C}{C_1 + C} \\
s_0 &= \frac{C}{C_1 + C} = \frac{C}{C_0} \\
\omega_0^2 &= \frac{1}{LC_s} \\
Q^2 &= \frac{L}{C_s R^2} \\
G &= \frac{1V}{1Pa}
\end{aligned}
\tag{5.1}
$$

it is possible to write its transfer function as:

$$
S(s) = \frac{Gs_0}{1 + \frac{s}{Q\omega_0} + \frac{s^2}{\omega_0^2}} \tag{5.2}
$$

This function shows a maximum at a frequency $\omega_{\max}$, defining $\xi = S(\omega_{\max}) / S(0)$ is possible to write:

$$
\begin{aligned}
\omega_{\max} &= \omega_0 \sqrt{1 - \frac{1}{2Q^2}} \\
\xi &= \frac{Q}{\sqrt{1 - \frac{1}{4Q^2}}}
\end{aligned}
\tag{5.3}
$$

This approach, and this variables definition, are useful in evaluating the ceramic characteristics from the parameters declared by the constructors. They quote the sensibility(Gs_0) in the low frequency limit, usually at 250 Hz, the value of C_0 and

provide the graphical representation of the transfer function (fig. 5.2) from which is possible to evaluate ω_{max} and ξ. As example the equivalent circuit for the ceramic showed in figure 5.2 is reported in figure 5.3.

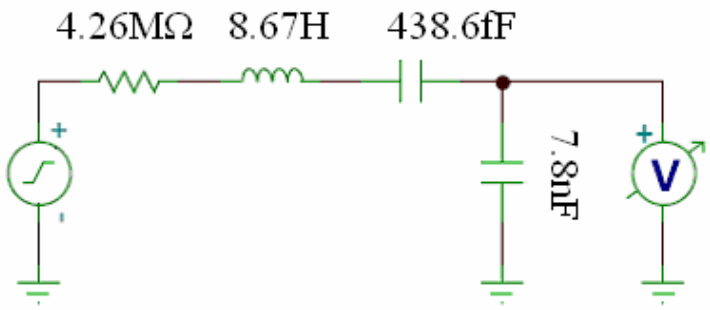

Figure 5.3

Calculated values of the equivalent circuit of the ceramic.

The only dissipative element of this model is the resistor, if its value is known is possible to evaluate the noise at the hydrophone output.

The power spectral density(PSD), injected in the circuit by the resistor, is $4KTR$ V^2/Hz; this PSD is filtered by the transfer function of the circuit and collected at the hydrophone output. The effective noise voltage at the output can be written as:

$$V_n = \sqrt{4KTR\frac{1}{2\pi}\int_0^{\infty}\frac{s_0^2}{\left(1-\frac{\omega^2}{\omega_0^2}\right)^2+\left(\frac{\omega}{Q\omega_2}\right)^2}d\omega} \tag{5.4}$$

recalling the definition of equivalent noise bandwidth as:

$$ENB = \frac{1}{2\pi}\int_0^{\infty}\frac{1}{\left(1-\frac{\omega^2}{\omega_0^2}\right)^2+\left(\frac{\omega}{Q\omega_2}\right)^2}d\omega = \frac{1}{4}Q\omega_0 \tag{5.5}$$

it is possible to write:

$$V_n = \sqrt{4 \cdot KRT \cdot s_0^2 \cdot ENB}$$
$$P_n = \frac{V_n}{Gs_0} = \sqrt{4 \cdot KRT \cdot ENB} \tag{5.6}$$

where P_n is the equivalent pressure noise level. The numerical values in our example, evaluated for a temperature of 14 Celsius degree, are:

$$V_n = 5nV$$
$$P_n = 95\mu Pa \tag{5.7}$$

P_n is the pressure for which the hydrophone voltage output is equal to its thermal noise. Although the specific values change for different commercial ceramics, the order of magnitude is related to the building technique and will not vary. The ceramic output is usually amplified to be acquired by an electronic front end. This will increase the equivalent pressure noise, how this will affect the measurements is strictly linked to the specific application, and will be neglected here. As a result it is possible to say that P_n is the minimum input pressure that can be distinguished by the noise using a single hydrophone.

5.3. Underwater noise

The underwater environment is an highly noisy ambient; the noise sources can be classified in three main groups: transient signal, stationary deterministic signals and stationary random signals. Stationary deterministic signals are entirely made up of sinusoids at discrete frequencies. In this case the power recorded by the sensor is independent of its bandwidth, assuming that the frequency of the signal is contained in it. Because of this the average frequency spectrum should be appropriately scaled in terms of mean square amplitude and would have units of Pa^2. The measurements can

also be scaled, and usually they are, as the root mean square amplitude(RMS). Figure 5.4 shows an example of deterministic stationary signal.

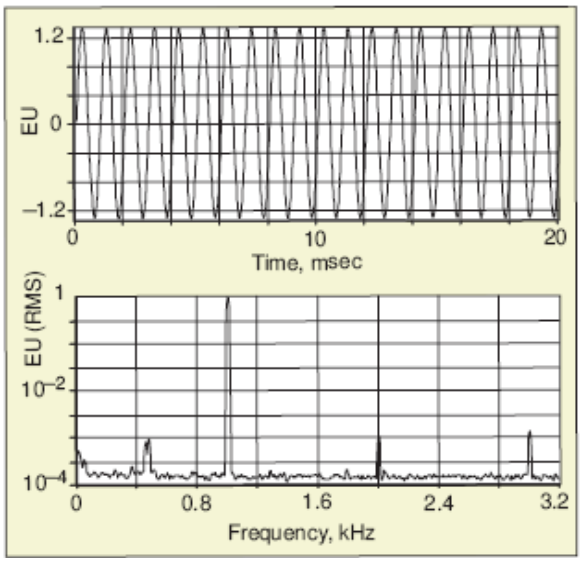

Figure 5.4

Stationary deterministic signal. EU is the generic measure unit in our case Pa.

Stationary random signals are sets of data having statistical properties that are invariant with respect to a translation in time. Those signals are continuous in frequency domain therefore the power associated with this noise sources is a function of the frequency band in which they are measured. In order to compare the properties of different sensors, in terms of their response to a stationary random noise, it is convenient to normalize the original pressure to the specific integration bandwidth. By dividing the acquired power to the sensor bandwidth we can then eliminate its influence. This normalized spectrum, often referred as the power spectral density (PSD), is a measure of the power per unit of frequency due to the signal. The unit for this type of measurements are expressed in Pa^2/Hz and usually the logarithm of this quantity, referred to $1\mu Pa^2/Hz$ is reported. In figure 5.5 a time series and a PSD of the series measurements is reported.

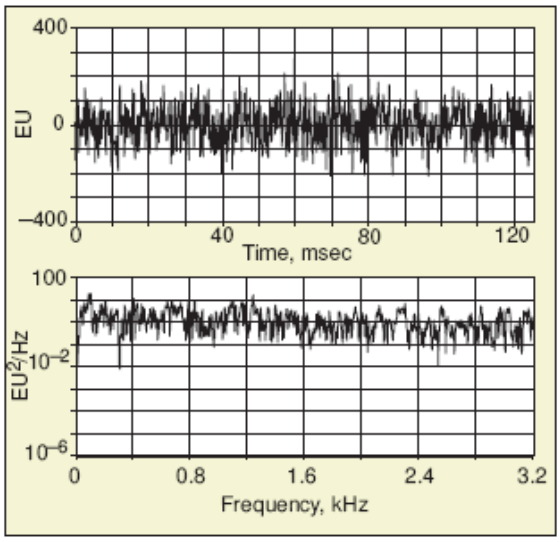

Figure 5.5

Stationary random signal. EU is the generic measure unit in our case Pa.

Transient signals(like the one expected by the UHE neutrinos) contain a finite amount of energy. Therefore, a transient signal cannot be characterized in terms of power. Indeed the spectral amplitude of a transient signal depends on the length of the time record. Since transients also have a spectrum continuously distributed over frequencies, the recorded power must be normalized with respect to the sensor bandwidth, just as PSD, but the measurements must be additionally re-scaled according to the acquisition time length. Thus the appropriate unit for the spectrum of a transient signal is the energy per unit of frequency which is referred as energy spectral density(ESD) with unit of $Pa^2 s/Hz$. Refer to fig 5.6 for an example of this type of signals.

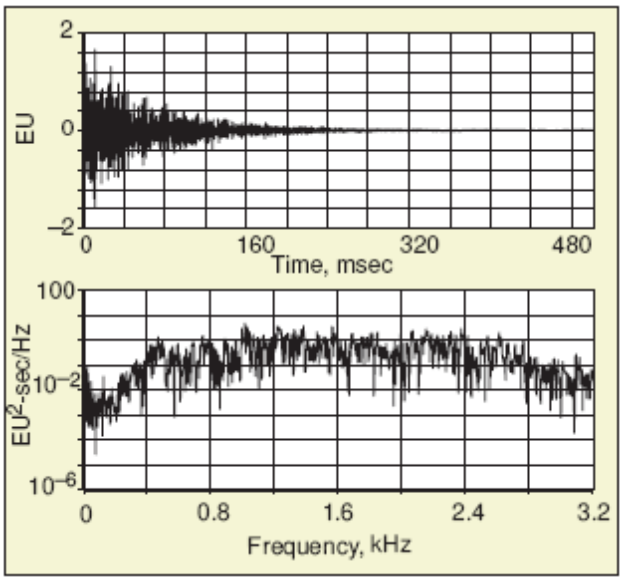

Figure 5.6

Transient signal. EU is the generic measure unit in our case Pa.

The ESD of a finite energy signal (i.e. square integrable) is defined as:

$$\phi(\omega) = \left| \frac{1}{\sqrt{2\pi}} \int_{-\infty}^{\infty} f(t) e^{-i\omega t} dt \right|^2 = \frac{F(\omega) F^*(\omega)}{2\pi} \tag{5.8}$$

where F is the continuous Fourier transform and F* is its complex conjugate.

For a stationary random signals the energy, defined above, has no sense, and then the ESD cannot be evaluated. However is always possible to define the PSD of an arbitrary time series of stationary random process, using the Wiener-Khinchin theorem, as the Fourier transform of the auto-correlation function:

$$S(f) = \int_{-\infty}^{\infty} R(\tau) e^{-2\pi i f \tau} d\tau \tag{5.9}$$

where R is the auto-correlation function defined as:

$$R(\tau) = \int_{-\infty}^{\infty} f(t+\tau) f^*(t) dt \tag{5.10}$$

All those kind of signals are present in the underwater environment. In figure 5.7 a classical noise spectrum, due to measurements at low depth[41], is shown.

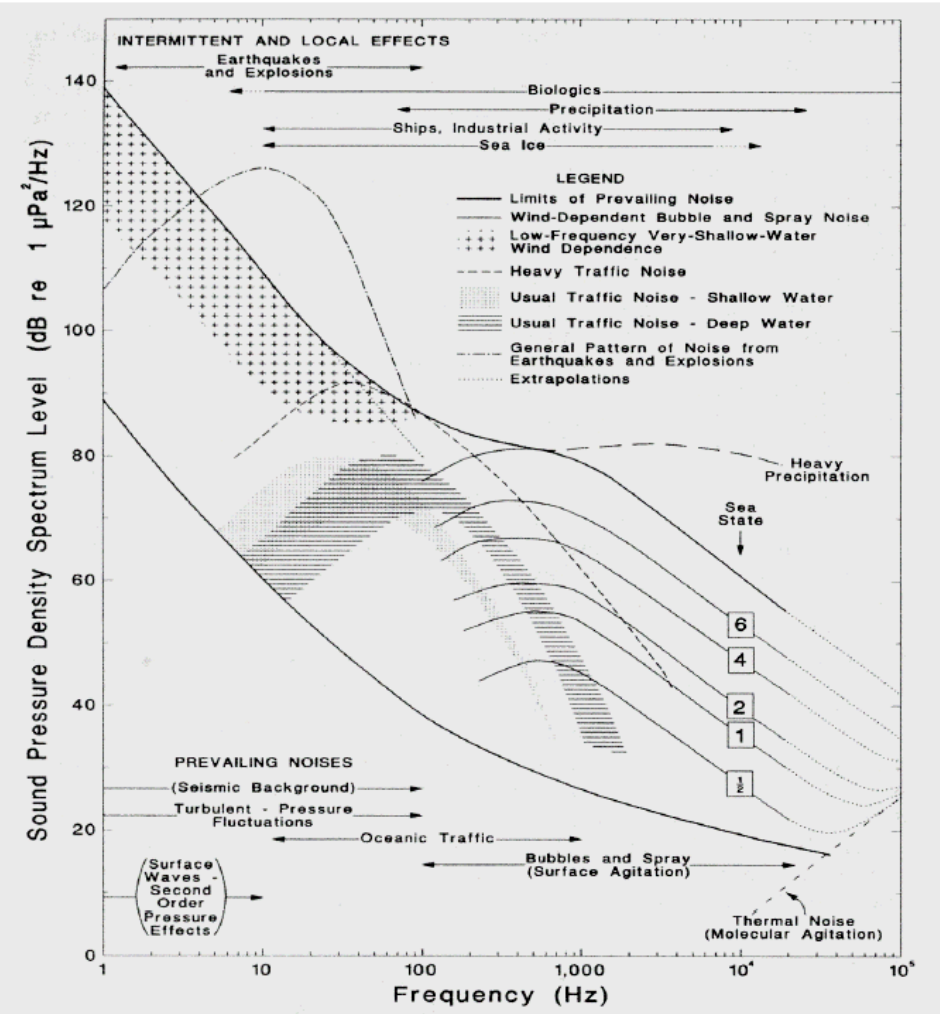

Figure 5.7

Power spectral density of underwater noise measured by Wenz in shallow water.

The major contributions to this spectrum, as function of frequency, can be summarized as follow:

1)below 10Hz. The main stationary noise source is the seismic background and the transient signals can be attributed to explosions or earthquakes.

2)between 10Hz and 2kHz. The diffuse noise is due to naval traffic and transients to ship motion.

Only a negligible part of the neutrino signal energy lies in this frequency regions while most of the ambient noise power is at low frequency.

3)between 2kHz and 40kHz. This is the most important and most variable region of the spectrum. The main contribution to stationary random signal in this region is due to wind and rain interactions with the sea surface; the variability is strictly linked to the weather conditions. Transient signals arise from ship cavitation, sonar and cetaceans, moreover quasi deterministic stationary signal are due to acoustic pinger usually working at 10kHz. In this frequency range lies most of the neutrino signal energy.

4)Above 40kHz. Only few data in this region are known in literature and none of them is recorded in deep water; anyway the main contribution to the PSD in this part of the spectrum is believed to arise from thermal noise of water molecules. This contribution, reported in figure 5.7 as extrapolation, has a dependency on frequency proportional to f^2 so dominates at high frequency.

A major source of information about the background noise in deep water is due to the $O\upsilon DE$ [42] experiment, realized in the framework of the NEMO collaboration. $O\upsilon DE$ is an acoustic station installed at the NEMO test site, 20km off the Sicily coast in front of Catania at depth of 2000m.

$O\upsilon DE$ is composed by an array of four hydrophones. An electronic system close to the hydrophones samples the hydrophones signal and transmit data over fiber optic to a laboratory on shore. The hydrophones signals are sampled at 96kHz. Since the main goal of this experiment is the characterization of the ambient noise as a function of time, due to limited storage capability, the data are stored on shore for 5 minutes each hour. The station has performed sound background monitoring from January 2005 up to November 2006. One of the most remarkable, and nearly unique, result obtained by $O\upsilon DE$ is the noise PSD measured in deep water(2000m) and reported in figure 5.9.

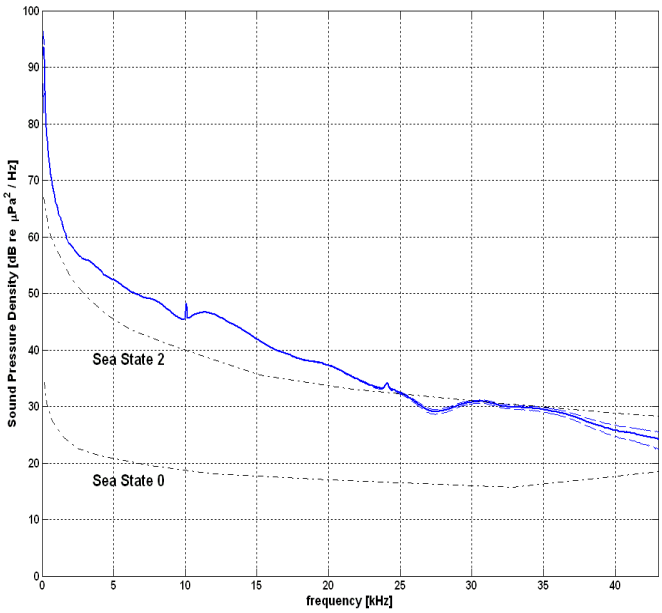

Figure 5.8

Average SPD measured at 2000 m depth with OnDE compared with bibliographic data (shallow depth).

Using this PSD is possible to evaluate the RMS of the noise in different frequency band:

$$NoiseRMS = \sqrt{\int_{f_1}^{f_2} PSD(f)df} \tag{5.11}$$

The results of such integration are reported in table 5.1 and show a noise level, in the frequency band of interest, of about 20mPa.

Frequency band (kHz)	Noise level(mPa)
2.5-5	36
5-10	27
10-20	14
20-40	7

Table 5.1
Noise level in mPa integrate d in different frequency bands.

In chapter 7 we'll show a method to detect signals whose amplitude is slightly less than the ambient noise, in any case the noise level pose a limit to the minimum amplitude of the acoustic signal that can be distinguished by the noise.

Since most of the noise in this region is due to the surface interaction with rain and wind it is possible to argue that this noise level will further decreases at higher depths. The variability of this noise has been studied during six months, from June to December 2005. In fig. 5.10 is represented the evolution of the noise level during this period.

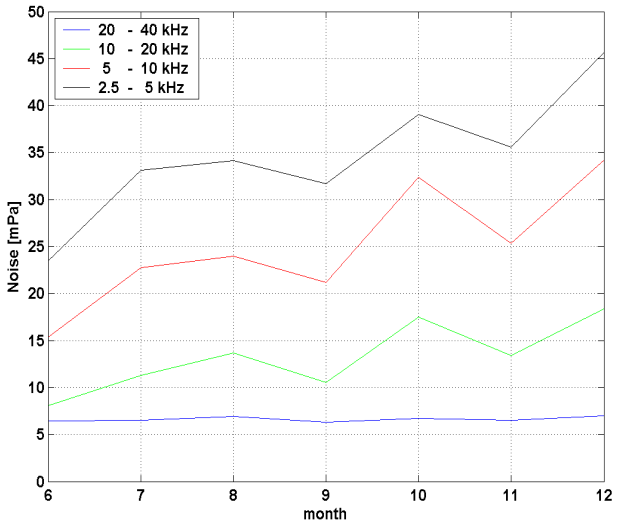

Figure 5.9

Noise level integrated in different frequency bands, the month number strat from june and end at december.

During this period an increases of the noise level is clearly visible in all the frequency band below 20kHz. This is compatible with the seasonal variability of the weather condition but also biological factors and human made noise, mainly due to navigation, play a role.

6. Detection algorithm

The aim of this work is to develop an algorithm that can be apply to an underwater array of hydrophones to detect the acoustic signal produced by the shower induced by neutrino interaction in water. In this chapter an outlook of the detection algorithm is given.

6.1. Strategy outlook

We need to find, in an highly noisy environment, a faint signal of known but variable shape as a function of the shower distance and the relative orientation of the shower and the hydrophone. Instead of reject the "noise" which is highly variable in shape and quite difficult to characterize, we decide to look for an algorithm that increase the signal or better the signal to noise ratio(SNR). This can be done, with different algorithms, both for the single hydrophone and for an array of hydrophones.

6.2. Approach for the single hydrophone

At level of a single hydrophone the only information that can be used is the knowledge of the signal shape. So we need to find a way to detect a known shape in an environment where the amplitude of our signal is small compared to the amplitude of other signals of different origin. This problem is very similar to the one encounter in radar systems where a known pulse is actively send and its delayed echo is measured. Even if the approach is substantially the opposite, in our case the pulse is not generated by our system but it's just recorded, the analysis technique can be the same. The use of the so called "matched filter" is a common choice in radar system and a convenient choice in our case. The main difference is that, in our case, the signal shape is computable but not fixed because it varies as function of the distance traveled and the

emission angle. A detailed discussion of the matched filter and its particular implementation in our specific case is discussed in chapter 7.

6.3. Approach for array of hydrophones

The gain in using an array of hydrophones instead of a single one is due to the possibility to correlate the signal in different hydrophones. If we know the position of the source and have an adequate propagation algorithm, we can correlate the difference in time of arrival at different points in space and time. However this approach can't help us in increase the SNR, in fact knowing the time of arrival of the pressure waves at different hydrophones, means that we are able to clearly detect the acoustic pulse at level of the single hydrophone. Instead we need a way to correlate different data flows from sensors and combine them into an unique one in which is possible to detect a signal that can't be see by a single sensor. The solution I propose in this work is the "Beam-Forming" technique. The beam-Forming is a MISO (Multi Input Single Output) technique originally develop to passively detect submarine with an underwater array of hydrophones. This technique combines the output of different sensors, with appropriate time delays according to the geometry of the array, into an unique data flow in which all the signals arriving from a specific direction are coherently summed. In chapter 8 the Beam-Forming is reviews, its performance evaluated and the computational power, needed to apply this technique, is discussed.

7. Matched filter

In this chapter the matched filter detection algorithm is reviewed[43-47], its implementation discussed and results from simulation of the detection algorithm at level of single hydrophone are given.

7.1. Optimal linear filter

Suppose that the time series of hydrophone samples $x(t)$ consist of a white noise $n(t)$ and a transient signal $s(t)$ of known shape that can be present or not in the time series. We want to apply a linear filter on $x(t)$ in such a way that the ratio of the power at filter output $y(t)$, when the signal is present, over the same quantity, when there is only noise at input, is maximum. The situation is reported in figure 7.1.

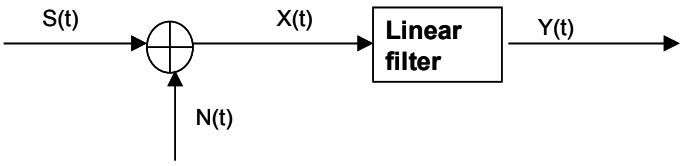

Figure 7.1

The input of the linear filter is a combination of a noise source and a signal of known shape.

Assuming that $n(t)$ is stationary white noise with power density $N_0/2$ and $G(i2\pi f)$ is the transfer function of the linear filter, the noise spectrum at the output of the filter is $N_0 G(i2\pi f)/2$; the power at the filter output is:

$$\frac{N_0}{2}\int_{-\infty}^{\infty}\left|G(i2\pi f)\right|^2 df \qquad (7.1)$$

and is not dependent on time. Further, if $S(i2\pi f)$ is the input signal spectrum the output signal spectrum is $S(i2\pi f)G(i2\pi f)$ and the filter output at time t^*, in which the transient signal is present, is:

$$y(t^*) = \int_{-\infty}^{\infty} S(i2\pi f)G(i2\pi f)e^{i2\pi ft^*}\,df \tag{7.2}$$

The ratio of the square of 7.2 to 7.1 is the power ratio we want to maximize:

$$r = \frac{\left[\int_{-\infty}^{\infty} S(i2\pi f)G(i2\pi f)e^{i2\pi ft^*}\,df\right]^2}{\frac{N_0}{2}\int_{-\infty}^{\infty}|G(i2\pi f)|^2\,df} \tag{7.3}$$

since the numerator of this ratio is real (is the filter output at time t^*), using the Schwarz inequality we can write

$$\left[\int_{-\infty}^{\infty} S(i2\pi f)G(i2\pi f)e^{i2\pi ft^*}\,df\right]^2 \le \int_{-\infty}^{\infty}|G(i2\pi f)|^2\,df\int_{-\infty}^{\infty}\left|S(i2\pi f)e^{i2\pi ft^*}\right|^2\,df \tag{7.4}$$

and substituting 7.4 into 7.3 we obtain

$$r \le \frac{2}{N_0}\int_{-\infty}^{\infty}|S(i2\pi f)|^2\,df \tag{7.5}$$

but recalling that $S(i2\pi f)$ is the transient signal energy density spectrum we can rewrite inequality 7.5 as $r \le 2E/N_0$ where E is the signal energy. It is clear that equality in eq 7.4 holds if

$$G(i2\pi f) = kS^*(i2\pi f)e^{-i2\pi ft^*} \tag{7.6}$$

that is, except for a possible amplitude and phase delay, the transfer function of a matched filter is the complex conjugate of the spectrum of the signal to which it is matched. If the noise $n(t)$ is not white but has an arbitrary power density spectrum $|N(i2\pi f)|^2$ a similar derivation is possible that leads to the solution:

$$G(i2\pi f) = \frac{kS^*(i2\pi f)e^{-i2\pi ft^*}}{|N(i2\pi f)|^2} \tag{7.7}$$

This can be understood in the following manner: suppose that the input $x(t)$ is passed through a two filters, a noise-whitening filter with transfer function $1/N(i2\pi f)$ and a matched filter. The noise component, at the output of the first filter, will be white but the signal will be distorted and its spectrum will be $S(i2\pi f)/N(i2\pi f)$; so the transfer function of the matched filter for this distorted signal will be (eq. 7.6):

$$G(i2\pi f) = \frac{kS^*(i2\pi f)e^{-i2\pi ft^*}}{N^*(i2\pi f)} \tag{7.8}$$

the cascade of those two filters has the transfer function reported in eq. 7.7

In conclusion the matched filter is the linear filter that maximize the ratio 7.3 and so the optimal linear filter that can discriminate a transient signal of known shape from a noise background of known spectrum.

The simplest scheme of detection system is reported in fig. 7.2 in the following of this paragraph we'll show how to correlate the threshold to the signal energy and the noise level.

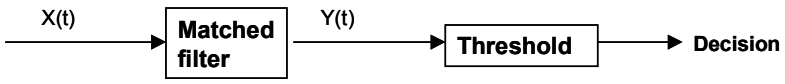

Figure 7.2

Logical scheme of the simplest detection system. The output of the matched filter is compared with a threashold to decide if the signal is present or not.

Let us examine the simplest hypothesis testing problem: the observed signal $x(t)$ is due to noise or to noise and a known signal. We denote the hypothesis of solely noise with H_0 and the alternative hypothesis with H_1; we want to derive a test for deciding in favour of H_0 or H_1. Defining $p_0(x)$ the probability that if H_0 is true the observed waveform is $x(t)$ and $p_1(x)$ the probability that if H_1 is true the observed waveform is $x(t)$ we can write our test as:

$$\begin{cases} \dfrac{p_1(x)}{p_0(x)} > \alpha \Rightarrow H_1 true \\ \dfrac{p_1(x)}{p_0(x)} \le \alpha \Rightarrow H_0 true \end{cases} \tag{7.9}$$

where α is a constant and do not depend on $x(t)$. This test means that we believe that H_1 is true if the observed waveform $x(t)$ is α time more likely to occur if H_1 is true than if H_0 is true.

Let us assume that the noise $n(t)$ is stationary white noise with power density $N_0/2$ and the transient signal, if present, has the known shape $s(t-t_0)$ in the time interval $t_0 \le t \le t_0 + \Delta T$. Then, observing the waveform $x(t)$ in an observation time I, containing the interval $t_0 \le t \le t_0 + \Delta T$, leads to the following two hypothesis:

$$\begin{aligned} &H_0 : x(t) = n(t) \\ &H_1 : x(t) = n(t) + s(t-t_0) \end{aligned} \tag{7.10}$$

It is possible to show, in the case of white noise, that the probability of observing a waveform $w(t)$ of duration $\Delta T = t_2 - t_1$, due to the contribution of noise only is:

$$p(w) = k \exp\left[-\frac{1}{N_0} \int_{t_1}^{t_2} w(t)^2 \, dt \right] \tag{7.11}$$

so in our case we can write:

$$p_0(x) = k \exp\left[-\frac{1}{N_0} \int_I x(t)^2 \, dt \right] \tag{7.12}$$

Similarly, $p_1(x)$ can be computed evaluating the probability that the noise can assume the form $x(t) - s(t - t_0)$ and so:

$$\begin{aligned} p_1(x) &= k \exp\left[-\frac{1}{N_0} \int_I [x(t) - s(t - t_0)]^2 \, dt \right] \\ &= k \exp\left[-\frac{1}{N_0} \int_I x(t)^2 \, dt + \frac{2}{N_0} \int_I x(t) s(t - t_0) dt - \frac{E}{N_0} \right] \end{aligned} \tag{7.13}$$

where E is the energy of the signal and is equal to $\int_I x(t)^2 \, dt$. Substituting 7.12 and 7.13 in 7.9 and taking the logarithm of both sides lead to:

$$\begin{cases} y(t_0) > \beta \Rightarrow H_1 true \\ y(t_0) \le \beta \Rightarrow H_0 true \end{cases} \tag{7.14}$$

where we have defined

$$\begin{aligned} y(t_0) &= \int_I x(t) s(t - t_0) dt \\ \beta &= \frac{N_0}{2} \log(\alpha) + 2E \end{aligned} \tag{7.15}$$

Changing variable in 7.15 by setting $\tau = t_0 - t$ leads to

$$y(t_0) = \int_{-\Delta T}^{0} s(-\tau) x(t_0 - \tau) dt \tag{7.16}$$

this means that $y(t_0)$ is the output, at time t_0, of a linear filter with impulse response $s(-\tau)$. Recalling eq 7.6 and the fact that the transfer function of a linear filter is the Laplace transform of its impulse response, we can conclude that $y(t_0)$ is the output at time t_0 of a matched filter that is matched to $s(t)$ and β is the threshold level that can be used to discriminate among the two hypothesis H_0 and H_1.

7.2. Simulation results

The matched filter is the optimal linear filter assuming that the signal shape is known, in figure 7.3 an example of bipolar pulse added to white Gaussian noise is given and the output of the matched filter is shown.

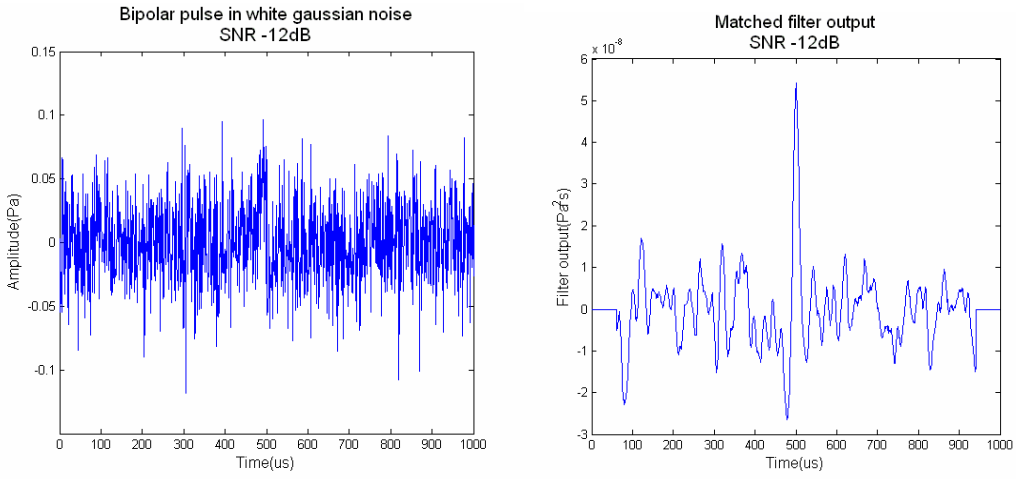

Figure 7.3

An example of matched filter applied to a time series of white gaussian noise with a bipolar pulse added at the middle of the series. The sampling frequency is 1Msps and the SNR of this example is -12dB. The presence of the bipolar pulse is clearly visible at the outpout of the matched filter.

The filter performance in presence of non white, slowly varying noise can't be computed analytically. To evaluate them we perform the following numerical simulation. We take time windows, 1ms length, of real data, acquired by $O\upsilon DE$, and evaluate the noise PSD. Subsequently we simulate the acoustic pulse at 1km from the shower and 0 degrees of emission angle and scale it according to the desired SNR.

Using the noise PSD and the signal shape we compute the filter's coefficients and the threshold; then we add the signal to the noise time window and analyse it with the filter. The time at which the filter's output is over-threshold is taken as the reconstructed hit time; if the difference of the reconstructed time with the nominal one is equal or less then one sample, the hit is assumed as well discriminated by the noise. This procedure is repeated 10^4 times for each SNR. The result of this simulation is shown in figure 7.4. The probability to correctly reconstruct the hit time is above 99.97% for SNR higher than -6dB.

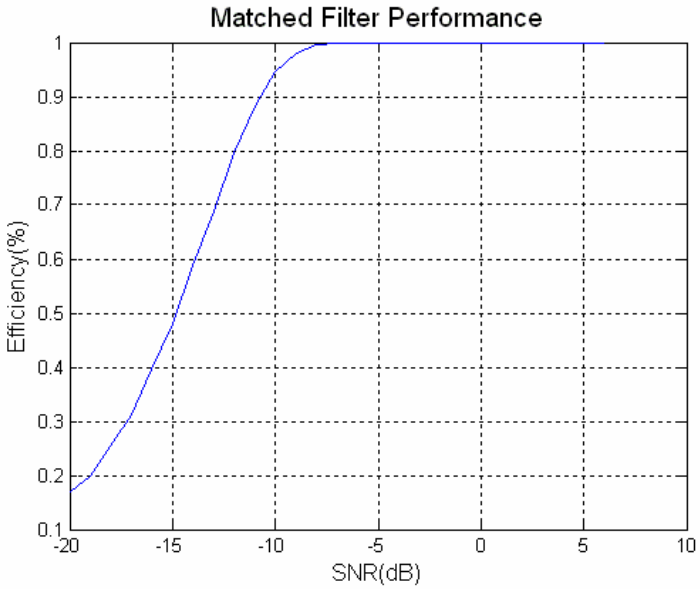

Figure 7.4

The efficiency of the matched filter as function of the SNR in case of non white and slowly varying noise.

As we discussed in the chapters 3 and 4 the shape of the acoustic signal is a function of both the emission angle and the distance travelled. In principle the same hydrophone's output must be analysed with one matched filter for each possible signal shape; in any practical implementation is possible to apply only a limited numbers of matched filters with worse overall performances. To evaluate the number of filter that we need to apply to the hydrophone's output we performed a simulation. As shown in figure 7.3 and discussed in chapter 5 the output of the filter is expressed in $Pa^2 s$ and, as is obvious, the filter's output is a function of the signal amplitude and duration; this means that we can't compare directly the output of two different filters because even if

each of them match perfectly the corresponding signal, their output will be, in general, different in amplitude. To compare different filters and the performance of a single filter as function of the signal parameters (emission angle and distance travelled) we must normalize conveniently both the signal and the filter. Since the peak amplitude of the filter output is proportional to the signal energy a convenient choice, to compare the performance of the matched filter with different signals, is to normalize the signal energy. If the acoustic signal has a shape in time described by $x(t)$ then it will be normalized by $y(t) = x(t)/x_0$ with $x_0 = \sqrt{\int_{-\infty}^{\infty} |x(t)|^2 dt}$; the same normalization is used for the filter. This approach means that all the signal have unitary energy regarding their shapes and the filter's output can therefore be considered as the filter "efficiency". In figure 7.5 the performance of the matched filter as function of the distance travelled by the pressure wave is reported. We built six different filters that match the assumed shape of the signal with an emission angle of 0 degrees and different distances travelled: 1,5,10,15,20 and 25km. Then we generates the acoustic signal and propagates it for an arbitrary distance from 1km to 50km. The matched filters are applied to the signal and their peak amplitude is recorded. The simulation was reduced to 50km because, as discussed in chapter 4, the possibility to measure an acoustic pulse at distance grater than this is remote. As it is possible to see in figure 7.5 a very limited number of filters guarantee an "efficiency" above 90% over a wide range of distances. The same procedure has been applied to evaluate the "efficiency" of the filter as function of the emission angle, for a fixed distance travelled of 1km; the results are reported in fig. 7.6; in this case the simulation is reduced to the range $\pm 3^0$ because, as it is possible to see in figure 3.12, the amplitude of the acoustic signal decreases of about one order of magnitude in this angular range so the possibility to detect an acoustic signal out of this range is very unlikely.

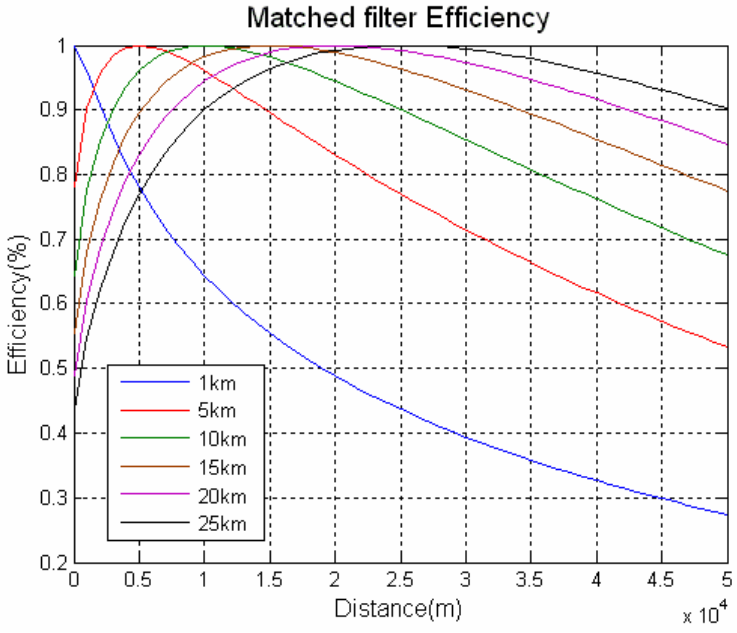

Figure 7.5

The matched filter performance as function of the distance traveled by the pressure wave for fixed emission angle (0 degrees). Different colors represents the output of different filters which have maximum efficiency at 1,5,10,15,20 and 25km.

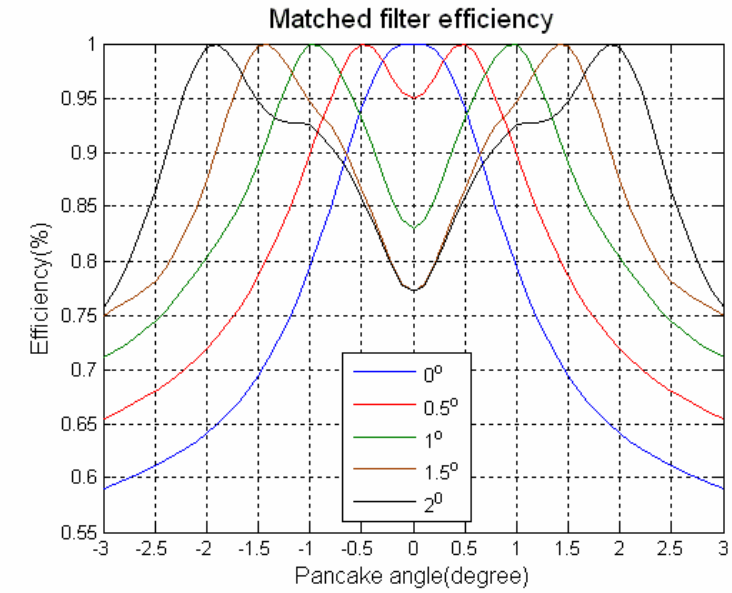

Figure 7.6

The matched filter performance as function of the emission angle of the pressure wave for fixed distance travelled (1km). Different colors represents the output of different filters which have maximum efficiency at 0,0.5,1,1.5 and 2 degrees.

7.3. Practical consideration

The simulation discussed in the previous paragraph shows the performance of the matched filter as a function of the signal shape and noise level; fixing the desired "efficiency" is possible to evaluate the number of filters needed to cover the signal parameters space. However to design a system that is possible to realize is necessary to evaluate the computational power needed to apply each filter. Suppose that the hydrophone is sampled with a frequency F_S and let ΔT be the time length of the acoustic signal, in this case the signal length in sample as well as the filter length are:

$$S = F_S \Delta T \tag{7.17}$$

each sampling time $T_C = 1/F_S$ the output of the filter $y(t_n)$ must be computed as:

$$Y(t_n) = \sum_{i=-S/2}^{+S/2} x(t_i) h(t_{n-i}) \tag{7.18}$$

where h is the filter impulse response. So the total number of addition and multiplication needed per unit of time are:

$$N = F_S^2 \Delta T \tag{7.19}$$

For $\Delta T = 120 \mu s$ and $F_S = 200 Ksps$ the total computational power for each filter is 9.6MFLOPS (millions of FLoating Point Operation Per Second). As reference the computational power of commercial digital signal processor (DSP), commonly used in audio application to implements digital filters have a computational power of few hundreds of MFLOPS and a commercial pentium quadcore have a power of tens of GFLOPS. A reasonable number of filters, three for the distance and three for the emission angle for a total of 9 filters seems a reasonable compromise to retains an efficiency above 90% over all the parametric space with an affordable computational power.

In fig. 7.7 the logical scheme of the single hydrophone analysis is shown. The noise spectrum is measured periodically every few minutes since, as discussed in chapter 5, it's supposed to vary on daily or seasonal scale and the probability to evaluate one noise spectrum with the signal is very unlikely. The noise spectrum is used to evaluate the filter coefficients and the threshold for the filter's output as discussed in paragraph 7.1.

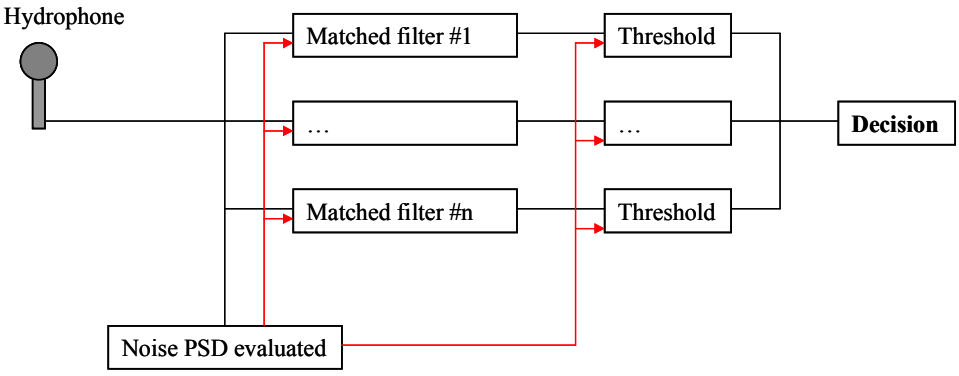

Figure 7.7

Data analisys of a single hydrophone output. The noise PSD is evaluated periodically and is used to compute the n matched filters and their thresholds. The filter's outputs are used to decide if the time series is or not noise.

The hydrophone's samples are analysed by different matched filters and their output are used to decide if the time series contains the signal; moreover the different outputs can be used to have an hint on the distance and the emission angle. We note that apply different filters to the same data stream increase consequently the data rate of each hydrophone, so this approach assume that a decision, with the whole data rate, is taken at level of single hydrophone.

The conclusion are that is possible, using a reasonable computational power to apply to each hydrophone a sufficient number of filter to cover the parametric space of the signal with an efficiency above the 90%, moreover the single filter is able to clearly discriminate(at 3σ level) the signal from the noise with a SNR of about -6dB even if the noise is non white and slowly varying in time.

8. Beam-Forming

In this chapter we discuss the beam-forming[48-51]. This technique analyze the data acquired by an array of sensors to compute the arrival direction of the incident waves. The array of sensors sample the wave-front in space and time and the samples of different sensors are combined to sum up coherently all the waves arriving on the array from a specific direction.

8.1. Delay and sum Beam-Forming

Assuming that the array is composed by N sensors located at position $\vec{p}_n$, with n=0,...,N-1, and defining the vector of signals as:

$$\vec{x}(t) = \begin{pmatrix} x_0(t) \\ ... \\ x_{N-1}(t) \end{pmatrix} \tag{8.1}$$

where $x_n(t)$ is the signal acquired by the nth hydrophone at position $\vec{p}_n$, we can process each sensor output by a linear filter, with impulse response $h_n(\tau)$, and sum up the results to obtain the array output:

$$y(t) = \sum_{n=0}^{N-1} \int_{-\infty}^{\infty} h_n(t-\tau) x_n(\tau) d\tau \tag{8.2}$$

Defining the vector $\vec{h}(\tau)$ as:

$$\vec{h}(\tau)=\begin{pmatrix} h_0(\tau) \\ ... \\ h_{N-1}(\tau) \end{pmatrix} \tag{8.3}$$

we can rewrite eq. 8.2 as:

$$y(t)=\int_{-\infty}^{\infty}\vec{h}^{T}(t-\tau)\vec{x}(\tau)d\tau \tag{8.4}$$

which can be rewritten in the frequency domain as:

$$Y(\omega)=\int_{-\infty}^{\infty}y(t)e^{-j\omega t}dt=\vec{H}^{T}(\omega)\vec{X}(\omega) \tag{8.5}$$

where

$$\vec{H}(\omega)=\int_{-\infty}^{\infty}\vec{h}(t)e^{-j\omega t}dt \tag{8.6}$$

and

$$\vec{X}(\omega)=\int_{-\infty}^{\infty}\vec{x}(t)e^{-j\omega t}dt \tag{8.7}$$

In this analysis technique, known as “delay and sum beam-forming”, the signals from different sensors are properly delayed in time and then added to coherently sum up the signal measured by sensors. In this case we can write:

$$h_n(\tau)=\frac{1}{N}\delta(\tau-\tau_n) \tag{8.8}$$

substituting eq. 8.8 into eq. 8.2 we obtain:

$$y(t) = \sum_{n=0}^{N-1} \int_{-\infty}^{\infty} h_n(t-\tau) x_n(\tau) d\tau = \sum_{n=0}^{N-1} \frac{1}{N} x_n(t-\tau_n) \tag{8.9}$$

if the delays are calculated so that $x_n(t-\tau_n) = x_m(t-\tau_m) = x(t)$ the signal sampled by all the sensors is summed coherently and the array response is $y(t) = x(t)$. We note that in the case in which an incoherent noise term is added to the signal, it will be reduced, in the array response $y(t)$, by a factor $1/N$. In paragraph 8.5 we'll show in details how to optimize the array to increase the SNR.

8.2. Array response function

To evaluate the array performance it is important to analyse its response to a plane wave. The array response to a general pressure waves can be evaluated by knowing its impulse response function $\vec{h}(\tau)$. If the plane wave has a frequency ω and a wave-number $\vec{k}$, the signal at sensor n will be equal to:

$$x_n(t) = e^{j(\omega t - \vec{k}^T \vec{p}_n)} \tag{8.10}$$

Defining the array manifold vector as:

$$\vec{v}(\vec{k}) = \begin{pmatrix} e^{-j\vec{k}^T \vec{p}_0} = e^{-j\omega\tau_0} \\ \dots \\ e^{-j\vec{k}^T \vec{p}_{N-1}} = e^{-j\omega\tau_{N-1}} \end{pmatrix} \tag{8.11}$$

where $\tau_n = \dfrac{\vec{k}^T \vec{p}_n}{\omega}$ are the propagation delays from the origin of the coordinate system to the sensor n. Substituting eq. 8.10 into 8.4 and recalling eq. 8.1 and eq. 8.11 we can write:

$$y(t) = \int_{-\infty}^{\infty} \vec{h}^T(t-\tau) \cdot \vec{x}(\tau) d\tau = \int_{-\infty}^{\infty} \vec{h}^T(t-\tau) \cdot \vec{v}(\vec{k}) e^{j\omega\tau} d\tau \tag{8.12}$$

making the substitution $\tau' = t - \tau$ and performing the integration we obtain:

$$y(t) = \vec{H}^T(\omega) \vec{v}(\vec{k}) e^{j\omega t} \tag{8.13}$$

it is convenient to define the frequency wave-number response as:

$$\Phi(\omega, \vec{k}) = \vec{H}^T(\omega) \vec{v}(\vec{k}) \tag{8.13a}$$

that represents the complex array gain to an input plane wave of frequency ω and wave-number $\vec{k}$. Moreover it is useful to define the Beam-Pattern as the array response to plane waves. The beam-pattern is a function of the propagation direction:

$$B(\omega, \theta, \varphi) = \Phi(\omega, \vec{k})_{\vec{k} = \frac{2\pi}{\lambda} \vec{a}(\theta, \varphi)} \tag{8.13b}$$

where $\vec{a}(\theta, \varphi)$ is a unit vector with spherical coordinate θ, φ.

8.3. Phased array

We start discussing the array response to a specific class of signals: the narrow-band signals. This signal has an energy spectrum as the one reported in fig. 8.1, their spectrum is band limited around some frequency ω_s so we can assume that the spectrum is 0 outside a frequency interval defined as:

$$|\omega - \omega_s| \leq \pi B_s \tag{8.14}$$

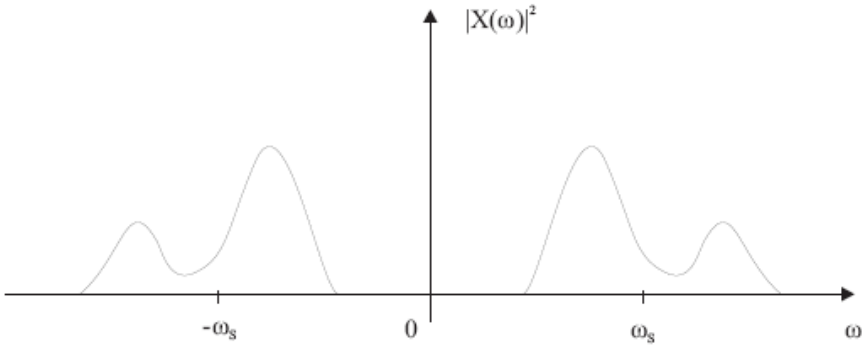

Figure 8.1

The energy spectral density of a narrow-band signal.

It is clear that the signal $x(t)$ is completely defined by the base band spectrum $|S(\omega)|^2$ reported in figure 8.2.

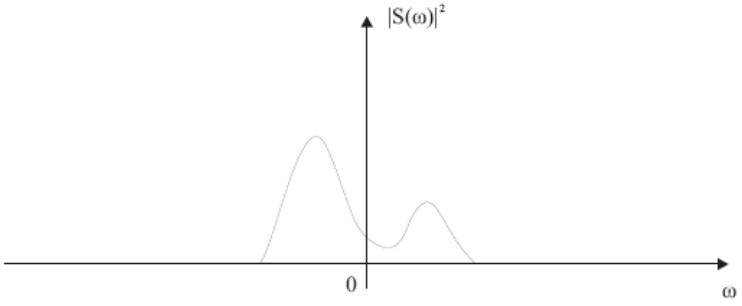

Figure 8.2

Base band energy spectrum density for a narrowband signal.

If we call $s(t)$ the signal in the base band associated with $x(t)$ we can write:

$$X(\omega) = S(\omega - \omega_s) + S^*(-(\omega - \omega_s))$$
$$x(t) = \frac{1}{2\pi}\int_{-\infty}^{\infty}\left[S(\omega - \omega_s) + S^*(-(\omega - \omega_s))\right]e^{j\omega t}\,d\omega = s(t)e^{j\omega_s t} + \left[s(t)e^{j\omega_s t}\right]^* \tag{8.15}$$

The signal measured by the sensor n will be:

$$x_n(t) = 2\,\mathrm{Re}\left(s(t-\tau_n)e^{j\omega_s(t-\tau_n)}\right) \tag{8.16}$$

If $B_s \Delta T_{\max} << 1$ where $\Delta T_{\max}$ is the maximum travel time between the array sensors it is possible to rewrite eq. 8.16 as: $x_n(t) = 2\,\mathrm{Re}\left(s(t) e^{j\omega_s t} e^{-j\omega_s \tau_n}\right)$.

This approximation means that the time delays can be substituted by phase shifts. Therefore the "delay and sum beam-forming", in this approximation, can be obtained by combining the sensors output with complex weights(w_n) so eq. 8.2 becomes:

$$y(t) = \sum_{n=0}^{N-1} w_n x_n(t) = \vec{w} \cdot \vec{x} \tag{8.17}$$

8.4. Uniform Linear Array

An uniform linear array (ULA) is an array of m elements on a line, with equal inter-element spacing d. In fig. 8.3 a scheme of those type of arrays is shown.

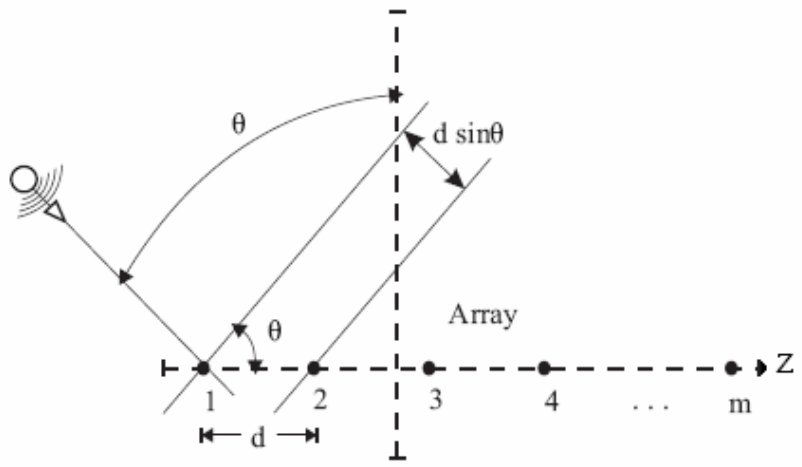

Figure 8.3

An array of linear equispaced sensors with inter-element space d. For notation convenience the array is aligned with the z axis.

Using the geometry reported in figure 8.3 it is possible to write the position of sensors, $\vec{p}_n$ and the array manifold vector $\vec{v}\left(\vec{k}\right)$ as:

$$\vec{p}_n = \begin{pmatrix} 0 \\ 0 \\ \left(n - \frac{m-1}{2}\right)d \end{pmatrix} \tag{8.18}$$

$$\vec{v}\left(\vec{k}\right) = \begin{pmatrix} e^{j\left(\frac{m-1}{2}\right)k_z d} \\ e^{j\left(\frac{m-1}{2}-1\right)k_z d} \\ \dots \\ e^{-j\left(\frac{m-1}{2}\right)k_z d} \end{pmatrix} \tag{8.19}$$

where $k_z = -\frac{2\pi}{\lambda}\cos(\theta)$. We note that since the geometry of the array is invariant under rotation around the z axis, this kind of arrays can just measure the projection of the wave-number vector on the z axis. With the above sensors position and manifold vector it is possible to write the frequency wave-number response function as:

$$\Phi\left(\omega, k_z\right) = \vec{w} \cdot \vec{v}\left(\vec{k}\right) \tag{8.20}$$

in the case of uniform weight $\vec{w} = \frac{1}{m}\left[1 \dots 1\right]^T$ the equation 8.20 can be rewritten as:

$$\Phi\left(k_z\right) = \frac{1}{m}\sum_{0}^{m-1} e^{j\left(n-\frac{m-1}{2}\right)k_z d} = \frac{1}{m}\frac{\sin\left(mk_z\frac{d}{2}\right)}{\sin\left(k_z\frac{d}{2}\right)} \tag{8.21}$$

The beam pattern corresponding to a physical angle θ can be written as:

$$B(\theta)=\frac{1}{m}\frac{\sin\left(\frac{m\pi}{\lambda}\cos(\theta)d\right)}{\sin\left(\frac{\pi}{\lambda}\cos(\theta)d\right)} \tag{8.22}$$

Usually we want that the sensors output is phased when the incident wave arrives on the array from a specific direction θ_s (the steering angle), this can be obtained by introducing the correct time delays in the manifold vector:

$$\vec{v}\left(\vec{k}\right)=\begin{pmatrix} e^{j\left(\frac{m-1}{2}\right)\left(k_z-k_z^s\right)d} \\ e^{j\left(\frac{m-1}{2}-1\right)\left(k_z-k_z^s\right)d} \\ \cdots \\ e^{-j\left(\frac{m-1}{2}\right)\left(k_z-k_z^s\right)d} \end{pmatrix} \tag{8.23}$$

where $k_z^s=-\frac{2\pi}{\lambda}\cos(\theta_s)$, which lead to the following beam pattern:

$$B(\theta)=\frac{1}{m}\frac{\sin\left(\frac{m\pi}{\lambda}(\cos(\theta)-\cos(\theta_s))d\right)}{\sin\left(\frac{\pi}{\lambda}(\cos(\theta)-\cos(\theta_s))d\right)} \tag{8.24}$$

The beam pattern is one of the most important function that characterizes the array response. In fig. 8.4 an example of beam-pattern is reported.

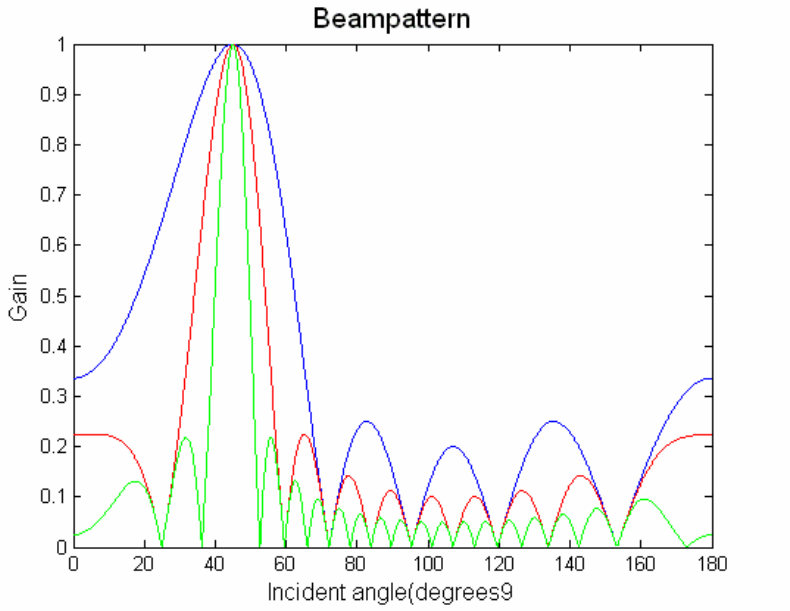

Figure 8.4

Beam-pattern for an ULA with inter sensor space of 0.5m for an incident wave of wavelength 1m as a function of sensors number 5(blue), 10(red) and 20(green). In this example the steering angle is 45 degrees. The gain is $|B(\theta)|$.

As is possible to see in figure 8.4 the waves with incident angle "near" the steering angle are left unchanged by the beam-forming while all the others are reduced in amplitude. A formal definition of angle "near" the steering angle is the null to null beam width (BW_{NN}): the range between the first beam-pattern nulls around the steering angle. The null occurs when the numerator of $B(\theta)$ is zero and the denominator is non zero so, defining $u = \cos(\theta)$:

$$\sin\left(\frac{\pi m d}{\lambda} u\right) = 0 \tag{8.25}$$

or

$$\frac{\pi m d}{\lambda} u = l\pi \tag{8.26}$$

thus the null occurs when $u = l\lambda/md$ and $u \neq l'\lambda/d$. So the first null occurs at $u = \lambda/md$ ($l = 1$ and $l' = m$) and the BW_{NN} is equal to $2\lambda/md$. The important parameter is the total array length expressed in wavelength of the incident wave.

The inter elements space, or better its length expressed in wavelength of the incident wave, it is of fundamental importance too. As an example in figure 8.5 we report the beam-pattern for the same array reported in figure 8.4 but with the incident wavelength reduced to 0.75m.

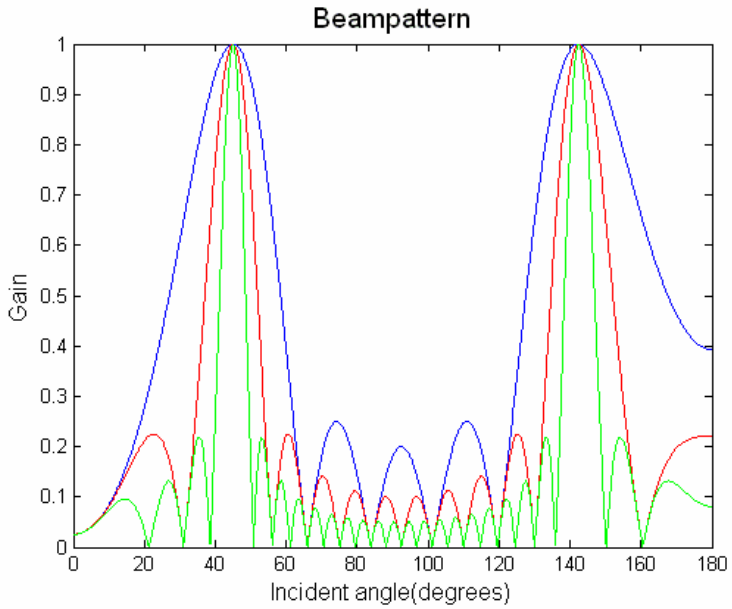

Figure 8.5

Beam-pattern for an ULA with inter sensor space of 0.5m for an incident wave of wavelength 0.5m as a function of sensors number 5(blue), 10(red) and 20(green). In this example the steering angle is 45 degrees. The gain is $|B(\theta)|$.

As it is possible to see in figure 8.5, in this case there are two directions at which the beam-pattern response is unitary; this leads to an ambiguity in resolving the direction of arrival of the incident wave. These grating lobes occur when both the numerator and the denominator of the beam-pattern are equal to 0 so, recalling 8.26 the maximum of the grating lobes occur when:

$$\frac{\pi md}{\lambda}u = l\pi \text{ and } \frac{\pi d}{\lambda}u = l'\pi \qquad (8.27)$$

This happens periodically every

$$u = l\frac{\lambda}{d}. \tag{8.28}$$

If the inter-element spacing $d \geq \lambda$ the grating lobes occur in the visible region $|u| = |\cos(\theta)| \leq 1$. We note that the positions of the grating lobes other than the real one, for a fixed array geometry, are function of the frequency of the incident wave. If we want to steer the array to a desired direction u_s the condition 8.28 becomes (see Eq. 8.24):

$$u = q\frac{\lambda}{d} + u_s \tag{8.29}$$

If the array is required to steer for angles $0 \leq \theta \leq 180$ without ambiguity (only one grating lobe) the inter sensor space must be $d \leq \lambda/2$. The problem of grating lobes is equivalent to that of aliasing in time domain, which occurs when we under sample the time domain waveform.

8.5. Array gain versus noise

One of the most important features of the beam-forming technique, at least in our application, is the array gain in case of white noise. Assuming that the input at each sensor consists of a signal and a noise term uncorrelated among the sensors (spatially white noise), then the signal at each sensor can be written as:

$$x_n(t) = s(t - \tau_n) + n_n(t) \tag{8.30}$$

where $s(t)$ is the plane wave and $n_n(t)$ is the noise term at sensor n. The SNR at each sensor can be written as:

$$SNR_I = \frac{|s(t)|^2}{|n(t)|^2} \tag{8.31}$$

Recalling eq. 8.17, in case of phased array, it is possible to write the array output, due to the signal, as:

$$y(t) = \vec{w}^T \cdot \vec{s}(t) \tag{8.32}$$

the power at of the array output can be written as:

$$E\left(|y_s(t)|^2\right) = E\left(\left|\vec{w}^T \vec{s}(t)\right|^2\right) = E\left(\vec{w}^T \vec{s}(t)\vec{s}^T(t)\vec{w}\right) = \vec{w}^T R \vec{w} \tag{8.33}$$

where the matrix R is defined as $E\left(\vec{s}(t)\vec{s}^T(t)\right)$, using this notation and recalling the definition of the manifold array vector we can write:

$$E\left(|y_s(t)|^2\right) = \vec{w}^T \cdot \vec{v}\left(\vec{k}\right)|s(t)|^2 \, \vec{v}^T\left(\vec{k}\right) \cdot \vec{w} \tag{8.34}$$

the power due to the noise term at the array output is:

$$E\left(|y_n(t)|^2\right) = \vec{w}^T \cdot E\left(\vec{n}(t) \cdot \vec{n}^T(t)\right) \cdot \vec{w} = \vec{w}^T \cdot N \cdot \vec{w} \tag{8.35}$$

The element of the matrix N, since the noise is spatially white, can be written as:

$$N_{i,j} = E\left(\vec{n}_i(t)\vec{n}_j^T(t)\right) = 0 \text{ if } i \neq j \text{ and } |n_i(t)|^2 \text{ if } i = j\,. \tag{8.36}$$

Defining SNR_O as the signal to noise ratio obtained to the output of the array so:

$$SNR_O = \frac{E\left(\left|y_s(t)\right|^2\right)}{E\left(\left|y_n(t)\right|^2\right)}$$

The white noise gain (A_{WNG}) can be written as the ratio between the SNR at the output of the array and the same quantity in the case of single sensor:

$$A_{WNG} = \frac{SNR_O}{SNR_I} = \frac{E\left(\left|y_s(t)\right|^2\right)}{E\left(\left|y_n(t)\right|^2\right)} \frac{\left|n(t)\right|^2}{\left|s(t)\right|^2} \tag{8.37}$$

Substituting eq.8.35 and 8.34 into eq. 8.37 we obtain:

$$A_{WNG} = \frac{\left|\vec{w}^T v\left(\vec{k}\right)\right|^2}{\vec{w}^T \vec{w}} \tag{8.38}$$

In particular we want to evaluate the white noise gain for a specific steering angle; recalling from 8.13a that $\vec{w}^T v\left(\vec{k}\right)$ is the frequency wave-number response and that this quantity is constrained to 1 in the steering direction, we can finally write the white noise gain as:

$$A_{WNG} = \frac{1}{\sum_{n=0}^{m-1} \left|w_n\right|^2} \tag{8.39}$$

Using the Cauchy-Schwartz inequality on the constraint condition $\vec{w}^T v\left(\vec{k}\right) = 1$ we can write:

$$1 = \left(\sum_{n=0}^{m} w_n v_n\left(\vec{k}\right)\right)^2 \le \sum_{n=0}^{m-1} \left|w_n\right|^2 \sum_{n=0}^{m-1} \left|v_n\left(\vec{k}\right)\right|^2 = m \sum_{n=0}^{m-1} \left|w_n\right|^2 \tag{8.40}$$

from eq. It 8.40 follows that $A_{WNG} \le m$.

In the case of uniformly weighted array, $w_n = \frac{1}{m}$ so the white noise gain value is:

$$A_{WNG} = m \tag{8.40a}$$

if we look for the maximum WNG value the uniformly weighted array is the optimum array.

8.6. Simulation results

To evaluate the performances of this technique we perform a simulation of the *OυDE* hydrophone array. Its geometry is reported in table 8.1.

Hydrophone number	Position x(m)	Position y(m)	Position z(m)
1	0	0	0
2	1,047	0	0
3	0,671	0,138	0,949
4	1,391	1,145	0

Table 8.1

The hydrophone positions of the simulated array. The origin of the coordinate system is the hyrophone 1, the x axis is coincident with the direction from hydrophone 1 to hydrophone 2 and the z axis is orthogonal to the plane of hydrophones 1,2,4.

In this simulation we generate one time window of white noise for each hydrophone, the time length is fixed and equal to 5ms. Then we calculate the time delays at which the signal will be measured by the different hydrophones and we add a simulated bipolar neutrino signal on each hydrophone time series. The time delays are calculated assuming the plane wave approximation so:

$$\tau_n = \frac{\vec{a}^T \vec{p}_n}{c} \tag{8.41}$$

where τ_n is the delay at hydrophone n, $\vec{a}$ is the direction of propagation of the incident plane wave, c is the sound speed and $\vec{p}_n$ is the relative position of hydrophone n with respect to the hydrophone 1 (the origin of the reference system). All the delays are referred to the arrival time of the signal on the hydrophone 1 so $\tau_0 = 0$. The matched filter, discussed in chapter 7, is applied to each hydrophone's data flow and the beam-forming is computed using the output of those filters. The steering angle of the array is changed with a step of 1 degree on both θ and φ angles and the maximum of the array response is evaluated as a function of the steering angle. This simulation is repeated for different SNR. Figures 8.6-8.9 show the result of the beam-forming reconstruction algorithm for fixed position of the source, with respect to the array, and for given value of SNR. For each reconstructed position the beam-forming analysis provides an output value. The color scale on the right represents this value after normalization of the maximum to 1.

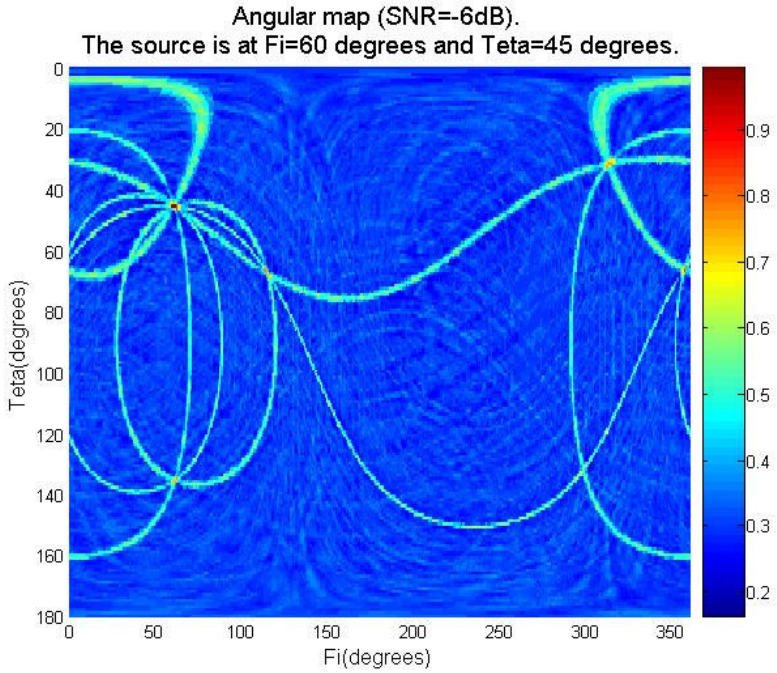

Figure 8.6

The beamforming output for a plane wave incident on the array from Teta=45 degrees and Fi=60 degrees. The SNR is -6dB. The Array output is normalized to its maximum value.

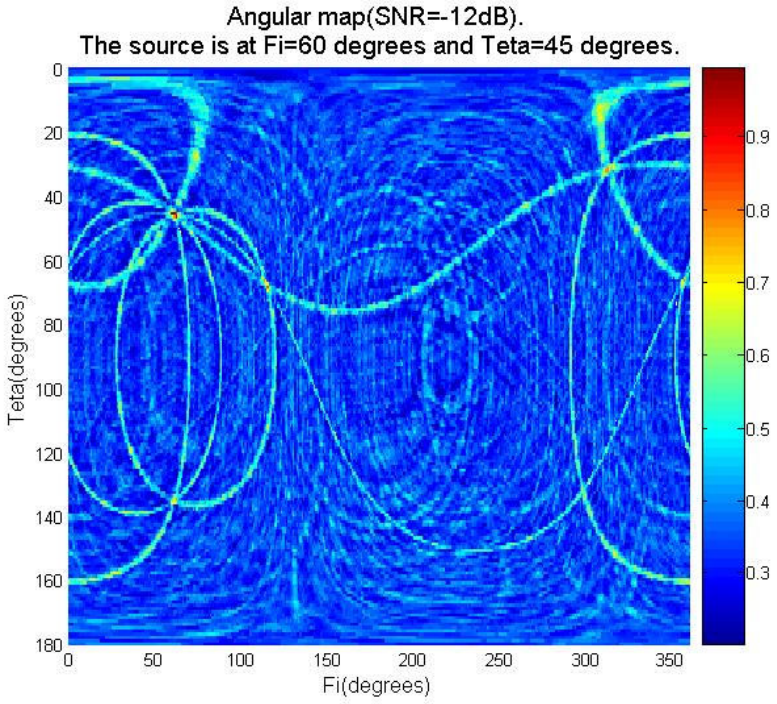

Figure 8.7

The beamforming output for a plane wave incident on the array from Teta=45 degrees and Fi=60 degrees. The SNR is -12dB. The Array output is normalized to its maximum value.

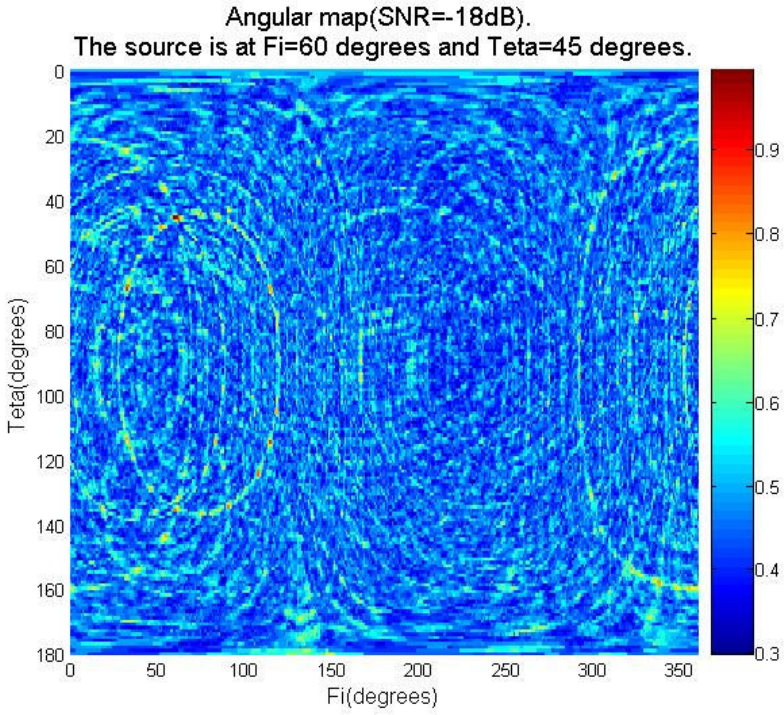

Figure 8.8

The beamforming output for a plane wave incident on the array from Teta=45 degrees and Fi=60 degrees. The SNR is -18dB. The Array output is normalized to its maximum value.

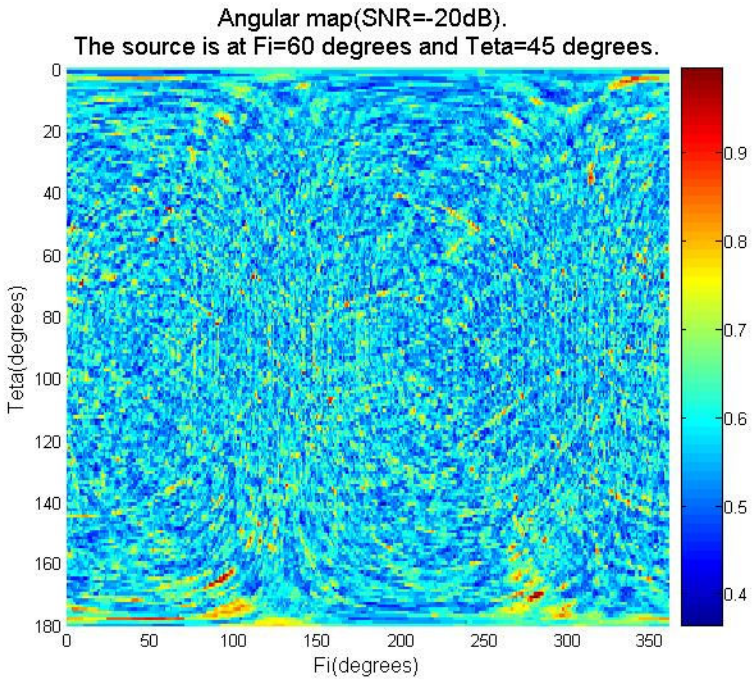

Figure 8.9

The beamforming output for a plane wave incident on the array from Teta=45 degrees and Fi=60 degrees. The SNR is -20dB. The Array output is normalized to its maximum value.

We note that even with a SNR as low as -12dB, at the level of a single sensor, the signal is well discriminated by the background at the output of the array. Let's analyse one of these maps, for example the one reported in fig. 8.6: we note that there is a visible spot in correspondence with the source at $\theta = 45^0$ and $\varphi = 60^0$, moreover there are many regions in which the array output is significantly different from background. The real source, corresponding to the maximum of the array output, is obtained when all the hydrophones are summed coherently and this happen only when the delays are evaluated for the "true" direction of arrival. However there are may other directions for which the delays calculated results in a coherent sum of 2 or more sensors but not all of them. For these aliases the beam-forming algorithm provides an output proportional to the energy reconstructed summing up, with the set of delays need for the selected direction, the signal of each sensors. The maximum value for the reconstructed energy will be obtained when, selecting the proper direction, the delays will allow to sum up with the right phase all the signals. These aliases can be evaluated using the knowledge of the geometry of the array and the direction of arrival of the incident plane wave. The map reported in figure 8.6 is the point spread function of the array: how the array sees a point source coming from a specific direction. Another important aspect that needs to be explained is the fact that we see just one grating lobe, just one real source, even if the inter sensor distance, roughly 1m, allows to reconstruct, without ambiguity, only wavelength bigger than 2m or frequency below 750Hz. As we pointed out in paragraph 8.4 the position of the grating lobes, for a fixed array geometry, are function of the plane wave frequency. This means that plane waves of different frequencies have the grating lobes at different angle as reported, for example, in figure 8.10.

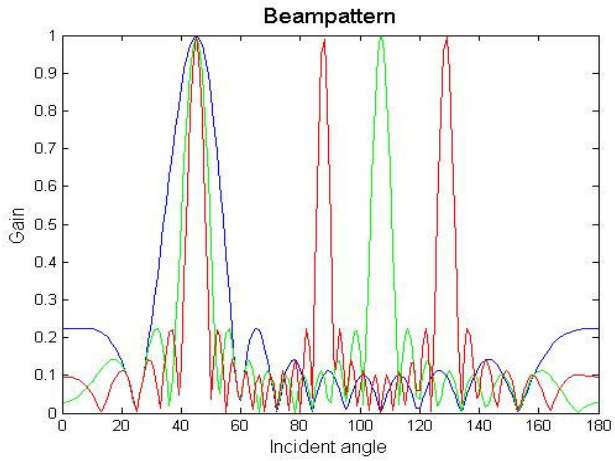

Figure 8.10

Beam-pattern for incident wave of different wavelength: 1m(blu), 2m(green), 3m(red). The simulated array is an ULA with inter sensor space of 0.5m and number of sensors equal to10.

If the frequency spectrum of the incident signal is wide, only the lobe corresponding to the real arrival direction is summed up coherently while a cancellation occurs for the others. In fig. 8.11 the beam-pattern for the matched filter output is reported. This beam-pattern is evaluated in the case of ULA with inter element space of 0.5m using 10 elements. The output of the matched filter is decomposed into frequency components by discrete Fourier transform. The beam-pattern is evaluated for each frequency component and it is weighted by the intensity of the spectral component. All the beam-patterns are summed to retain the beam-pattern of the signal. In radar systems the use of wide band signals is often referred as wide-band beam-forming. The beam-forming is very expensive in terms of computational power.

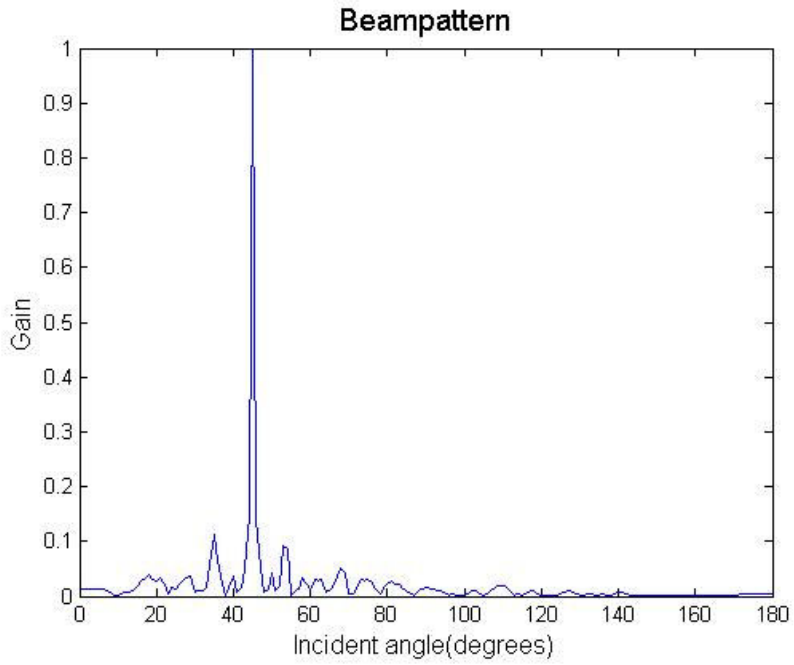

Figure 8.11

The beam-pattern of an ULA of 10 elements spaced of 0.5 for a wideband signal as the matched filter's output.

To build the array output, for each sample, a number of addiction equal to the number of hydrophones minus one are required. This means that in our example (200ksps on 4 hydrophones) we needs a computational power of 600kFLOPS for each set of delays; during the generation of the map reported in figure 8.6 we have used 64.8k sets of delays. The total computational power needed to perform the proposed algorithm on an array of 4 hydrophones is 38.9GFLOPS.

9. Detector simulations

In order to evaluate the possibility to detect acoustic signals from neutrino interactions and to verify the capability of the reconstruction and selection algorithms described in the previous chapters, in distinguishing the signal from background, we describe the simulation of a structure that can be used as a basic block for a full detector of neutrino induced acoustic signal in water. We also describe the performances of the NEMO phase 2 tower, as acoustic neutrino detector.

9.1. Detector geometry

We simulated two different geometries: the NEMO phase 2 tower and a string like detector. The NEMO tower is composed of 16 floors vertically spaced by 40m. Each floor consists of a mechanical horizontal structure, 10m long, with two photomultipliers and one hydrophone at each floor extreme. Adjacent floors are rotated by 90 degrees and the first floor is 150m above the seabed. The total number of hydrophones in the NEMO tower is 34, two for each floor and two at base of the tower. In this simulation we use as active detector, for each floor, only the two hydrophones. The geometry of the hydrophones array, in the case of NEMO phase 2 tower, does not allow to use the beam-forming techniques since the hydrophones are too distant to be considered as a "phased array".

The string like detector, that we have simulated, is composed of 20 phased arrays each made by 4 hydrophones. The arrays are aligned on a vertical line and are spaced by 50m. The first array is placed at 500m above the seabed. The total number of hydrophones, in this geometry, is 80 and the total length of the detector is 1000m. In the following of this chapter we describe the results obtained simulating a detector composed by three of such phased arrays lines arranged on a equilateral triangle with side equal to 500m. These two geometries, in principle, could not be compared since they differ in the number of hydrophones and in the techniques that can be applied to

the data analysis. The NEMO tower in fact is not optimized to be an acoustic detector but since it will be deployed next year and, since it will contain hydrophones, it will offer the possibility to acquire, and analyse, acoustic data. From these data we will gain knowledge to improve the acoustic detection technique and to optimize a possible future detector. The main purpose of the hydrophone system on the NEMO tower is to perform the acoustic positioning of the photomultipliers. In both the simulations the sea depth is assumed to be 3500m.

9.2. Events generation

The first step of the simulation is the event generation. We performed different simulations for different neutrino energies in the range $10^{19} eV$ -$10^{21} eV$. For each energy the neutrino interaction points are generated uniformly over different spherical surfaces, with the constraint of the limited sea depth. Two examples of spherical interaction point distributions are reported in figures 9.1 and 9.2.

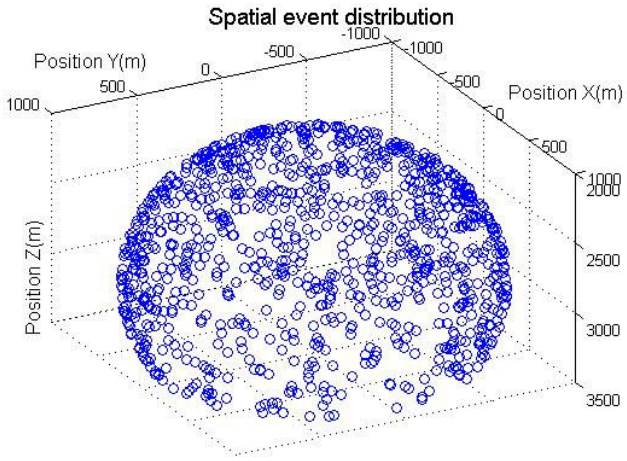

Figure 9.1

Interaction points for a sample of events with neutrino interacting at 1km distance from the center of the detector. Since the seabed is at 3500m no event are generated below this depth.

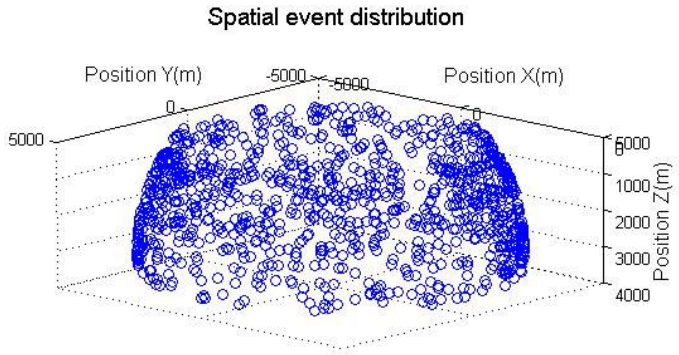

Figure 9.2

Interaction points for a sample of events with neutrino interacting at 5km distance from the center of the detector. Since the seabed is at 3500m no event are generated below this depth and above the surface.

For each interaction point the direction of propagation of the incident neutrino is randomly generated according to the angular distribution discussed in paragraph 3.3. The θ (zenith angle) and φ (azimuth angle) distributions of incident neutrinos are reported in fig. 9.3 and 9.4.

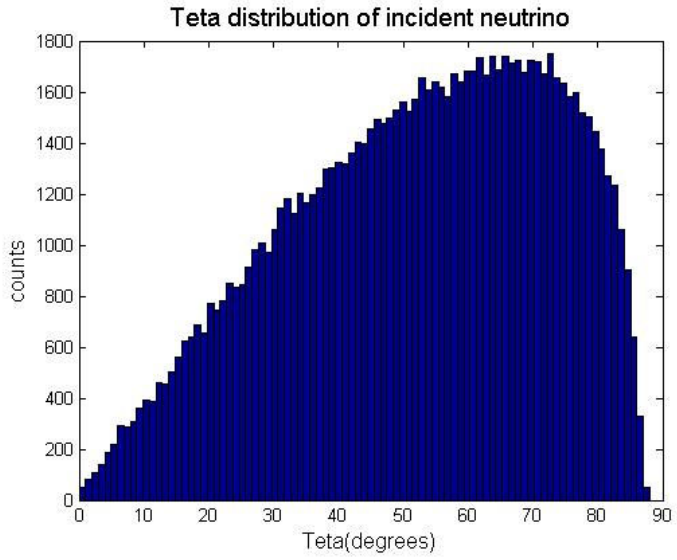

Figure 9.3

The θ distribution of the interacting neutrinos. The figure reports the distribution in the case of sea-depth ~ 3500m and neutrino energy equal to $10^{21} eV$.

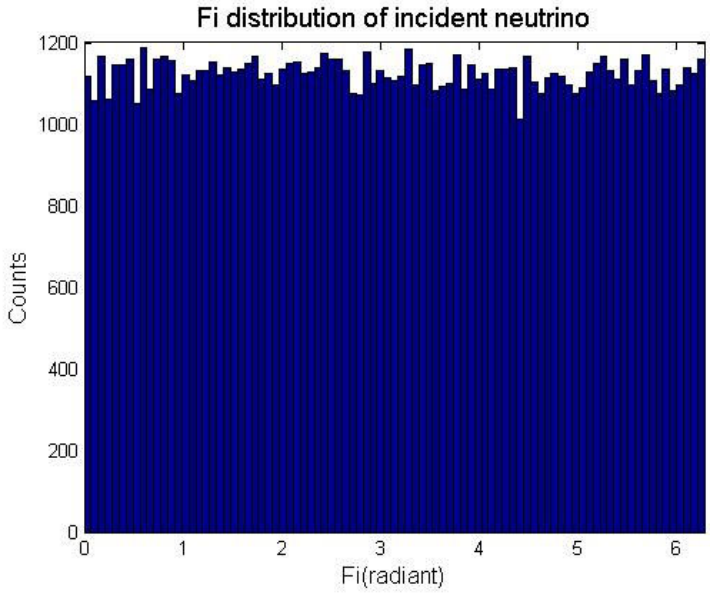

Figure 9.4

The φ distribution of incident neutrinos. Since the neutrino flux is assumed isotropic the distribution is flat.

We simulated the events on 20 spherical shells logarithmically spaced from 316m to 31.6km; the same number of events (10^4) is simulated in each spherical shell so the total number of simulated interactions, for each neutrino energy, is $2 \cdot 10^5$.

9.3. Signal propagation

From each interaction point we propagated the acoustic signal to the detector. This is done using the procedure described in paragraph 4.4. For each simulated acoustic event the knowledge of the starting point (interaction point) and of each sensor position allows to calculate the emission angle at the interaction point and the direction of arrival on the sensor. Moreover the analytical propagation algorithm allows to evaluate the complete ray path so, for instance, the total trajectory length and the maximum depth reached. For each neutrino interaction the emission angle is evaluated and used to calculate the amplitude and the shape of the signal registered by each hydrophone, according to the signal parametrization discussed in chapter 3. Moreover the total path

length from the interaction point to the sensor is evaluated and used to modify the signal amplitude taking into account both the frequency attenuation and the geometrical attenuation discussed in chapter 5. During the propagation the simulation code checks if the sonic ray trajectory hits the surface or the seabed; in these cases the signal is assumed to be undetectable. In fact, even if the propagation code would be able to evaluate the sonic ray trajectory, in case of reflection on the sea surface as on the seabed, it would not calculate any alteration of the signal's frequency spectrum. Taking into account the reflection would imply to know also the roughness of the seabed surface, this is beyond the goal of our present work.

9.4. Signal detection

In this simulation the signal detection has been simplified to be evaluated quickly. The noise level is assumed to be constant during the simulation and to have a root mean square equal to 20mPa. We recall from chapter 5 that this noise level is as the one measured by $O\upsilon DE$ over six month at a depth of 2000m; it is reasonable that the noise level, at lower depth, will be less that the one we now have assumed. The detection probability, knowing the signal amplitude and the noise level, has been parametrized in different ways for the two detectors. In the case of the NEMO tower, since the beam-forming can't be used, the detection probability is assumed to be the one discussed in chapter 7, deriving from the usage of the matched filter on a single hydrophone. We recall from chapter 7 that in this case the signal can be discriminated by the background if the SNR is bigger than -6dB. The neutrino event is assumed to be detected if it is measured by at least 4 sensors over the whole detector.

In case of the string geometry the simulation code propagates the signal up to the phased array; since in this case it is possible to apply both the matched filter and the beam-forming techniques, as discussed in chapter 8, the signal can be measured if the SNR is bigger that -12dB. In this case the neutrino interaction in assumed detected if the acoustic neutrino pulse is measured by at least 2 phased arrays. The mean number of phased arrays that, after the matched filter and beam-forming technique analysis contribute to measure the neutrino induced acoustic bipolar pulse, for detected events,

is reported in fig. 9.5 as a function of the neutrino energy and interaction point distance.

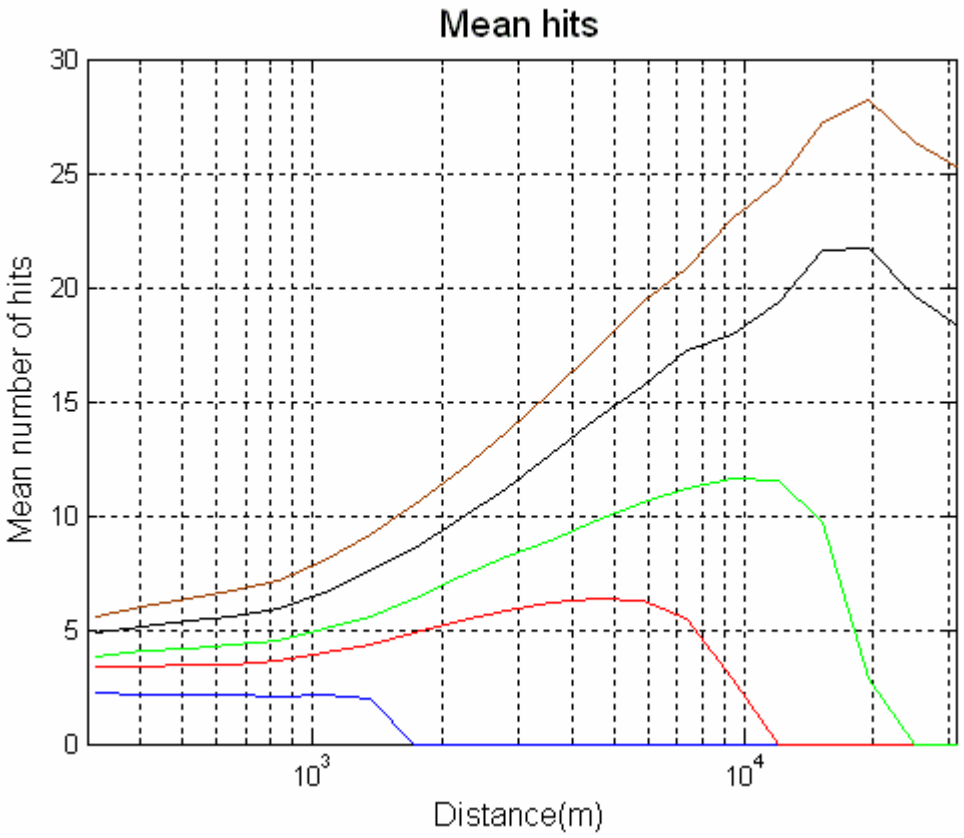

Figure 9.5

Mean number of phased arrays hit after the matched filter and beam-forming analysis. The number of surviving hits is given as a function of the neutrino interaction distance from the detector and of its energy. The figure shows the results for five different neutrino energies: 10^{19}eV (blue line), 10^{20}eV (red line), $2*10^{20}$eV (green line) $5*10^{20}$eV (black line) and 10^{21}eV (brown line).

The number of phased arrays able to discriminate the neutrino signal from the background, increases as a function of the distance, in particular as the neutrino energy increases, for geometrical reason. In fact the collimated sonic pancake, resulting from a neutrino interaction in water, has a bigger geometrical intersection with the detector if the cascade is distance from it. The sharp cut off, evident in the case of 10^{20}eV, is due to the decrease of the signal amplitude with the distance.

9.5. Reconstruction

In chapter 7 we described how to select, for each hydrophone, acoustic signals due to neutrino interaction, from background using the matched filter technique. In chapter 8 we described how to use the information registered by a group of hydrophones, a phased array, to reconstruct the arrival direction of the acoustic signal. Here we want to discuss how, using this information of at least two phased arrays, we can evaluate the reconstruction capability of the simulated detector. The incident angle of the acoustic bipolar pulse on a real phased array can be evaluated with the technique described in chapter 8; in order to simulate an high number of phased arrays a parametrization is needed. In this simulation the reconstructed incident angle of the acoustic bipolar pulse on the phased array is parameterized by a gaussian distribution centred on the nominal value with a σ equal to 5 degrees. Knowing the incident angle on at least two phased arrays, that have discriminated the signal from the background, the sonic rays can be traced back using the propagation technique described in chapter 4. The interaction point is then evaluated as the minimum of the distance between the sonic rays as a function of time. The difference between the reconstructed neutrino interaction point and the true one is reported in fig 9.6, in this simulation the neutrino energy is 10^{20}eV and the interaction point is 1.1km away from the detector.

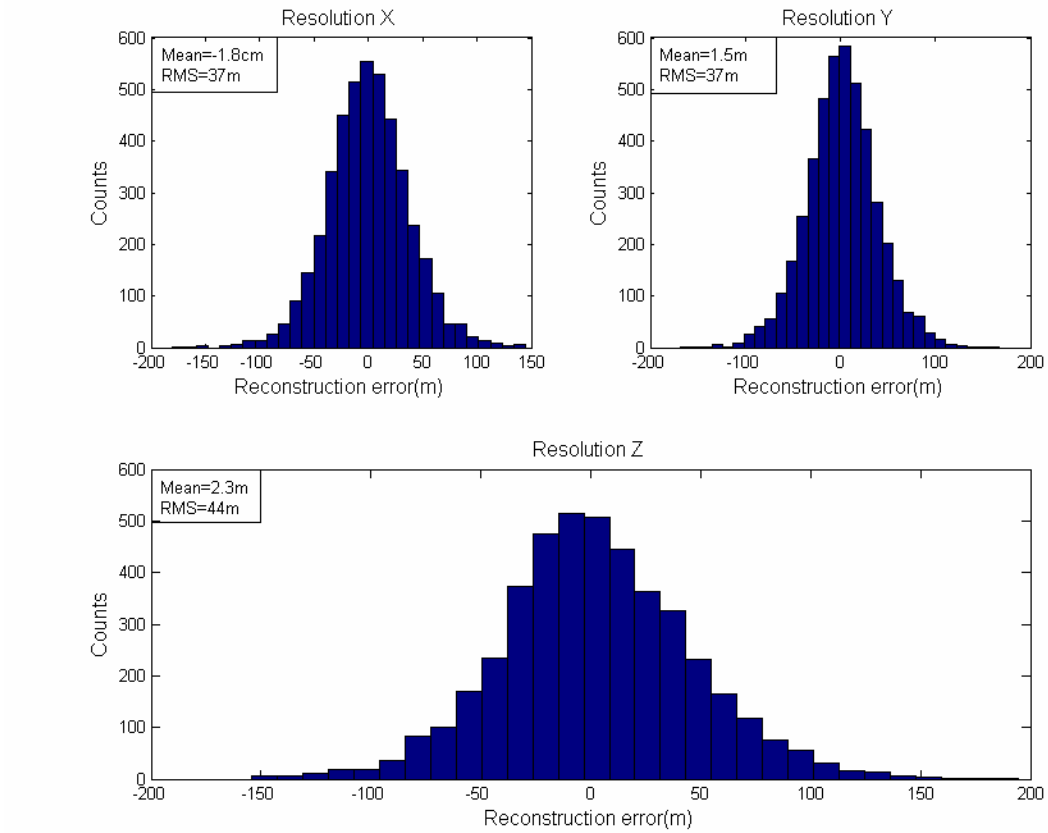

Figure 9.6

The x,y,z (top left, top right and bottom respectively) resolution on the neutrino interaction point reconstruction for a neutrino of 10^{20}eV interacting 1.1km away from the apparatus.

The reconstruction error is a function of many factors. The most important is the capability of each phased array to measure the incident direction of neutrino induced pressure wave; in fact this error can be considered as a systematic error in the reconstruction algorithm and its influence is a increasing function of the distance as reported in fig 9.7.

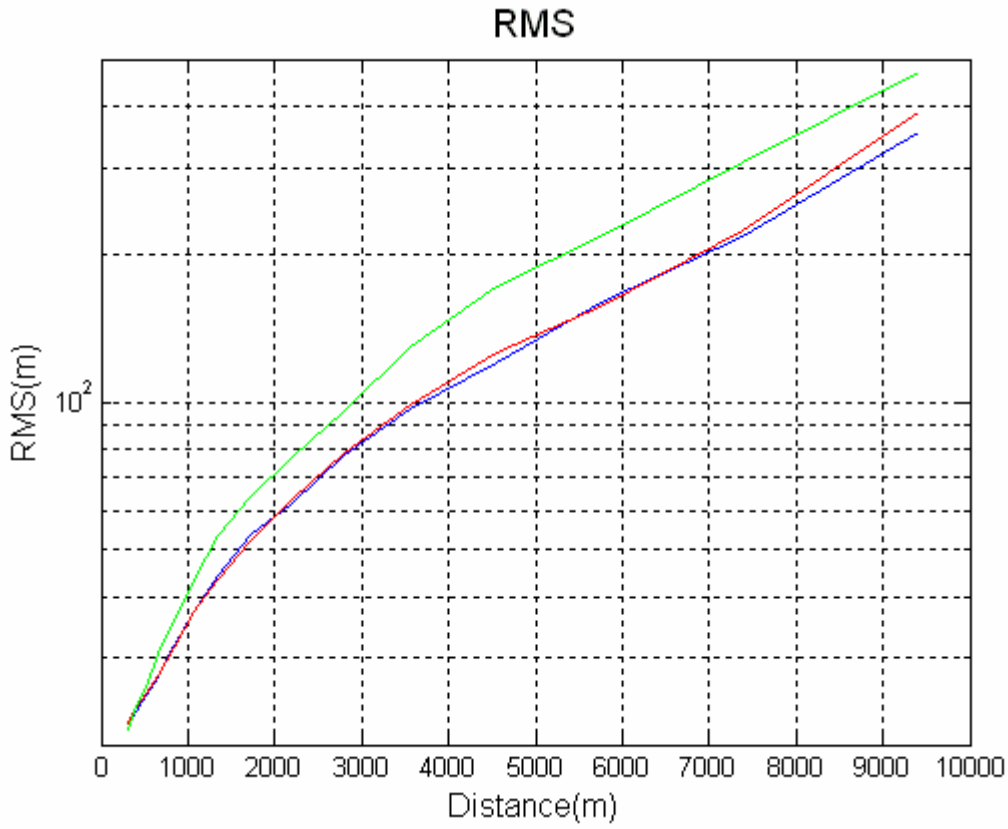

Figure 9.7

The RMS for the x,y,z (blue,red and green lines respectively) resolution on the neutrino interaction point reconstruction for a neutrino energy of 10^{20}eV.

The knowledge of the environmental parameters, in particular the sound speed and its gradient, has a relevant impact on the resolution. To evaluate the influence of those parameters on the resolution, we performed a simulation in which the environmental parameters, used in the reconstruction technique, are different from the one used during the propagation of the acoustic pulse from the cascade to the detector. In particular we parametrized the sound speed and its gradient, used in the reconstruction phase, with a gaussian distribution centred on the nominal value with a σ equal to 5% or 10% of the nominal value. The results of this simulations are reported in fig. 9.8-9.10.

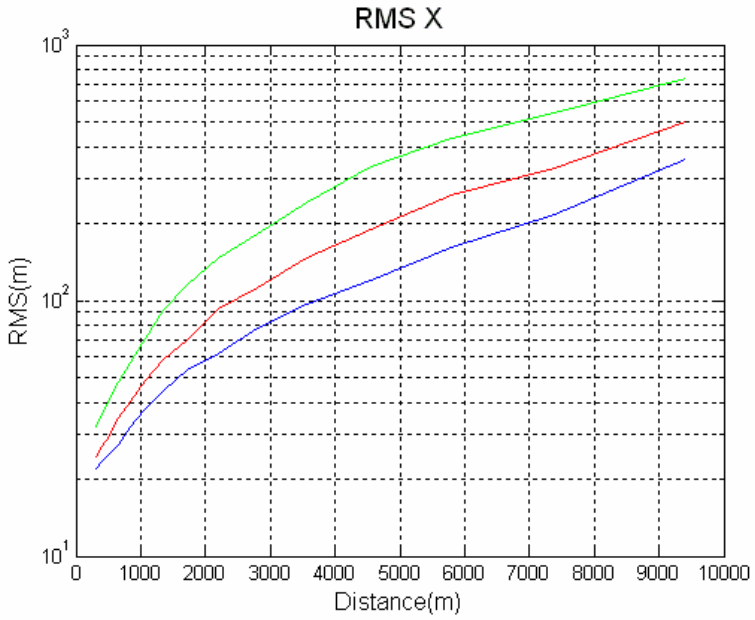

Figure 9.8

The RMS for the x coordinate as a function of the distance of the interaction point and of the kowledge of the environmental parameters. The figure compare the resolution for three different errors of the environmental parameters: perfect knowledge (blue line), a relative error of 5% (red line) and a relative error of 10% (green line).

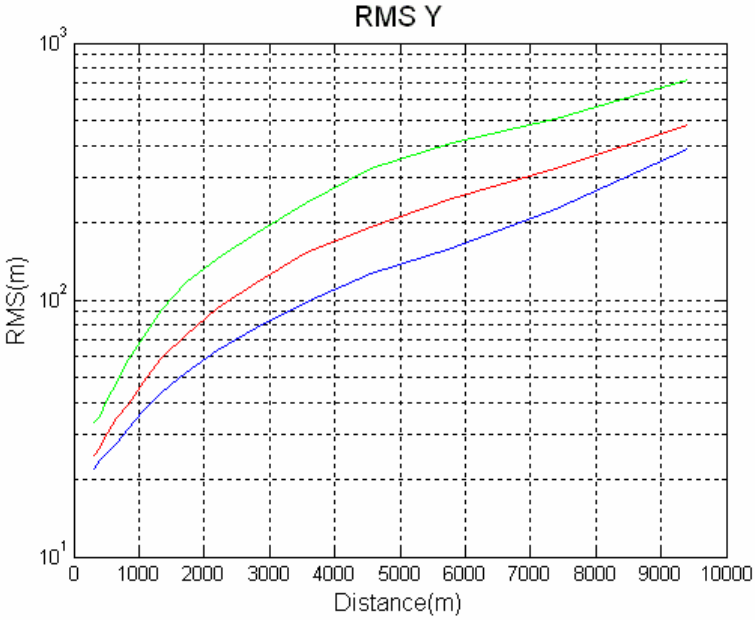

Figure 9.9

The RMS for the y coordinate as a function of the distance of the interaction point and of the kowledge of the environmental parameters. The figure compare the resolution for three different errors of the environmental parameters: perfect knowledge (blue line), a relative error of 5% (red line) and a relative error of 10% (green line).

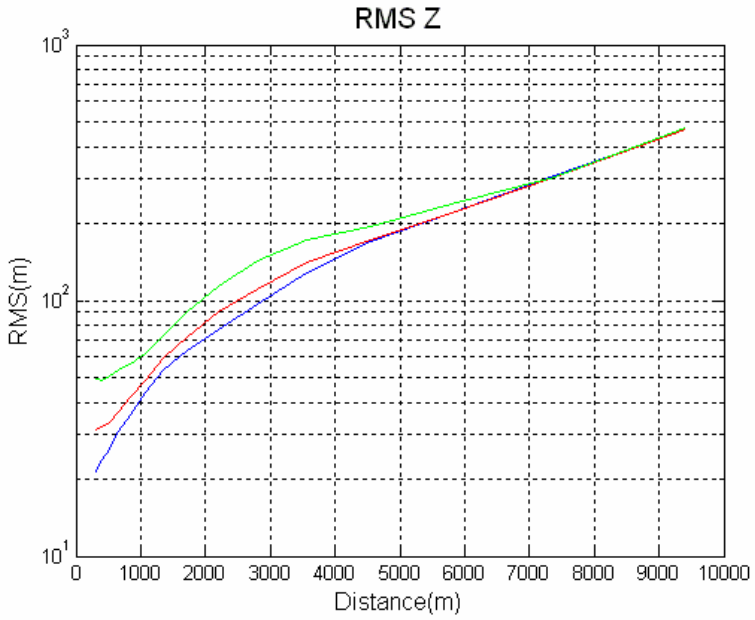

Figure 9.10

The RMS for the z coordinate as a function of the distance of the interaction point and of the kowledge of the environmental parameters. The figure compare the resolution for three different errors of the environmental parameters: perfect knowledge (blue line), a relative error of 5% (red line) and a relative error of 10% (green line).

We note that the resolution error, in particular for the z coordinate, at high distances approaches the one obtained with a perfect knowledge of the environmental parameters. This result is due to the combination of two effects. The incident direction of the acoustic pressure waves on the phased arrays tends to be the same as the distance of the neutrino interaction point increases. This results in an error that is almost constant at large distances. In contrast the resolution error, due to the non perfect reconstruction of the incident angle of the pressure wave on the phased arrays, increases with the distance. As result at large distances from the detector the resolution error due to the knowledge of the environmental parameters becomes negligible with respect to the one due to the reconstruction error of the incident direction of the pressure waves on the phased arrays.

9.6. Simulation results

A number of 10^4 events have been generated over a spherical surface, as explained in paragraph 8.2, then propagated to the detector and measured. For each sphere radius the detection efficiency has been calculated as the number of detected events over the total number of generated interaction. This efficiency contains both geometrical effects and the sensor (tower detector), or phased array (line detector), detection efficiencies. The results for the NEMO tower reported in fig. 9.11 while the results for the string geometry are shown in fig. 9.12. We note that the efficiency as a function of the distance shows a maximum, at low distances, that is function of the neutrino energy. We recall, from chapter 3, that the acoustic energy is very collimated in the plane perpendicular to the neutrino induced cascade axis. The amplitude of the acoustic signal will decrease of one order of magnitude in few degrees; at short distance the geometrical intersection between the sonic pancake and the detector plays a key role. As the distance of the interaction point increases the signal attenuation will decrease the probability of detection. The combination of these two effects will results in a maximum at some distance that depends on the signal amplitude and so on its energy.

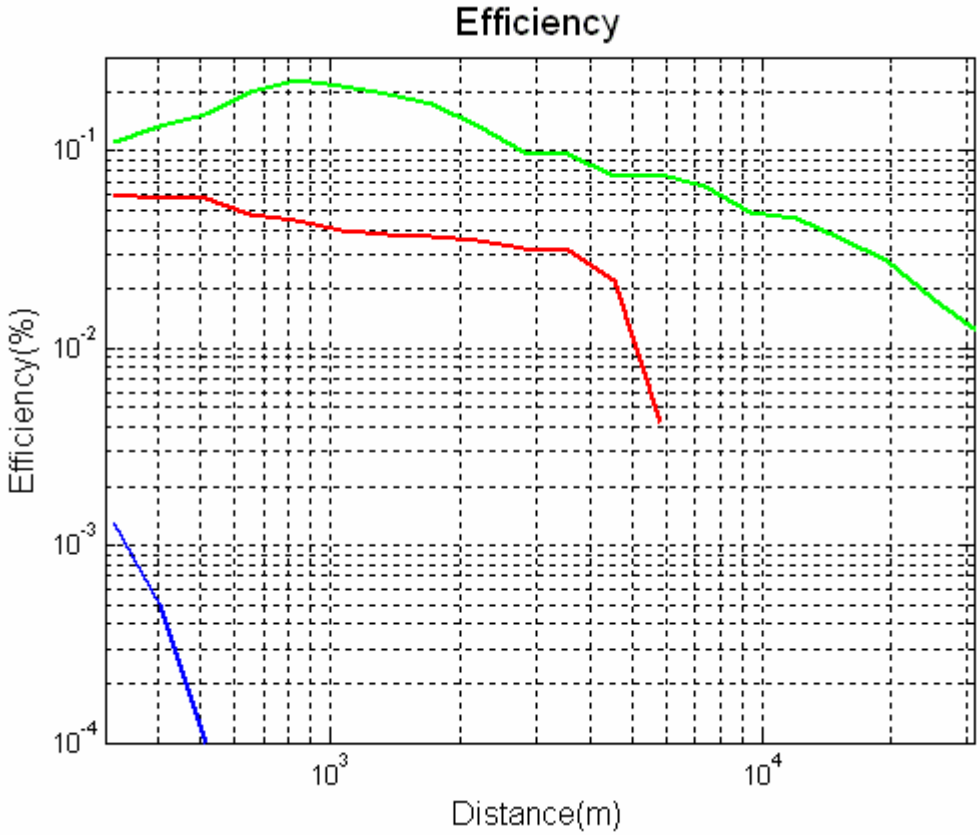

Figure 9.11

The efficiency plot of the NEMO tower calculated for a neutrino energy of 10^{19} eV (blue line), 10^{20} eV (red line) and 10^{21} eV (green line).

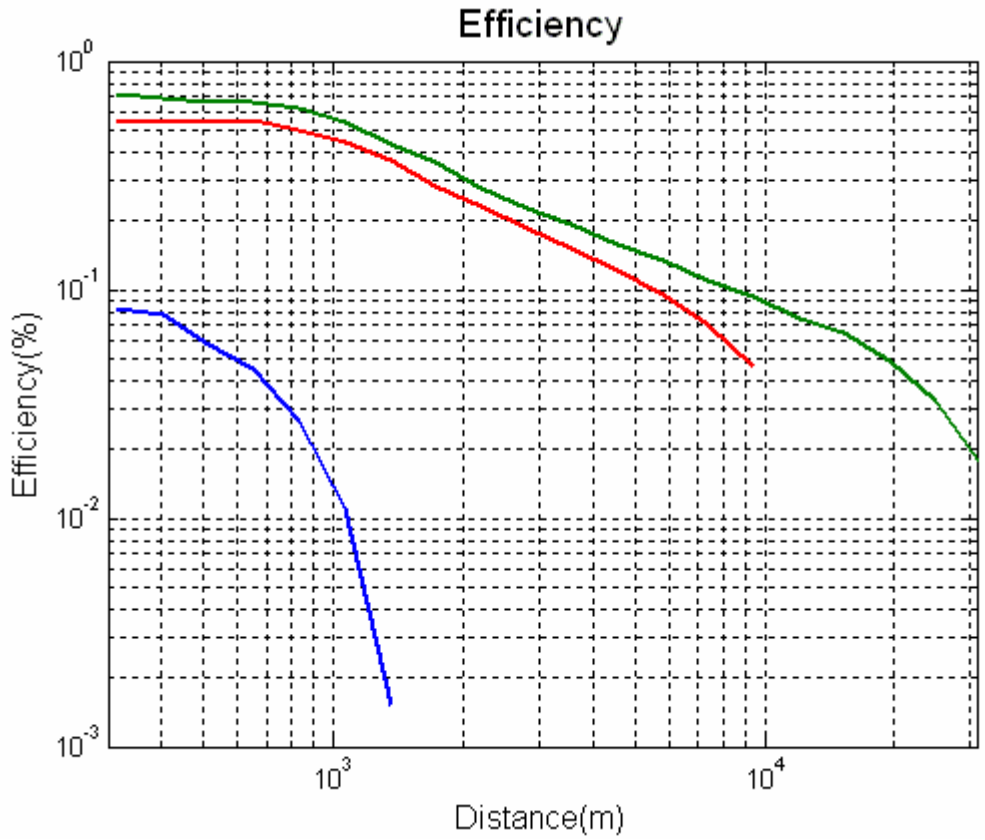

Figure 9.12

The efficiency plot of the string detector calculated for a neutrino energy of 10^{19} eV (blue line), 10^{20} eV (red line) and 10^{21} eV (green line).

In case of neutrino energy of $10^{19} eV$ the amplitude of the acoustic signal is at the limit of the detection capability and so the detector is sensible only to a very small part of the sonic pancake and only if the interaction point is near to the detector. This explain why the efficiency is so small and do not show a maximum.

The efficiency plots have been used to calculate the effective volume of detection as a function of the simulated neutrino energies. The above procedure calculate the efficiency of detection at a fixed distance from the detector. A spherical shell volume is then evaluated around each simulated spherical surface and the efficiency is assumed to be constant over this volume. A numerical integration is then performed and the effective volume is calculated; the results are reported in table 9.1. The uncertainties reported in the table 9.1 are the statistical error due to the limited number of detected events. Since the effective volume has been calculated as:

$$V = \sum_{n=1}^{N} \varepsilon_n \Delta V_n \tag{9.1}$$

where ε_n is the neutrino detection efficiency over the spherical surface n and ΔV_n is the spherical shell volume around the surface n.

Neutrino energy (eV)	Effective volume (km^3) for the NEMO Tower	Effective volume (km^3) for the string detector
10^{19}	$2.5 \cdot 10^{-4} \pm 1.1 \cdot 10^{-4}$	0.18±0.05
10^{20}	6.1±0.2	44.2±2.7
10^{21}	39.4±2.3	86.8±3.8

Table 9.1
Effective volume as a function of the neutrino energy for the NEMO phase 2 tower and the proposed detector made of one vertical string of phased arrays.

This result shows that even a simply acoustic detector could increase the detection volume of a neutrino telescope by almost two order of magnitude. An acoustic detector as the one described in this work will not be able to make "astronomy" (i.e. it will have a very poor positioning resolution) but it will have a high capability to detect UHE astrophysical neutrinos. In my view the final neutrino telescope should have include a Cherenkov detector integrate with acoustic lines of phased arrays.

9.7. Expected event rate for GZK neutrinos

As a final result we evaluate the expected event rate, from GZK neutrinos, that is possible to measure with the proposed detector geometry and analysis technique. In fig. 9.13 we report the expected neutrino flux due to GZK effect, discussed in chapter 1. The detected event rate can be evaluated by the following integral:

$$Rate = \int_{E_1}^{E_2} dE \int_0^T dt \int_\Omega d\Omega \int_0^\infty r^2 \rho \cdot Na \cdot F(E) \cdot \sigma(E) \cdot \varepsilon(E,r) dr \tag{9.2}$$

where F is the GZK neutrino flux as a function of the neutrino energy, σ is the neutrino cross section, ρ is the medium density, Na is the Avogadro number and ε is the detection efficiency of the detector. Using the efficiency of detection discussed in

the previous paragraph it is possible to evaluate numerically this integral. The result, integrated between 10^{19}eV and 10^{21}eV, for an observation period of one year is $(30{,}5 \pm 1{,}7) \cdot 10^{-2}\, yr^{-1}$. The GZK neutrino flux decreases very quickly for neutrino energies above 10^{20}eV and below 10^{17}eV; since the acoustic detection techniques starts to be effective from energies above 10^{19}eV, only a small part of the GZK neutrinos will be measured. To measure a number of GZK events of the order of $\sim 10^{1}\text{yr}^{-1}$ it is necessary to increase correspondingly the number of strings that compose the detector to increase the effective volume or to develop other techniques that will further increase the background rejection allowing to lower the energy threshold down to 10^{18}eV.

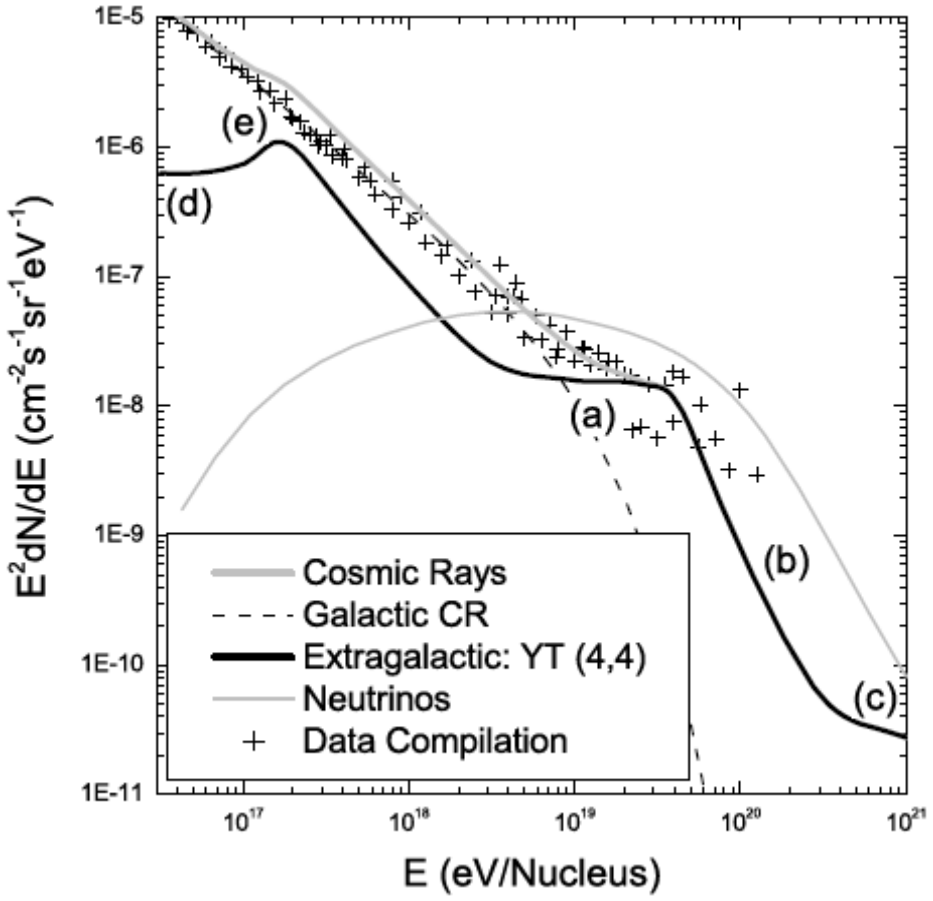

Figure 9.13

Neutrino and cosmic ray fluxes taken from [53], YT is the flux model due to Yoshida and Teshima.

Bibliography

[1] Greisen, Kenneth. Physical Review Letters 16 (17): 748–750

[2] Zatsepin, G. T.; Kuz'min, V. A. Journal of Experimental and Theoretical Physics Letters 4: 78–80

[3] J. Cronin, T. K. Gaisser and S. P. Swordy, Sci, Amer. 276 (1994).

[4] P. Meszaros. Science 291 (2001) 79–84, astro-ph/0102255.

[5] A. Dar, Proceedings of the 11th International Workshop on Neutrino Telescopes, pp. 451–476, 2005, astroph/0601329.

[6] http://www.ifh.de/baikal/baikalhome.html

[7] http://icecube.wisc.edu/

[8] http://antares.in2p3.fr/

[9] http://nemoweb.lns.infn.it/

[10] http://www.nestor.org.gr/

[11] http://www.km3net.org/

[12] Askaryan GA, SOVIET PHYSICS JETP-USSR 14 (2): 441-443 1962.

[13] D.Saltzberg et al. Phys.Rev.Lett.86:2802-2805,2001; P.W.Gorham et al. Phys.Rev.D72:023002,2005; P.W.Gorham et al. Phys.Rev.Lett.99:171101,2007.

[14] N.Lehtinen et al., Phys.Rev.D69:013008,2004.

[15] I.Kravchenko et al., Astropart.Phys.20:195-213,2003.

[16] P.W.Gorham et al., Phys.Rev.Lett.93:041101,2004.

[17] P. Mioˇcinovi´c et al., "Tuning into UHE neutrinos in Antarctica: The ANITA experiment," eConf C041213 (2004) 2516, astro-ph/0503304.

[18] http://www.auger.org/

[19] J. Vandenbroucke, G. Gratta and N. Lehtinen, Astrophys.J. 621, 301 (2005), astro-ph/0406105.

[20] Askaryan, G. A. 1957, Soviet J. At. Energy, 3, 921

[21] Niess, Doctoral thesis, http://marwww.in2p3.fr/~niess/these.pdf

[22] Learned et al., 2002 Astropart. Phys. 17, 279

[23] Vandenbroucke, Gratta, Lehtinen Astrophysical Journal 621:301-312

[24] Perkin, Doctoral thesis, http://arxiv.org/PS_cache/arxiv/pdf/0801/0801.0991v1.pdf

[25] Sulak et al., 1979, Nucl. Instrum. Methods Phys. Res., 161, 203

[26] S. Schwemmer, Diploma thesis, FAU-PI1-DIPL-05-002.

[27] G.DeBonis private communications.

[28] Gandhi et al., 1998, Phys. Rev. D, 58, 093009

[29] Landau and Pomeranchuk, Dok Akad. Mauk. USSR 92(535), 1953

[30] Migdal, Phys. Rev. 103(6), September 1956.

[31] Del Grosso, 1974, Journal of the Acoustical Society of America 56: 1084-1091

[32] F.J. Millero, Xu Li, Journal of the Acoustical Society of America 93: 255-275.

[33] Wilson, Journal of the Acoustical Society of America 32: 1357.

[34] Giorgio Riccobene, private comunications.

[35] Francois and Garrison, Journal of the Acoustical Society of America 72: 896-907

[36] Ainslie and McColm, Journal of the Acoustical Society of America 103:1671-1672

[37] C. A. Boyles, *Acoustic waveguides: applications to oceanic science* (New York: Wiley, 1984).

[38] Mickael B.Porter and Homer P.Bucker, Journal of the Acoustical Society of America 55:63-79

[39] Paul C. Etter, *Underwater Acoustic Modelling*. Elsevier Science Publishing CO.INC. New York. 1991.

[40] http://www.bksv.com/

[41] Wenz, Journal of the Acoustical Society of America 51: 1010-1024.

[42] Giorgio Riccobene, arXiv:0804.2913v1

[43] Brennan, Proc. IRE, vol. 43, 1530.

[44] Helstorm, Proc. IRE vol. 43,1111-1118.

[45] Levin, IRE National Convention Record, pt. 4, 174-181.

[46] Middleton, J. Soc. Indus. Appl. Math., vol. 3, 192-253.

[47] Rochefort, IRE National Convention Record, pt. 4, 30-34.

[48] Barry D. Van Veen, Kevin M. Buckley, IEEE 0740-7467/88/0400-0004

[49] Wang Min, IEEE 0-7803-8882-8/05.

[50] F. Anderson et al., IEE proc. H, Vol 138, Iss 4, 342-346

[51] Carsten Sydow, Journal of the Acoustical Society of America 96: 845-849

[52] David Seckel arXiv:astro-ph/0103300v1

Acknowledgements

This thesis would not have been possible without the support, the encouragement and the remarkable patience of my thesis advisor Prof. Antonio Capone who guided me since the beginning of this work, sharing with me his experience and knowledge.
I cannot thank him enough.

I am deeply in debt to Prof. Maurizio Bonori for his critical review of this work and for many fruitful discussions.

I wish to thank Dr. Giorgio Riccobene for allowing me to use the ONDE data and other materials and for the support he gave me despite the little time he had available.

I'd like to thank Prof. Mauro Morganti for the suggestions, corrections and revisions made to text.

I have also benefited from many discussions with members of the NEMO group of Roma, in particular with Giulia De Bonis, who share with me her results about the neutrino induced acoustic signal.

Lastly, and most importantly, I wish to thank my parents, Maurizio and Laura. They bore me, supported me, and loved me. To them I dedicate this thesis.